



University of HUDDERSFIELD

University of Huddersfield Repository

Shen, Qiang

An In-Situ TEM Study of High Temperature Helium Irradiation of 4H-SiC

Original Citation

Shen, Qiang (2015) An In-Situ TEM Study of High Temperature Helium Irradiation of 4H-SiC. Masters thesis, University of Huddersfield.

This version is available at <http://eprints.hud.ac.uk/id/eprint/25377/>

The University Repository is a digital collection of the research output of the University, available on Open Access. Copyright and Moral Rights for the items on this site are retained by the individual author and/or other copyright owners. Users may access full items free of charge; copies of full text items generally can be reproduced, displayed or performed and given to third parties in any format or medium for personal research or study, educational or not-for-profit purposes without prior permission or charge, provided:

- The authors, title and full bibliographic details is credited in any copy;
- A hyperlink and/or URL is included for the original metadata page; and
- The content is not changed in any way.

For more information, including our policy and submission procedure, please contact the Repository Team at: E.mailbox@hud.ac.uk.

<http://eprints.hud.ac.uk/>

**An In-Situ TEM Study of High Temperature
Helium Irradiation of 4H-SiC**

Qiang Shen

Electron Microscopy and Materials Analysis Research Group
School of Computing and Engineering
University of Huddersfield, Huddersfield, UK

January 2015

Contents

List of Figures	v
List of Tables	vii
List of Important Equations	viii
List of Abbreviations and Acronyms	ix
List of Nomenclature	xi
Acknowledgements	xii
Abstract	xiii
1. Introduction	1
1.1 History	1
1.2 Application.....	2
1.2.1 Electronic devices	2
1.2.2 Non-nuclear structural materials	3
1.2.3 Astronomy.....	3
1.2.4 Abrasives and cutting	3
1.2.5 Nuclear materials	3
1.2.5.1 Nuclear fuel cladding and coatings	4
1.2.5.2 Structure support in nuclear reactors	4
1.2.5.3 Immobilization of nuclear waste	5
1.2.5.4 The first wall candidate for fission reactor	5
1.3 Motivation.....	6
1.4 Work undertaken.....	7
2. Literature Review	8
2.1 Silicon carbide	8
2.1.1 Structure and valence bond	8
2.1.2 Properties of SiC	9
2.2 Ion-solid interactions	9
2.2.1 Energy loss mechanism.....	10
2.2.1.1 Binary collision approximation	10
2.2.1.2 Nuclear stopping.....	10

2.2.1.3 Electronic stopping	10
2.2.2 Ion range and distribution	12
2.2.3 Channelling	12
2.2.3.1 General	12
2.2.3.2 Channelling in SiC materials	13
2.2.4 Radiation damage	13
2.2.5 Collision cascades	14
2.2.6 Spike.....	14
2.2.6.1 Displacement spikes	14
2.2.6.2 Thermal spikes.....	15
2.3.7 Phase stability and transformation	15
2.3.8 Sputtering	15
2.3.8.1 Sputtering of SiC	16
2.3.9 Computer simulation.....	17
2.3 Transmission Electron Microscope	18
2.3.1 TEM sample preparation.....	18
2.3.2 TEM for irradiation damage investigation.....	19
2.3.3 Electron irradiation in the TEM	19
2.3.4 TEM with in-situ ion irradiation	19
2.3.5 TEM for SiC.....	20
2.4 Irradiation effects on SiC	21
2.4.1 Electron irradiation.....	21
2.4.1.1 100–160 keV	21
2.4.1.2 200-400 keV	22
2.4.1.3 >400 keV	22
2.4.2 He ion irradiation	23
2.4.2.1 1-10 keV	23
2.4.2.2 10-160 keV	23
2.4.2.3 >1 MeV.....	24
2.5 Diffusion in SiC	24
2.5.1 Self diffusion.....	24
2.5.2 He diffusion.....	25
3. Experimental Methods	26

3.1 Bulk materials	26
3.2 TEM specimen preparation.....	26
3.2.1 Cutting of bulk material	26
3.2.2 Mechanical polishing	26
3.2.3 Ion beam milling	28
3.3 Transmission electron microscope.....	29
3.3.1 Electron scattering.....	29
3.3.1.1 Elastic scattering.....	30
3.3.1.2 Inelastic scattering	32
3.3.2 Components and structure.....	32
3.3.2.1 Electron source	32
3.3.2.2 Lenses	33
3.3.2.3 Apertures	34
3.3.2.4 Image capture	34
3.3.3 Main operating modes and techniques	35
3.3.3.1 Diffraction	36
3.3.3.2 Imaging.....	36
3.3.3.3 Down-zone imaging	36
3.3.3.4 Contrast mechanisms.....	37
3.4 MIAMI.....	38
3.4.1 Ion source	39
3.4.2 Beam profile monitors.....	40
3.4.3 Beam focus and deflection	40
3.4.3.1 Einzel lens	40
3.4.3.2 Bending magnet.....	40
3.4.3.3 Double deflection	41
3.4.4 Current metering system	42
3.4.4.1 Skimmer	42
3.4.4.2 Current metering rod	43
3.4.5 Final deflection.....	43
3.4.6 Transmission electron microscope.....	44
4. In-situ Analysis of Helium Irradiation Effect on SiC at High Temperatures	45

4.1 Introduction.....	45
4.2 Irradiation conditions	46
4.2.1 Computer calculation with SRIM	46
4.3 Experimental results	47
4.3.1 Helium bubbles	47
4.3.2 Bubble discs	48
4.3.2.1 Plan-view and edge-on bubble discs	49
4.3.2.2 Effects of temperature on bubble disc formation	51
4.3.2.3 The growth of bubble discs with increasing He fluence	53
4.3.2.4 The growth of bubble discs whilst held at 800 °C.....	56
4.3.2.5 Final size distribution of bubble discs	58
4.3.2.6 The crystallographic orientation of the edge-on bubble discs.....	60
4.4 Summary	68
5. Discussion	69
5.1 The growth mechanism of the bubble discs.....	69
5.2 The motion of helium atoms and helium bubbles.....	72
5.2.1 Motion of helium atoms	72
5.2.2 Motion of helium bubbles	72
5.3 The growth and growth rate of bubble discs.....	73
5.4 Analysis of bubble growth during temperature holding period.....	73
5.5 The final size distribution of bubble discs	73
5.6 Preferential habit planes of the bubble discs	75
5.6.1 The bubble discs viewed in [001] direction	75
5.6.2 The edge-on bubble discs viewed in other down-zone directions	77
6. Conclusions and Further Work.....	79
6.1 Conclusion	79
6.2 Further work	80
References	81

List of Figures

1.1	Structure of the TRISO fuel particles and irradiation induced crack	4
1.2	Prototype SiC/SiC control rods with articulating joints	5
1.3	Operating temperature and displacement fluence for different reactor systems	6
2.1	Position and projection of silicon and carbon atoms in SiC	8
2.2	The reduced nuclear and electronic stopping cross sections as a function of $\epsilon^{1/2}$	11
2.3	The initial ion range and the projected range of the incident ion	12
2.4	The schimatic of channelling	12
2.5	Schematic of a collision cascade	14
2.6	Schematic of a displacement spik	15
2.7	Schematic of sputtering	16
2.8	The energy range for C and Si displacements	21
3.1	Tripod polishing jig and stub	27
3.2	A round Molybdenum grid with a SiC sample and glued areas	28
3.3	Geometry in Gatan PIPS	29
3.4	Different kinds of electron scattering from a thin specimen	29
3.5	One-dimensional schematic of von Laue approach	31
3.6	Schematic of the Bragg diffraction	31
3.7	Schematic of the thermionic electron source	32
3.8	Schematic of a magnetic lens	33
3.9	The two basic modes of TEM operation	35
3.10	The mechanism of mass-thickness contrast	37
3.11	Schematic of the ion beamline from the ion source to the final deflection	39
3.12	An exploded view of exploded view of Model 101-Q ion source ion source	39
3.13	Schematic of double deflection	41
3.14	Sample position geometry in the MIAMI facility	42
4.1	Graphs output from SRIM	46
4.2	TEM images of bubbles at fluence of 6.1×10^{16} ions.cm ⁻² at 700 °C	47
4.3	TEM images of bubbles and edge-on bubble discs at 6.1×10^{16} ions.cm ⁻² at 800 °C	48
4.4	Plan-view and edge-on bubble discs at a fluence of 6.1×10^{16} ions.cm ⁻² at 900 °C observed close to [001] zone-axis	50
4.5	The sizes of the edge-on bubble discs at different temperatures at the same fluence	

of $\sim 6.1 \times 10^{16}$ ions.cm ⁻² viewed close to [001] direction	52
4.6 The growth curve of edge-on bubble discs at 800 °C with different fluences.....	54
4.7 The length (a) and the width (b) increase of bubble discs at 800 °C with increasing He fluence	55
4.8 The growth of bubble discs whilst held at 800 °C at 3.8×10^{16} ions.cm ⁻²	56
4.9 The growth curve of bubble discs whilst held at 800 °C	57
4.10 Final size distribution of bubble discs at 900 °C at a fluence of 6.1×10^{16} ions.cm ⁻²	58
4.11 The diffraction pattern of (001) plane (a); image of edge-on bubble discs lying on (001) plane (b); the (001) zone indexing generated by JEMs (c)	61
4.12 Distribution of the angles of the edge-on bubble discs and fitting curve	62
4.13 Schematic of [001]-centred zone-map showing low-order zones selected Kikuchi lines derived from JEMs	64
4.14 Schematic of [001]-centred zone-map with diffraction patterns	65
4.15 Edge-on bubble discs observed in different done-zone directions	66
4.16 Angle distributions of edge-on bubble discs observed in different done-zone conditions	66
5.1 Schematic of the helium filled platelet, constrained by two dislocation dipoles on both sides	70
5.2 The TEM image of on-edge bubble discs viewed on [001] zone-axis and the structure of (001) plane viewed on [001] zone-axis derived from software Crystalmaker	75
5.3 The layer structure observed in [100] direction	75
5.4 The geometrical view of bubble discs lying on (100) planes when observed at different zones	77

List of Tables

2.1	Fundamental properties of common silicon carbide polytypes	9
3.1	The sizes of diamonds on polishing disc for various sample thicknesses	27
4.1	The most common transmutation reactions in SiC	45
4.2	The parameters of gauss fitting of the final size distribution	59
4.3	Result of the multi-peak fitting	62
4.4	Calculated angles from the [001]-zone to various zones in its surrounding ZAPMap	63

List of Important Equations

2.1	Equation of sputtering	16
2.2	Equation of helium diffusion coefficient from Jung's paper	25
2.3	Equation of helium diffusion coefficient from Pramono's paper	25
3.1	The differential scattering cross section for a single isolate atom	30
3.2	Scattering cross section for scattering into all angles greater than θ	30
3.3	Square of the absolute value of amplitude of an electron wave scattered from an isolated atom	30
3.4	Structure factor	30
3.5	Von Laue's diffraction equations (a)	30
3.6	Von Laue's diffraction equations (b)	31
3.7	Von Laue's diffraction equations (c)	31
3.8	Bragg's law	31
3.9	Equation of Lorentz force	40
3.10	The voltage applied in the Colutron G-2	40
3.11	The velocity of ions entering into the magnet bending	41
3.12	The electrical force between the two plates of the double deflection	41
3.13	The electric field between the plates of the double deflection	41
3.14	The electric field between the plates of the final deflection	41
3.15	The electrical force between the two vertical plates of the final deflection	41
3.16	The voltage applied between two vertical plates of the final deflection	41
5.1	The dissociative/interstitial mechanism of helium diffusion	71

List of Abbreviations and Acronyms

BCA	Binary Collision Approximation
CCD	Charge-Coupled Device
CMR	Current Metering Rod
EDX	Energy Dispersion X-ray spectrometry
EELS	Electron Energy Loss Spectrometry
FHRs	Fluoride-cooled High Temperature Reactors
FIB	Focused Ion Beam
GFRs	Gas-cooled Fast Reactors
HRTEM	High Resolution Transmission Electron Microscope
HTGRs	High Temperature gas-cooled reactors
LED	Light Emitting Diode
LWRs	Light Water Reactors
MD	Molecular Dynamics
MIAMI	Microscope and Ion Accelerator for Materials Investigations
MMCs	Metal Matrix Composites
MOSFETs	Metal Oxide Semiconductor Field Effect Transistors
PIPS	Precision Ion Polishing System
PKA	Primary Knock-on Atom
SAD	Selected Area Diffraction
SiC	Silicon Carbide
SRIM	Stopping and Range of Ions in Matter
TEM	Transmission Electron Microscope
TRISO	Tri-structural Isotropic

XTEM Cross-Sectional Transmission Electron Microscopy
ZAPMap Zone Axis Pattern Map

List of Nomenclature

$f(\theta)$	Structure factor
$F(\theta)$	Atomic structure factor
(h k l)	Miller indices of a crystal plane
R	Ion range
R_p	Projected ion range
v_0	Bohr velocity of the atomic electron
v_i	Ion velocity
$Y_{sputter\ yield}$	Sputtering yield
Z_1	Ion atomic number
Z_2	The target atomic number
Z_1^{eff}	Average charge of the ion
α	Calculated angles α from the [001]-zone to various zones
ε	Proportional to ion energy
θ	The angle electron are scattered
λ	Wavelength of electron wave
Ω	Solid angle

Acknowledgements

I would like to express my gratitude to all those who helped me during my master's study. My deepest gratitude goes first and foremost to Dr. Jonathan Hinks, my supervisor, for his constant instruction and guidance. He has walked me through all the stages of my master's study. Without him, the research done in this thesis would have taken much longer and been less significant of science.

Second, I would like to say thank you to the rest of our research group: Steve Donnelly, Graeme Greaves, Francis Sweeney and Imran Hanif. Graeme answered me a lot of questions during my experiments and solved some operation problems of MIAMI when I tried to find the ion beam. Francis explained principles of electron microscopy for me. Imran discussed with me when I get stuck, which helped me to get better understanding of my research. Thank you for helping me on this journey.

I would also like to extend my gratitude to college of Energy research, Xiamen University, who sponsored my study. I am very grateful to my tutor in China, Guang Ran, Assistant professor at Xiamen University, who gave constant support and advices on my experiments. I also appreciate Professor Ning Li and Professor Lumin Wang who provided this opportunity.

I would also like to express my gratitude to my office mates. Thank you for bringing a lot of joy and improving my English.

Finally, I owe my sincere gratitude to my family. Thanks to my dad and mum for backing me up all the way.

Abstract

SiC is an excellent candidate material for use in fusion and fission nuclear reactors. The work done in this thesis aims to understand the behaviour of SiC under He irradiation at high temperatures. Experiments of helium irradiation in 4H-SiC in temperature range of 700–900 °C have been conducted with in-situ ion irradiation facility of MIAMI.

A couple of results are derived from the experiments: The major experimental observations were the formation bubble discs. There is a critical temperature threshold around 700 °C above which much higher number density of bubble discs were formed. At 800 °C, bubble discs were observed to grow with increasing helium fluence. Growth of bubble discs was also observed when the temperature was held at 800 °C after a fluence of 3.8×10^{16} ions.cm⁻² as the bubble discs grew due to diffusion of helium and gain of vacancies. Bubble discs trended to stop growing with a mean size of 30 nm at a fluence of 6.1×10^{16} ions.cm⁻². The evolution of bubble discs was similar at 900 °C as at 800 °C. Analysis done at room temperature of experiments conducted at 900 °C revealed that bubble discs formed preferentially on the {001} and {100} planes.

1. Introduction

Silicon carbide is a compound of silicon and carbon, which have an easy chemical formula SiC. As an important structural ceramic material, silicon carbide has been widely used for over a century.

Silicon carbide has more than 250 crystalline forms [1]. The polytypes of silicon carbide are categorized by their different crystal lattice and stacking sequences along the c-axis. For instance, rhombohedral polytypes (15R-,21R-,27R- etc.), hexagonal types (2H-,4H-,6H- etc.) and the single cubic-polytype (3C-) [1], [2]. The majority of the polytypes have been investigated and their properties are well-understood [1]. Some of the polytypes can perform well under extreme conditions of irradiation and temperature, for instance, in nuclear reactor cores and extraterrestrial environments.

This introductory chapter provides a short history of SiC and its current applications, especially in nuclear industry. The motivation and details of the work undertaken in this research are then presented in the second part.

1.1 History

Silicon carbide was first reported by Sadow in 1824 [3] following which the preparation and synthesis was researched in 1885 by A.H. Cowless and E.H. Cowless [4]. The first SiC Light Emitting Diode (LED) was reported in 1907 [5].

The Lely method was used to produce single crystal SiC in 1955, putting forward a sublimation process at temperature of 2550–2600 °C [6]. SiC manufactured by purely-thermal process shows low purity and small crystallites, which are not suitable for many industrial purposes [6]–[8]. Therefore, Tsvetkov and Tsvetkov developed the seeded sublimation method in 1978, making the synthesis of large high-purity single-crystal SiC wafers possible [9].

Industrial mass production of large SiC wafer was realized and further refinement to the growth process was developed in the 1980s [10]. The excellent characteristics of SiC drove scientists and researchers to explore new applications in the 21st century.

1.2 Application

SiC has a variety of applications in different fields. SiC has been manufactured into grinding wheels and other abrasive products as excellent abrasive since the end of nineteenth century [1]. Nowadays, as a technical grade ceramic, great improvement in quality has been achieved [11]. SiC is widely used as a semiconductor material in electronics, due to its high thermal conductivity, high electric field breakdown strength and high maximum current density. It is also used as high-powered devices [12]. SiC polytypes have very low coefficient of thermal expansion ($2.7\text{--}4.5\times 10^{-6}\text{ k}^{-1}$) and no phase transition happens when they are heated, which would cause discontinuities in thermal expansion [13]–[15]. SiC is also used in resistance heating applications and flame igniters [16]. The main applications of SiC are discussed in more detail below.

1.2.1 Electronic devices

Research on SiC for electronic applications is mostly motivated by the superior combination of SiC's physical properties. It performs much better for some high-temperature, high-power, or high frequency applications compared to Si- or GaAs-based devices [17]. Though the research is driven initially for military applications, civilian industries became increasingly interesting in SiC-based electronics [17]. For instance, Schottky diodes and MOSFETs (Metal Oxide Semiconductor Field Effect Transistors) for high-temperature and high-power switching as the switch time of these components is low when based on SiC [18]–[20]. Such devices and circuits made using SiC, can be used for both military and communications systems – for instance, radar, distributed satellite arrays and unpiloted aerial vehicles [17]. Meanwhile, the petroleum industry is interested in using SiC-based sensors to explore and probe the environment around drilling equipment where temperatures can rise up to nearly 300 °C [17]. SiC electronics are being considered for a variety of applications in the automotive industry, such as engine control sensors, but the economics of relatively expensive sensors still need be evaluated before SiC electronics step into this potential market [17].

1.2.2 Non-nuclear structural materials

As a hard ceramic, silicon carbide is used as a composite and ceramic in bulletproof vests. Silicon carbide is applied in lots of high temperature kilns as support structure, such as for firing ceramics, glass fusing or glass casting [21].

1.2.3 Astronomy

Materials of the silicon carbide family are some of the most desirable candidates for telescopes in outer space [22]. These infrared astronomical telescopes are normally cooled down to a few K to achieve the required instrument sensitivity [22]. SiC has a low thermal expansion coefficient, high hardness, low density and high radiation hardness which could be made into telescope mirrors. SiC-based materials with new element infiltrated material add new characteristics and perform even better. For instance, carbon-reinforced SiC (C/SiC) materials achieve high fracture toughness and reduced shrinkage factor [23].

1.2.4 Abrasives and cutting

SiC is also used as an abrasive and for cutting in manufacturing. Since 1980s, SiC particles and whiskers have been investigated and incorporated into Metal Matrix Composites (MMCs) [24]. These SiC-reinforced MMCs demonstrate excellent wear and abrasion resistance [24]–[26]. The products are widely employed in automotive/aircraft brakes [27]–[29] and in piston engines [30] to improve wear resistance.

1.2.5 Nuclear materials

Facing the increasing energy crisis, scientists are looking for promising sources of power. Nuclear energy is one possible solution. Not only does the nuclear fuel have extremely high energy density, but it also massively reduces the carbon emissions of energy production compared to the burning of fossil fuels. Silicon carbide is a candidate material for use in nuclear reactor cores, owing to its superior irradiation tolerance, which is generally associated with properties such as low thermal expansion, high thermal conductivity, good thermal structure stability, good thermal shock resistance and good chemical inertness [17, 32].

1.2.5.1 Nuclear fuel cladding and coatings

Tri-structural isotropic (TRISO) particles have been used as nuclear fuel in High Temperature Gas-cooled Reactors (HTGRs), such as pebble bed reactors, for several decades [31]. And now they are being considered for used in fluoride-salt high-temperature reactors (FHRs) [32, 33] and light water reactors (LWRs) [34].

For HTGRs applications, a large number of these TRISO fuel particles are either spheres for pebble bed fuel or cylindrical compacts for prismatic fuels [35]. These fuel forms have been successfully deployed in Germany in the 1960s [9] and are now being produced and evaluated in the US as well as in China and other countries [4]. The typical TRISO fuel particle contains a couple of different functional layers and the fuel kernel. Fig. 1 shows a schematic representation of the TRISO fuel particles [32].

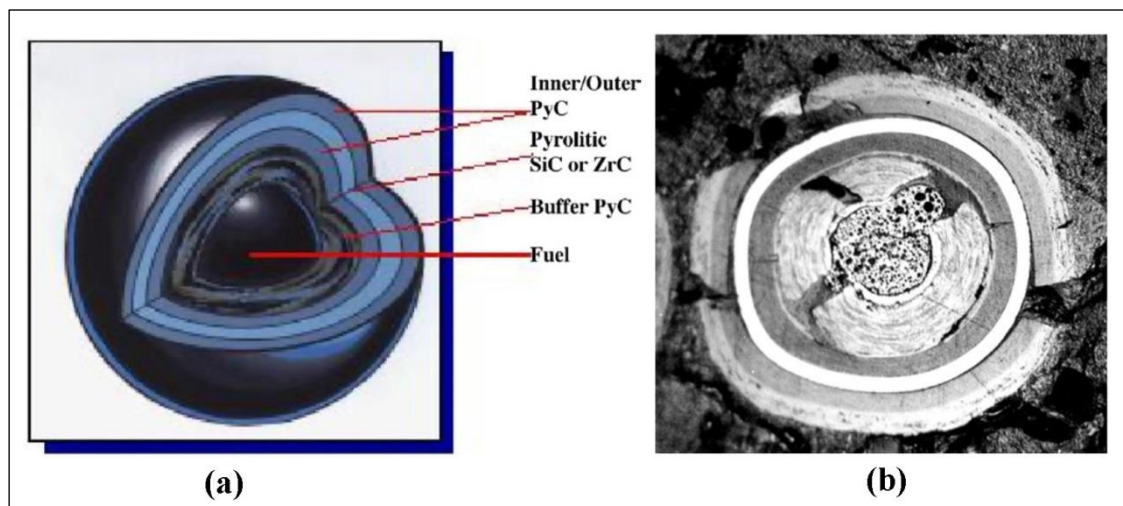


Fig 1.1: Schematic structure of the TRISO fuel particles (a) and irradiation induced crack (b) (reproduced from [32]).

The SiC layer of the TRISO particle is considered to be the most important structure [32]. The SiC layer holds the particle together under the high pressures generated during fission, providing structural support to bear the stresses produced by irradiation induced structural changes. Therefore, the SiC layer acts as “a pressure vessel” for the fuel [36].

1.2.5.2 Structure support in nuclear reactors

SiC-based ceramic composites are being considered as structural materials in nuclear reactors for applications such as core support, fuel channel boxes, prototype control rods (as shown in

Fig 1.2) [37]. Its application has been proposed in all types of nuclear fission reactors, which including LWRs, High Temperature Gas-cooled Reactors (HTGRs), Gas-cooled Fast Reactors (GFRs) and Fluoride-cooled High Temperature Reactors (FHRs). SiC-based materials have also been extensively considered as replacements for metallic alloys in some components [37].

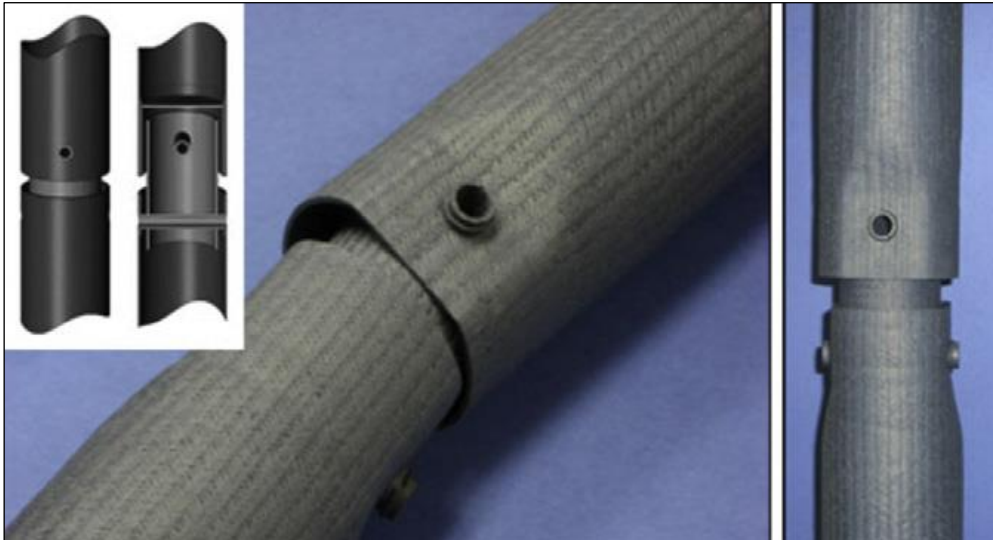


Fig1.2: articulating connections of control rods made of Prototype SiC/SiC (reproduced from [37]).

1.2.5.3 Immobilization of nuclear waste

SiC could be used to immobilize the irradiative atoms from the reprocessing of spent nuclear fuel, such as ^{137}Cs , ^{14}C , ^{129}I and ^{85}Kr [38]–[40]. Due to the extraordinary low fission product diffusivities, high chemical stability and high radiation resistance, Some polytypes of SiC are excellent materials to retain the radionuclides in a geologic repository [38].

1.2.5.4 The first wall candidate for fission reactor

SiC-based materials are considered as candidates for low-activation composites for fusion reactor components, such as the first wall which faces extremely high temperature plasma, the divertor which remove the waste and impurities from the plasma [41]–[43].

1.3 Motivation

The current GenIII nuclear reactors operate at temperature less than 625 K. For the innovative GenIV fission reactors and for fusion reactors, the materials would confront harsher operating environments. Fig 1.3 shows the expected operating conditions in terms of temperature and atomic displacements of these new reactors [44]. Since the service lifetime is expected to be at least 60 years, the maintainable function under high temperature and high neutron fluence in the reactors poses a great challenge of materials.

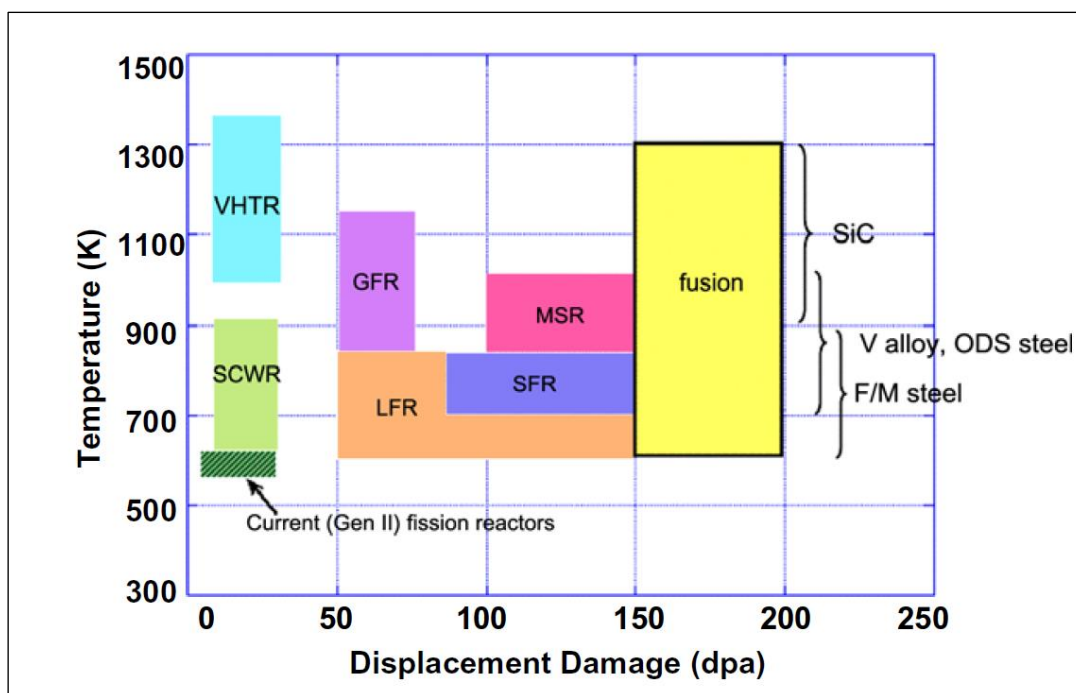


Fig 1.3: Expected operating temperature and displacement dose for different nuclear fission reactor systems (dpa means displacement per atom) (reproduced from [44]).

As a promising candidate material, SiC has been researched for more than 50 years. However, as summarised by Riccardi [45], there are still critical issues to be solved for the application of this material in harsh environments. In this work, the dynamical changes during high temperature helium irradiation on SiC were investigated to understand the underlying mechanisms. Helium irradiation caused bubbles and bubble discs which may result in a degradation of the material properties. These formations will decrease the toughness thus increasing high temperature creep and swelling [37], [46]. They could also be

a nucleation sites for cracks which ultimately lead to the premature failure of the materials [37].

1.4 Work undertaken

The main purpose of the work was to simulate the helium irradiation of SiC in the nuclear reactors. As an important product of the transmutation, helium was implanted into 4H-SiC at 700 °C, 800 °C and 900 °C. Helium bubbles and bubble discs are found in irradiated 4H-SiC under these conditions. The characteristics of the bubble discs were researched, which included the growth mechanism, size, orientation, effect of irradiation fluence and temperature. Utilizing the in-situ ion irradiation technique, it was possible to investigate the dynamic evolution on the nanoscale in real-time.

There are few in-situ ion irradiation studies of helium bubble discs in SiC in this temperature range. The information and conclusions derived from these experiments are of great significance for the application of SiC in extreme conditions and in particular in the nuclear industry.

2. Literature Review

This chapter gives a review of the relevant literature on SiC including its structure and properties, mechanism of ion-solid interactions, electron and helium radiation effects on SiC, temperature affects and the TEM technique. This literature review aims to provide evidence and to situate the current study within the relative area.

2.1 Silicon carbide

2.1.1 Structure and valence bond

The fundamental structural unit of SiC is a primary co-ordinated tetrahedron, SiC_4 or CSi_4 , as shown in Fig 2.1(a). The four bonds between carbon and silicon are nearly purely covalent. A 12% ionic contribution to the bonds can be estimated from Pauling's formula where a Si atom has the positive charge [47].

Silicon carbide has more than 250 polytypes. The polytypes are classified as α -SiC (hexagonal and rhombohedral polytypes) and β -SiC (cubic polytype). All the polytypes of silicon carbide can be expressed as a typical hexagonal axis system, which have the c-axis normal to three equivalent axes a, b and d having angles of 120° with each other. All the polytypes share identical layers perpendicular to the hexagonal axis (c-axis) but with different stacking sequences [2]. The positions of the silicon and carbon atoms in projection can be seen in Fig. 2.1.

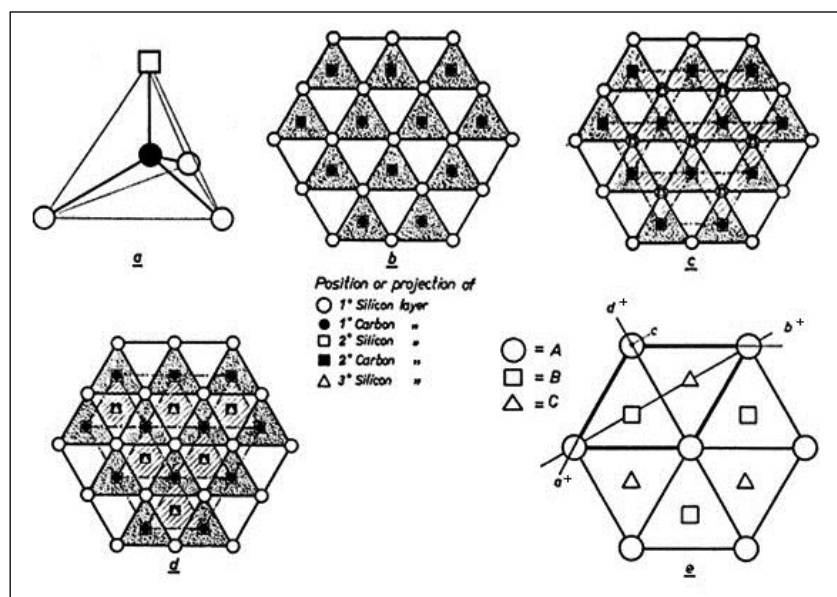


Fig 2.1: Position and projection of silicon and carbon atoms in SiC

- a) elementary Si-C tetrahedron;
- b) projection of one tetrahedral layer;
- c) projection of two adjacent tetrahedral layers of the cubic;
- d) projection of two adjacent tetrahedral layers of the hexagonal; and
- e) projection of the different positions of the atoms (reproduced from [2]).

2.1.2 Properties of SiC

SiC has a number of properties which make it ideally suited to many applications. It has low density, high strength, high thermal structure stability, low thermal expansion, high hardness, high elastic modulus, good thermal shock resistance, chemically inert and excellent radiation resistance [16], [48].

There are some small differences in the properties between the different polytypes. Some basic parameters of main SiC polytypes are shown in Table 2.1 [49].

Table 2.1: Fundamental properties of common silicon carbide polytypes [49].

Material Property	Polytype		
	3C(α)	4H(β)	6H(β)
Density (g.cm ⁻³)	3.21	3.21	3.21
Lattice Parameters(Å)	a = 3.083	a = 3.081	a = 3.081
	b = 7.551	b = 10.084	b = 15.12
Space Group	T _d ² (F43m)	C _{6V} ⁴ (P6 ₃ mc)	C _{6V} ⁴ (P6 ₃ mc)
Thermal Conductivity (W.cm ⁻¹ .K ⁻¹)	4.9	4.9	4.9
Bulk Modulus (10 ⁻³ Bar)	2.22	2.23	2.04
Band Gap (eV)	2.40	3.26	3.02
Coefficient of Thermal Expansion ($\times 10^{-6}$ K ⁻¹)	2.74 (at RT)	$\bar{a}_{11}=4.47$ $\bar{a}_{33}=4.06$	4.25

2.2 Ion-solid interactions

The mechanism of the interaction between energetic particles and solid materials has been widely explored over the last 70 years and is fundamental to many experimental techniques. Mechanical, optical, electrical and magnetic properties of materials can all be affected once energetic particles interact with them. The section below covers the main principles of ion-solid interactions which are highly relevant for the research detailed in following chapters.

2.2.1 Energy loss mechanism

The ability of a solid to slow an energetic particle is usually defined as the “stopping power” d_E/d_x which gives the energy transfer per path length of the particle along its trajectory. The total stopping power is divided into two basic energy transfer mechanisms: nuclear stopping and electric stopping [50].

2.2.1.1 Binary collision approximation

Binary collision approximation (BCA) has been used as a fundamental assumption of many theory and models in the area of the ion-solid interaction, as well as the computer simulations in this area [51]. The BCA separated the interactions between particles into a collection of dualistic collisions. BCA only considers the energy loss caused by nuclear stopping power and the interaction between the incident particles and target atoms nuclei is regarded as elastic [51].

2.2.1.2 Nuclear stopping

Nuclear stopping means the average energy loss of the incident particles produces from elastic interactions with target nuclei [52]. The principal effect of nuclear collision is that kinetic energy is transferred to the knock-on target atoms. These atoms might be displaced from their original lattice sites (if the transferred energy exceeds the threshold energy for the ballistic displacement of the target atom) and structural defects might be created, e.g. vacancies and interstitials.

2.2.1.3 Electronic stopping

Electronic stopping power is due to interactions with electrons of the target atoms, which may lead to excitation of the electrons and ionization of atoms. Electronic stopping power depends strongly on the ion velocity and the charge density on the ion and on the target atoms.

In addition to slowing the energetic particle, electronic interactions can affect the actual charge state of the incident particle, which is in matter of continuously fluctuating and balance between electron loss and electron attachment.

The average charge of the ion, which depends on its velocity, is called its “effective” charge, Z_I^{eff} . In a low energy state in which the ion velocity, v_i , is much lower than the Bohr velocity of the atomic electron, v_0 , the ion will capture an electron from the target and

neutralize [52]. Nuclear energy loss dominates at these velocities and diminishes as $1/E_0$. The electronic energy loss is increasing with the rising of the ion's velocity [52]. When the velocity is in the range from approximately $0.1v_0$ to $v_0Z_1^{2/3}$, the electronic energy loss is approximately proportional to velocity v_i [52].

At higher velocities ($v_0 \gg v_0Z_1^{2/3}$), electrons are stripped from the incident ion (or energetic PKA, etc.) and finally the ion can be regarded as a naked positive nucleus which possesses a higher velocity than the mean orbital velocities of the electrons in the shells or subshells of the target atoms. At this stage, the cross-section of the electronic stopping diminishes with the increasing velocity and the stopping values are in direct proportion to $(Z_1/v_i)^2$.

Fig 2.2 shows the relationship between parameter $\epsilon^{1/2}$ and the cross sections of nuclear and electronic stopping. The reduced energy (ϵ) is directly proportional to the energy of incident ions and $\epsilon^{1/2}$ is directly proportional to ion velocity. Both the electronic and nuclear stopping powers increase to their peaks then decrease. The electronic energy stopping reaches its peak at values of $\epsilon^{1/2}$ which are higher than the nuclear stopping maximum, as it is presented in Fig 2.2. The nuclear interaction can be viewed as a collection of single elastic collisions between the incident particle and the target-atom nuclei, whilst the electronic interactions can be described as a continuous viscous drag process between the incident particle and the electron sea surrounding the target nuclei. The reduced nuclear and electronic stopping cross sections in relationship with $\epsilon^{1/2}$ are shown in Fig 2.2 [53].

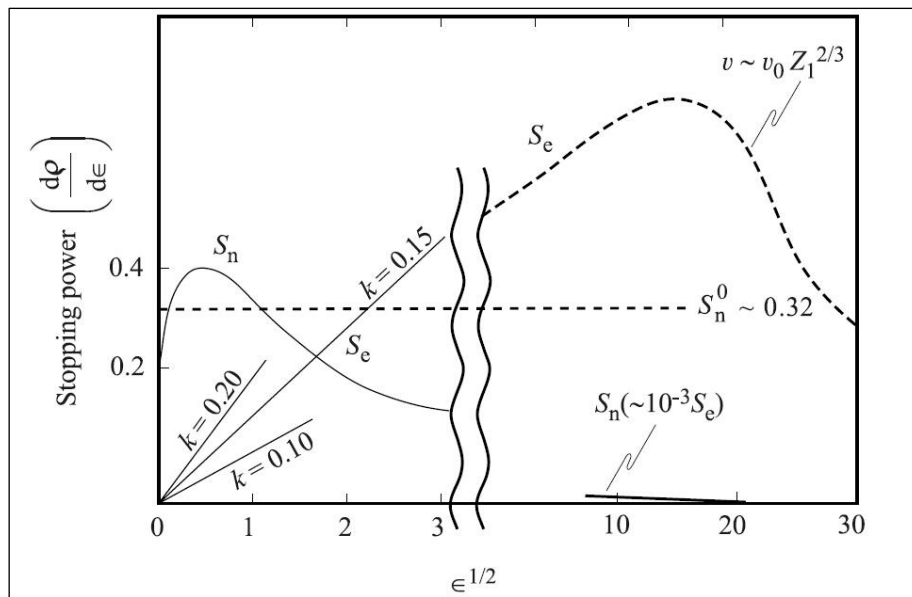


Fig 2.2: The cross sections of nuclear and electronic stopping as a function of $\epsilon^{1/2}$ (reproduced from [53]).

2.2.2 Ion range and distribution

When the ion enters into the target, it undergoes collisions with the target atoms and does not follow a straight path because of these collisions. As shown in Figure 2.3, the actual path length travelled by the ion is called the range, R , and penetration along the direction parallel to that of the incident ion is given as projected range, R_p .

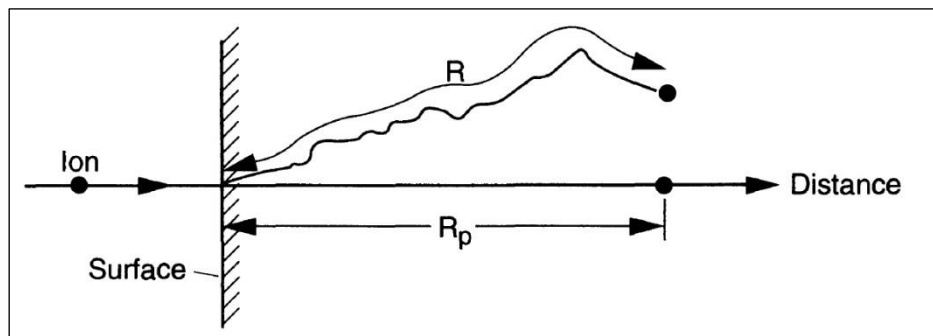


Fig 2.3: An ion incident on a material penetrates with a total path length, R and gives a projected range, R_p , along the direction parallel to the incident direction of the ion (reproduced from [53]).

2.2.3 Channelling

2.2.3.1 General

When it comes to crystalline materials, the ordered arrangement of atoms greatly affects the ranges of ions and the resulting radiation damage. Channelling is where the ion trajectory is well aligned along an open crystallographic direction. The stopping power of the particles in the certain direction is much lower than other directions and the ions will travel deep in the target with less collision, as shown in Fig 2.4 [54].

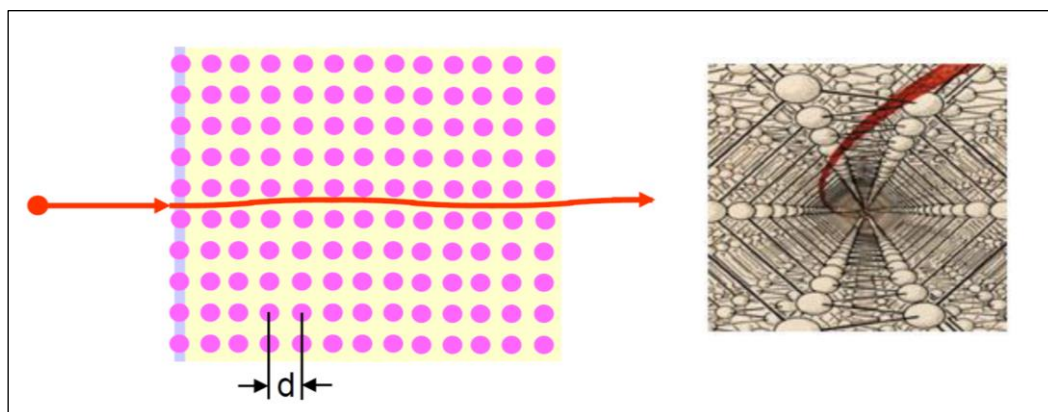


Fig 2.4: The schematic of channelling (reproduced from [54]).

In monocrystalline materials, the channeling directions are usually the low index crystalline axes and it is often difficult to avoid channeling in single crystalline materials. [55]. The main parameters such as the ion atomic number Z_1 , the ion energy E_c , the target atomic number Z_2 , the orientation of the substrate, the crystal lattice type and spacing and the vibrational amplitude of the target atom (related to temperature), have a distinct affect on the channelling and range distribution. The channeled particles will cause fewer displacements of target atoms and have a longer range of incident ions, which is different from conventional collision theory [55].

2.2.3.2 Channelling in SiC materials

The channelling will likely occur when the ion travels along a low index crystallographic direction. Ivan Chakarov and co-workers investigated the Al^+ implantation ranges in 6H-SiC along the [001] axis and found they were more than twice as deep relative to the random off-axis implantation. Furthermore, they found some proportion of the channeled ion would get stuck in a disordered layer where the dechannelled Al^+ ion stop and cause a plenty of the defects. Thus an intermediate damage random peak ($\sim 2 \mu m$) appears at lower depth layer than the true channeling peak layer ($\sim 4 \mu m$) [56].

4H-SiC has several major channelling directions including the [001], [113] and [110]. Implantation of Al^+ along the [113] direction was found to be three times deeper compared to implantation along the [001] direction and five times deeper compared to random off-axis direction [57].

2.2.4 Radiation damage

When the energetic ions are introduced into the target, they collide with target atoms and the energy is transferred during the collisions. A target atom which is displaced from its lattice sites by an incident ion is called a Primary Knock-on Atom (PKA). Energetic ions could create many PKAs which can then interact with further atoms. The collisions result in displacement of lattice atoms from their initial sites creating vacancies, interstitials and other types of lattice defects. This is called “radiation damage”. For high energy particles, electronic energy dissipation can result in atomic displacements [51, 53].

2.2.5 Collision cascades

Nuclear collisions by an incident ion transfers energy to the target atoms and forms primary recoil atoms. If the transferred energy from the incident ion is large enough, the PKAs will go on colliding with other atoms and cause more displacements. The collision process between incident atoms and PKAs, PKAs and other lattice atoms which create a number of new generations recoil atoms is called a “collision cascade”, as shown schematically in Fig 2.5.

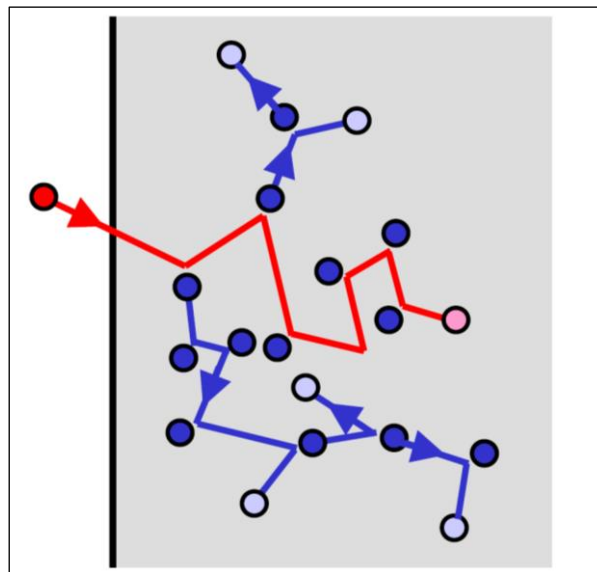


Fig 2.5: Schematic of an incident ion trajectory and related recoil atoms with their individual trajectories and the resulting collision cascade (reproduced from [58]).

2.2.6 Spike

Spikes in the context of ion-solid interactions consist of displacement spikes and thermal spikes. They are discussed in the section below.

2.2.6.1 Displacement spikes

A displacement spike means a high density cascade where the majority of atoms in the area are temporarily in motion. The area is highly damaged after the displacement spike. A displacement spike consists of a core of vacancies and a surrounding jacket of interstitial atoms. Brinkman produced the first schematic of the displacement spike, shown in Fig 2.6 [59].

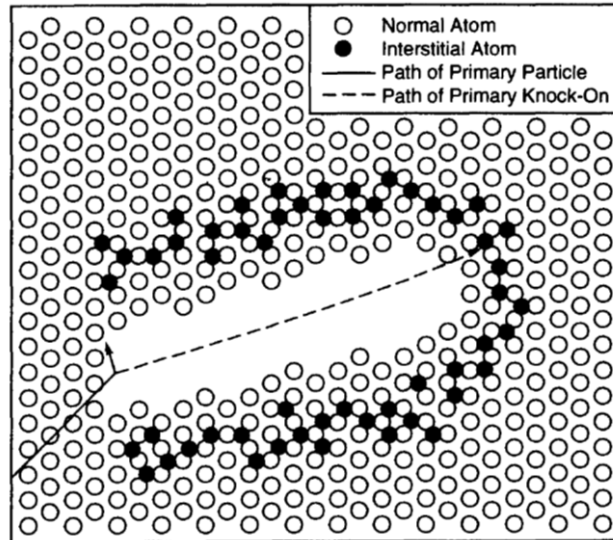


Fig 2.6: Schematic of a displacement spike (reproduced from [59]).

2.2.6.2 Thermal spikes

In general, thermal spikes means the temperature elevation of the surround material in a collision cascade [58]. The thermal spikes just last several picoseconds [52]. Then, the volume quenches to ambient temperature [52].

2.3.7 Phase stability and transformation

Ion irradiation can affect the stability of the phases of a target material and even change the phases. Local enrichment or depletion of solute is possible to happen during the irradiation. Irradiation can also cause lattice disordering, phase dissolution, nucleation and growth of distinct phases. Further, irradiation can create metastable phases and amorphization [53].

2.3.8 Sputtering

When a collision happens near the surface of target materials, the atoms in the near-surface layers obtain sufficient energy from bombardment and overcome its binding energy to the surface, so that they will escape from the target face. The process is called sputtering. A schematic of sputtering in the cascade is given in Fig 2.7.

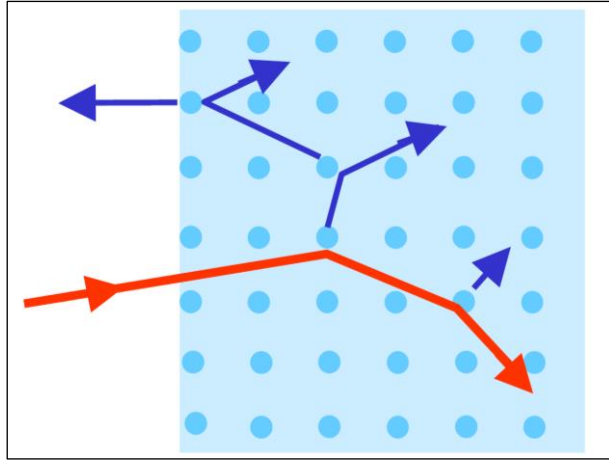


Fig 2.7: A schematic presentation of sputtering (reproduced from [58]).

The sputtering yield is a parameter defined as the number of ejected atoms per incident energetic particle [52]:

$$Y_{sputter\ yield} = \frac{\text{mean number of emitted atoms}}{\text{incident particle}} \quad (2.1)$$

The sputtering yield typically varies in the range 0.5–20, depending on the incident angle and energy of the incident ion, the masses of the ion and target atoms and the surface binding energy of the target atoms [52]. For crystalline materials, the orientation of the crystal with regard to direction of irradiation can affect the sputtering. For in-situ microscopy, sputtering is an important factor, because we deal with very thin samples and changes near the surface must be considered.

Sputtering could cause a significant erosion of material and can thus be a problem. However, it can be utilized for TEM sample preparation. For instance, ion beam milling is a final thinning process which is based on sputtering by ion irradiation [60]. Also, sputtering is widely used as one of the processes for depositing thin films on suitable substrates in the semiconductor industry [61].

2.3.8.1 Sputtering of SiC

Sputtering of SiC has been widely researched with different incident atoms and various energies. W. Eckstein and his co-workers investigated the sputtering yields of SiC for light ions such as H, D and He, because of their importance in nuclear fusion and fission reactors

[62]. J.Roth found the sputtering yield of SiC for He⁺ is about 10⁻² and significant temperature dependence is found at low energies (600 to 7500 eV) [63]. Plenty of research has been conducted on focused ion beam sputtering of SiC [64]. Computer simulation of SiC sputtering by He⁺ has also been performed. T.S. Pugacheva et al. found that for light incident particles, the sputtering is significant when the incident ions have the energy of 3–5 keV [65]. In Gernot Ecke's work, the simulation of sputtering yields for SiC fits the existing experimental data very well. However, the simulation results depends on the input parameters of SiC [66].

2.3.9 Computer simulation

Computer simulation can be a very effective approach for the analysis of ion-solid interactions. By simulating on the computer, we can not only predict the damage distribution, ion range and energy deposition, but also gain an improved understanding of the spatial and temporal development of the interaction. There are mainly two types of computer simulation which are widely used nowadays: the Binary Collision Approximation (BCA) method and the Molecular Dynamics (MD) method [52].

The BCA method considers that the incident ion goes through a sequence of independent binary collisions with the target atoms. In the BCA approach, a single collision between the ion and the atom is considered at a time using a classical scattering integral between two colliding particles. For those whose energies are less than the displacement energy, the BCA code would consider the ballistic feature of the cascades, such as replacement-collision sequences and the focused-collision sequences [53].

There are a plenty of computer programs, such as: TRIM [67], EVOLVE [68], SASAMAL [69], DINA [70] and CASCAD [71]. Most of these programs are based on a combination of BCA method and Monte Carlo code. Monte Carlo code is a computational algorithm that repeats doing the sampling in a random way and then does the probability statistics to get the distribution of probability. The majority of the models consider all the material as amorphous solids (no long-range order), they possess a great deal of distinct advantages: running fast and good simulating result which fits the experiment data well [65].

SRIM (Stopping and Range of Ions in Matter) is the most popular software in this area. It can estimate the damage distribution, sputtering, ion penetration depth and so on. SRIM has been used in this work to estimate the damage distribution and ion range of He implantation in the experiments.

The molecular dynamics method provides a more precise and realistic description of the atomic interactions in cascades. The MD simulations allow the well-defined lattice atom positions in crystalline structure to be taken into account and the changes of all the atoms through the cascade process. The analysis calculates the force (a function of distance) between the simulated atoms from their interatomic potential functions. Then the simulation obtains the acceleration and motion by using Newton's laws of motion. The program solves these equations numerically in a very short period of time and then iterates. Therefore, the approach of molecular dynamics is computationally expensive but extremely useful for particles interaction simulations in small volumes [53].

2.3 Transmission Electron Microscope

The transmission electron microscope is a powerful scientific instrument which can provide a wide collection of characterization methods with high resolution. Indeed as nanotechnology and related areas capture the imagination of both the industrial and the scientific communities, it is progressively believed that the TEM is the central tool for characterization of nanoscale materials and devices [72].

2.3.1 TEM sample preparation

Nowadays, most all kinds of materials are investigated in the TEM, including metals alloys, ceramics, semiconductors, polymers, glasses and composite mixtures of the materials. The limiting factor in the investigation of the materials using TEM is often sample preparation, rather than the resolution of the electron microscope [73] [74].

TEM specimen preparation itself is a very broad subject. Scientists use various ways: electropolishing, chemical etching, ion milling/ focused ion beam (FIB), grinding and crushing, cleaving and so on. Each of methods has merits and drawbacks.

Elceropolishing and chemical etching are widely used to make electrically conductive specimens, for example, metals and alloys. Certain voltages and suitable solutions for different material are needed [72]. Ion milling is another important technique to make TEM samples. It is applicable to both electrically conductive and nonconductive materials. A kind of commercial product called Precision Ion Polishing System (PIPS) developed by Gatan Inc. was used in our sample preparation and the processes are detailed in the section 3.2. Ion Focused ion Beam (FIB) can be considered as a scanning electron microscope (SEM)

cooperating with a built-in ion gun [72]. Ion mill would inevitably induce some irradiation damages into the samples [72] while cleaved specimens for TEM are damage-free ones [75], [76]. Williams and Carter has details these methods in chapter 10 of their book [72].

2.3.2 TEM for irradiation damage investigation

Electron-beam irradiation using transmission electron microscopy (TEM) is an important techniques for investigating radiation effects of materials [77]. TEM has the ability to observe materials with high resolution and high magnifications. It could be used to investigate the radiation damage on a nanoscale. Facilities which combined TEM with ion beams provides the possibility for scientists to do TEM with in-situ ion irradiation [78].

2.3.3 Electron irradiation in the TEM

Although TEM make advantages of the short wavelength of the electron beam, the electrons are one type of ionizing radiation. In general, electron beam irradiation produces three types of radiation damage: (1) atomic displacements because of the energy transfer resulting from interactions between electron of then beam and nucleus of specimen atoms; (2) atomic displacements caused by the interactions between the electrons of the beam with electrons of the specimen atoms; and (3) beam heating [79]. Electron irradiation can damage the specimen, for example, polymers, organics, certain minerals and ceramics [72].

Irradiation effect on SiC by electron is well discussed in the section 2.4. In-Tae Bae et al. discussed about the main three factors of the electron beam irradiation on SiC in their publications: the fluences/fluxes, the voltage (energy of the electron) and temperature dependence [77]. Generally, higher fluences and higher voltages will lead to greater irradiation damage [77].

2.3.4 TEM with in-situ ion irradiation

An ion beam is directed from implanter or ion accelerator onto the specimen in the microscopes in a TEM facility with in-situ ion irradiation. One of the biggest advantages is that TEM facilities with in-situ ion irradiation are able to capture the dynamic evolution of the materials during the ion irradiation, which help the researchers to analyse and understand the mechanism under the phenomenon. The TEM facilities with in-situ ion irradiation are often used to simulate neutron irradiation damage in the nuclear reactors. The irradiation

damages equivalent to the DPA level irradiating by high neutron doses can be achieved in a short time frames. Several tens of such facilities have been built over the last fifty years. In Hinks's paper [80], he reviews the specific technique and the details of the facilities over the world.

2.3.5 TEM for SiC

Different TEM modes and techniques are used to investigate SiC materials. Bright field imaging, dark field imaging, selected area deflection pattern, weak-beam dark field imaging, HRTEM, electron microscope combined with Energy Dispersion X-ray spectrometry (EDX) and Electron Energy Loss Spectrometry (EELS) are employed [11]. The evolutions of SiC, such as the structure transformation of SiC crystalline defects, bubbles formation, dopant deposition, amorphization, Chemical composite changes and self-organization were investigated with these techniques [22], [42], [43], [77], [81]–[87].

2.4 Irradiation effects on SiC

2.4.1 Electron irradiation

The research on electron irradiation is important for the TEM of SiC. Electron irradiation is relatively easy to perform, with many universities and research institutes possess equipment capable to generating high-energy electrons. Below, the literature is reviewed across different electron energy ranges.

2.4.1.1 100–160 keV

Barry's work gives the displacement threshold energy, E_d , of a carbon atom in SiC is 21.8 ± 1.5 eV and the minimum electron energy required to generate a displacement damage is estimated to be 108 ± 7 keV [88]. The corresponding electron energies necessary of the C and Si atom displacement is shown in Fig 2.8. while Bardeleben et al claims that 100-150 keV for C atoms and 220-300 keV for Si atoms are reasonable as the lower limits [89].

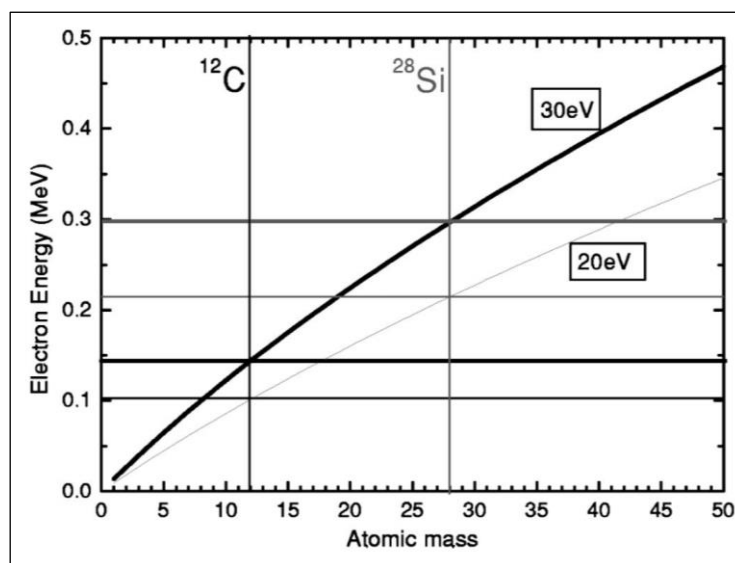


Fig 2.8: schematic of minimum required energies of electron, which transfer energy of either 20 eV or 30 eV to an atom of atomic mass, A , in an individual collision. For example, if the displacement energy of the atoms is 30 eV, displacements of Si and C require electron energies of ~ 150 eV and ~ 300 eV, respectively [89].

In 4H-SiC, it is believed that at an energy of 116 keV, the electron trap concentration increases linearly with the fluence of the electrons, which may be caused by carbon

displacement [90]. Katsunori Danno and his colleague claimed that the irradiation induced electrons trap centers did not decrease until annealing above 1600 °C [90]. The C interstitial atoms, C_i , have high mobility and are able to migrate outside of the electron irradiation area and the vacancies remain within the region of electron irradiation [91], [92].

2.4.1.2 200-400 keV

The Si atom displacement and Si Frenkel pair defects (Si vacancies and Si interstitials) took place at an electron beam energy above 200 keV [89], [93]. Although in Steed's work Si Frenkel pair defects appeared at energies above 250 keV [94]. Electron irradiation at 200 KeV will induce amorphization on 6H-SiC and 4H-SiC at or lower than room temperature (295K) by the accumulation of defects resulted from direct atomic displacements. Ishimaru and his co-workers researched amorphization mechanisms and concluded that amorphization is caused by the accumulation of interstitial carbon atoms [95]. Bae investigated that the defect recovery increases during irradiation, due to the temperature increases and ionization effects [96]. Bardeleben claimed that at room temperature, 300 keV electron irradiation induced carbon vacancy-hydrogen complexes were predominant found in high purity intrinsic and p-type and SiC, although the energy level is large enough to knock out Si atoms [87].

With the help of Deep Level Transient Spectroscopy, C-displacement-related defects, HK_0 , HK_2 and Si-displacement-related defects, EP1, EP2, were observed in SiC irradiated in this energy range, while other deep level Si-displacement-related defects centers EP3 and EP4 were only observed in the samples irradiated by energy of 400 keV. Si-displacement-related defects trended to be annealed out above 950 °C, while carbon-displacement-related defects included complexes stayed stable [93].

2.4.1.3 >400 keV

Higher energy electron irradiation introduces more complicated defects in the SiC structure. Clusters of both vacancies and interstitials are shown to form following irradiation with electron energy of between 800 keV and 1 MeV [97–99]. In Chen and co-workers's detected that the generation of the deep level defects after high electron irradiation, named as ED1, E_1/E_2 and E_i , is mainly due to the displacement of the C atom [100]. The reason of generation stay the same as the research with the energy range of 200–400 keV above [87], [93], [95, 96]. The TEM observation with EELS showed that preferential displacement of carbon resulted in silicon-silicon bonding and no carbon-carbon bonding was detected in Asaoka's experiment

[101]. Electron induced amorphization in SiC occurred at electron energies of up to 2 MeV in Inui's work [102]. The electron trapped defects reduced the performance of SiC diodes in this energy range [103].

2.4.2 He ion irradiation

He ion irradiation effects are influenced by several parameters: the ion energy, ion flux and fluence, crystallographic orientation and sample temperature. The effects are reviewed below with a focus on the formation of bubble platelets and bubble discs in SiC.

2.4.2.1 1-10 keV

Bubbles have been generated by 2–3 keV helium irradiations in SiC at temperatures above 1000 °C. The bubbles size increased with irradiation temperature and Hojou observed the precipitated bubbles were aligned preferentially along {001} basal planes [82]. 8 keV helium irradiation of the SiC in Sugiyama's experiment revealed carbon concentration reduced in the vicinity of the SiC surface and the C-C bonds enriched on the SiC surface, although the exact depth was not mentioned in this paper. [104]. 10 keV He was implanted into 100 nm SiC in Ohy's in-situ irradiation experiments. Amorphous areas are formed at room temperature and helium bubbles are generated both in amorphous areas and in crystal structure. At 1000 °C, bubble precipitated in crystal structure [105]. Preferential bubble precipitation and growth were found along the c-planes. At higher fluences, the number of bubbles increased, and their position became more random within the lattice [105].

2.4.2.2 10-160 keV

Barot revealed 50 keV He irradiation induced phase changes from bulk c-SiC to α -SiC and amorphous phase with fluences of 5×10^{15} to 1×10^{17} ions.cm⁻².s⁻¹ at room temperature. Then an elevated irradiation temperature of 600 °C avoided amorphization. The subsequent annealing to room temperature led to the relaxation of surface strain and the formation of helium platelets. The transformation from platelets to clusters of bubbles was observed by using XTEM, which was attributed to the motion of vacancies in the paper. The growth of bubbles and stacking faults also resulted in swelling at surface observed by AFM [106].

No amorphous layer was generated in 6H-SiC samples irradiated to a fluence of 3×10^{16} ions.cm⁻² with 100 keV He irradiation at 327 °C, due to the dynamic annealing [107]. The

damage areas partially recovered with the increasing annealing temperature, which was studied by optical transmittance technique [107]. TEM observation showed lattice defects were not completely recovered because of the existence of helium bubbles. Raman spectra indicated that the activation energy for bond polarizability was about $0.172 \pm 0.003 \text{ eV}$ [107].

Bubble discs were detected in 4H-SiC implanted with 30 keV He^+ ions to $2.5 \times 10^{16} \text{ cm}^{-2}$ and annealed at 800 °C for 30 minutes [108]. The author concluded the overpressure state of He/vacancy clusters caused the planar bubbles to grow on low-index planes. The platelets-to-bubble discs transformation happened when their size exceeded a critical value. A simple model was presented to explain the formation of helium platelets/discs. The model was based on a frozen matrix assumption that ignored the long-range movement and clustering below the temperature of vacancy mobility [108].

2.4.2.3 >1 MeV

A comparison of defects was made between α -SiC and β -SiC after 15.7 MeV helium irradiation. It turned out that disk-shaped clusters of bubbles preferentially form along {001} habit planes in hexagonal α -SiC and on {111} planes in cubic β -SiC [109], [110]. Helium platelets were formed at ambient temperature by 26.3 MeV helium irradiation with a fluence of $2.26 \times 10^{22} \text{ ions.cm}^{-2}$ and no transformation of platelets happened in Chen's work [81]. After annealing to 1500K, helium platelets transformed to discs of spherical bubbles with dislocation loops [81].

2.5 Diffusion in SiC

It is well believed most species have a low diffusion coefficient in SiC [111], [112]. Temperature, implanted atom and defects may all affect diffusion processes in SiC. Here we give a review of self-diffusion and He diffusion in SiC which are both of direct relevance for the evolution of helium bubbles and helium bubble discs in the experiment performed as part of the current work.

2.5.1 Self diffusion

Hong measured self-diffusion in pure and n-doped α -SiC single crystals by using isotopic tracing the temperature range of 1900–2300 °C. The activation energy for the migration of C in pure and n-doped α -SiC was found to be $\sim 7.41 \text{ eV}$ and $\sim 8.20 \text{ eV}$ [113], respectively.

Similarly, the activation energy of Si in pure and n-doped a-SiC was about 7.22 eV and 8.18 eV, respectively [114]. Rüschemschmidt investigated the Si and C diffusivity was between 1723 °C and 1923 °C. The activation energy of C and Si was given around 7~10 eV [115].

In a lower temperature range of 650–850 °C, C atoms diffused into Si substrate to create SiC films. C preferentially occupied substitutional sites below 750 °C, but both interstitial and vacant sites above 820 °C [116].

2.5.2 He diffusion

Monitored by mass spectrometry, Jung et al. got He diffusion coefficient D for temperature of 527–777 °C in his work, which is written as below:

$$D [m^2/s] = 1.1 \times 10^6 \exp(-1.14/kT) \quad (2.2)$$

The activation energy was considered as 1.0 eV below 1000K and 1.8 eV above 727 °C [117]. Sasaki gave that the activation energy of helium diffusion in a neutron irradiated SiC at temperature 700-950 °C was ~1.2 eV [118]. In Pramono's work, the helium diffusion coefficient in neutron irradiated SiC stayed the similar function 750-1260 °C, given as:

$$D [cm^2/s] = 1.38 \times 10^{-10} \exp [-0.91 \pm 0.07 (eV/atom)/kT] \quad (2.3)$$

The activation energy of helium diffusion was around ~0.9 eV. Pramono concluded that helium diffusion mechanism changed to migration of vacancies above 1260 °C to explain the accelerated migration of vacancies [118]. It also was reported that vacancy mobility became possible, when the temperature exceeded the critical value (~927 °C) [119]. Zhang and his colleagues calculated the activation energy for helium diffusion in SiC to be 1.1eV when they established their model of formation of helium platelets as described above in section 2.4.2.2 [108].

3. Experimental Methods

3.1 Bulk materials

The material used in the experiments was 4H (four-hexagonal) polytype of silicon carbide. The SiC wafers were acquired from Cree (USA). The wafers have a diameter of 76.2 mm, a thickness of 344.7 μm and resistivity of 0.021 $\Omega\cdot\text{m}$. The orientation of the surface was 7.88° off the (001) plane.

3.2 TEM specimen preparation

TEM specimen preparation is a broad area and there are various ways to make specimens. The correct method to choose depends on the information you need, time constraints, availability of equipment and the materials. This section details the preparation of 4H-SiC TEM specimens for this study.

3.2.1 Cutting of bulk material

The SiC bulk material was first stuck on a PTFE block with wax. The PTFE block was loaded into a Well 3241 diamond wire saw. Then, a 0.3 mm diamond wire saw was used to cut SiC into 1.8×0.7 ×0.3 mm pieces.

3.2.2 Mechanical polishing

A tripod polisher, originally developed by IBM, was used in this procedure [120]. The SiC pieces were attached on a Pyrex stub and then the stub was mounted in a hole by two screws. The heights of the tripod legs are adjustable to obtain the required wedged angle of the specimen. The tripod and Pyrex stub is shown in Fig 3.2. The milling wheel used here is an Escil ESC300 GTL. A series of different grade diamond polishing discs was adhered to a glass plate on a spinning wheel by water surface tension. As the sample got thinner, polishing discs with smaller size of diamond particles were changed in order to decrease the surface roughness and make it as flat as possible; the spinning speeding of the wheel also was reduced. The sequence of diamond particles sizes on the disc and spinning speeding corresponding to the thickness of the specimen used in this procedure are shown in Table 3.1. The changes made here are important to avoid specimen breaking. Water was used to wash

the disc and clean the material removed from the specimen, otherwise these small powders or particles remained on the disc will affect the surface smoothness of the specimen.

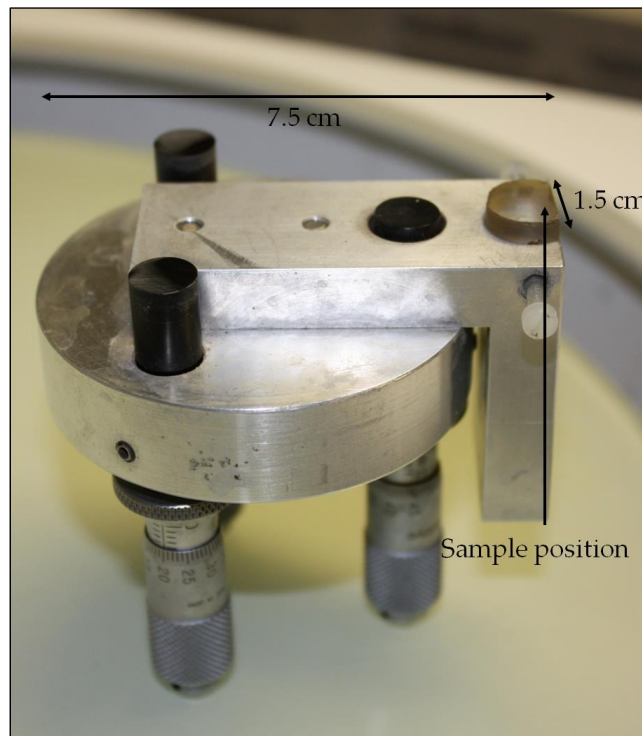


Figure 3.1: Tripod polishing jig and stub (reproduced from [49]).

Table 3.1: The sizes of diamonds on polishing disc for various sample thicknesses

Particle Size (μm)	Thickness(μm)	Wheel Speed (RPM)
15	<80	15
9	80-50	10
6	50-25	6
3	25-15	3
1	15-10	1

During the thinning process, the thickness of the specimen was measured by a Cooke, Troughton and Simms traveling microscope with a precision of $\pm 0.5 \mu\text{m}$. The specimens were polished to approximately 10-15 μm with the tripod. This is an appropriate thickness to start ion mill because of the slower rate of material removal by ion beam and the artifacts (such as surface roughness) which may arise during the prolonged ion milling. The Pyrex stub was put into acetone and the specimen released from the stub after 20 minutes. In order to be supported safely at high temperatures, the specimen was glued on a molybdenum grid by G-1

Epoxy glue from Gatan, which is capable of withstanding high temperature. The grids (bought from Agar Scientific) are 3.05 mm in diameter, with a 2×1 mm hole, as shown in Fig 3.2. The specimen was mounted across the 1mm gap carefully. Following that, the specimens were put into a 100 °C oven for 30 minutes to cure of the epoxy.

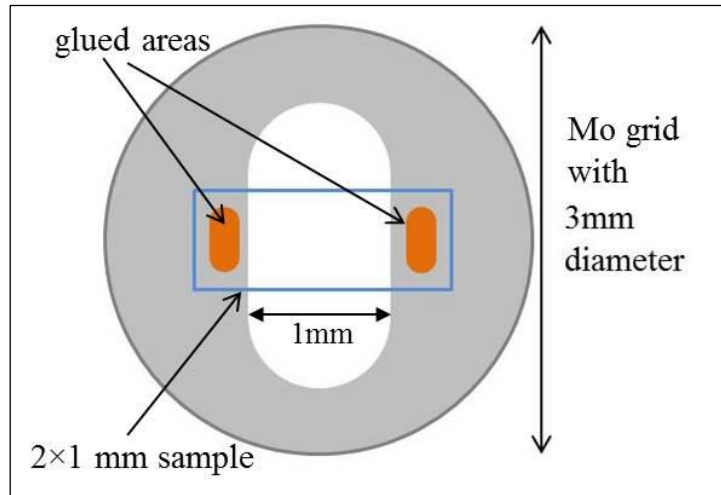


Fig 3.2: A schematic of a round molybdenum grid with a SiC sample and glued areas.

3.2.3 Ion beam milling

The machine used is called Gatan model 691 PIPS (short for Precision Ion Polishing System), which was developed by Gatan Inc. As shown in Fig 3.3, the specimen was mounted at the sample position in the middle of PIPS. There are two ion guns which emit an argon beam to polish the sample. The incident energy and angle are adjustable to different materials and sample preparation requirements. The sample was thinned to electron transparency by bombarding the surface of the specimen to sputter away atoms. For SiC, the starting incident energy and angle were 4 keV and 5 °, respectively. Then the energy and angle were changed to 2 keV and 3 ° when a perforation was detected by a built-in microscope above the sample and this procedure lasted for half an hour. Finally, an energy of 0.5 keV and an angle of 1 ° were used to smooth and clean the surface of sample. The sample rotates during the thinning. The final thickness of the sample normally reaches less than 100nm, which is 200 keV electron transparent [121]. The specimen was monitored by a built-in optic microscope above the sample during the thinning procedure.

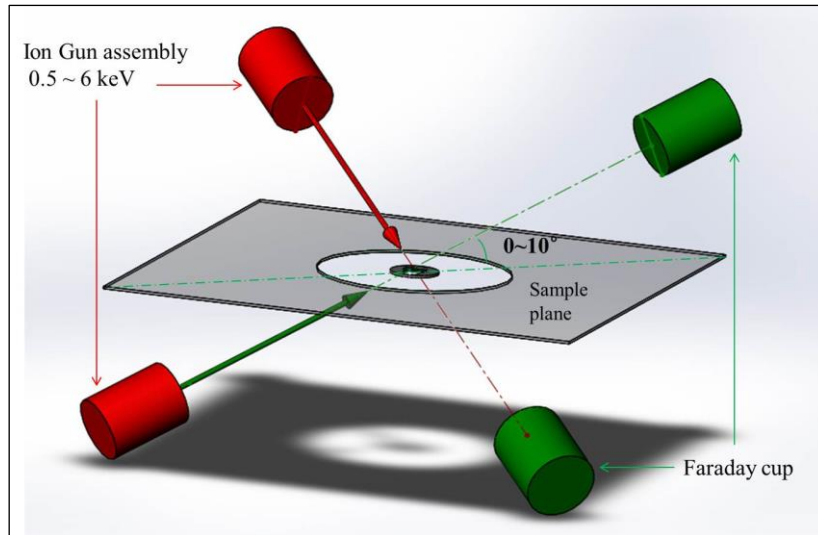


Figure 3.3: Geometry in Gatan PIPS showing ion guns, path of the ion beams, sample position and ion detection elements.

3.3 Transmission electron microscope

3.3.1 Electron scattering

As known wave-particles duality, the electron is treated in two different ways: a succession of particles in electron and wave in electron diffraction. Electron scattering can be classified in different ways: elastic and inelastic scattering, and also coherent and incoherent scattering. When an electron interacts with thin TEM samples, various terms produce, shown in Figure 3.4.

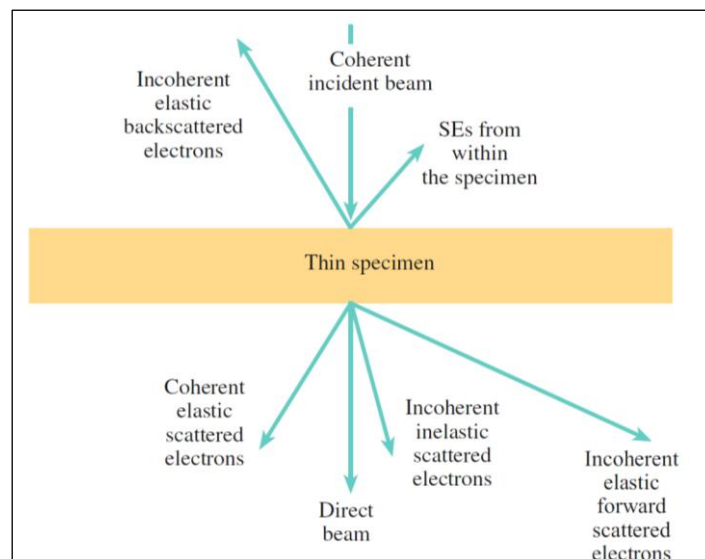


Fig 3.4: Different types of electron scattering from a thin specimen (reproduce from [72]).

When an electron encounters a single atom, the electron is scattered through an angle (θ) (radians) into some solid angle (Ω), measured in steradians (sr). The concept of scattering cross-section is induced to describe the chance of a particular electron undergoing scattering. The differential scattering cross section $d\sigma/d\Omega$ for a single, isolate atom can be written as:

$$\frac{d\sigma}{d\Omega} = \frac{1}{2\pi \sin \theta} \frac{d\sigma}{d\theta} , \quad (3.1)$$

and the cross sections of scattering $d\sigma/d\Omega$, whose scattering angles are bigger than θ , are integrated from θ to π , written as follow:

$$\sigma_{atom} = \int_{\theta}^{\pi} d\sigma = 2\pi \int_{\theta}^{\pi} \frac{d\sigma}{d\Omega} \sin \theta \, d\theta . \quad (3.2)$$

3.3.1.1 Elastic scattering

Elastic scattering lays the foundation of contrast in the imaging mode and diffraction pattern of TEM. In consideration of wave property of the electron beam, the atomic-scattering factor $f(\theta)$ is defined by the equation as below:

$$|f(\theta)|^2 = \frac{d\sigma(\theta)}{d\Omega} . \quad (3.3)$$

In the equation, $f(\theta)$ is a parameter of the amplitude of an electron wave, which is scattered from an isolated atom and $|f(\theta)|^2$ is in direct proportion to the scattered intensity.

Then we consider the situation in a crystal structure. In a structure unit, $f(\theta)$ of all the atoms is multiplied by its phase factor and then is summed up, of which the sum $F(\theta)$ is written:

$$F(\theta) = \sum_i^{\infty} f_i e^{2\pi i(hx_i + ky_i + lz_e)} . \quad (3.4)$$

The absolute value $|F(\theta)|^2$ is in direct proportion to the scattered intensity. The phase factor considers the phase difference of between scattered waves by atoms on different parallel planes. The scattering angle θ is between the incident and scattered electron beams.

Von Laue used a light-optics way to compute the path difference for a wave. The path differences are integer numbers of wavelengths in three dimensions, $h\lambda$, $k\lambda$ and $l\lambda$. The well-known Von Laue's diffraction equations are given as below:

$$a(\cos \theta_1 - \cos \theta_2) = h\lambda \quad , \quad (3.5)$$

$$b(\cos \theta_3 - \cos \theta_4) = k\lambda \quad , \quad (3.6)$$

$$c(\cos \theta_5 - \cos \theta_6) = l\lambda \quad , \quad (3.7)$$

and the two-dimensional schematic is shown in Fig 3.5:

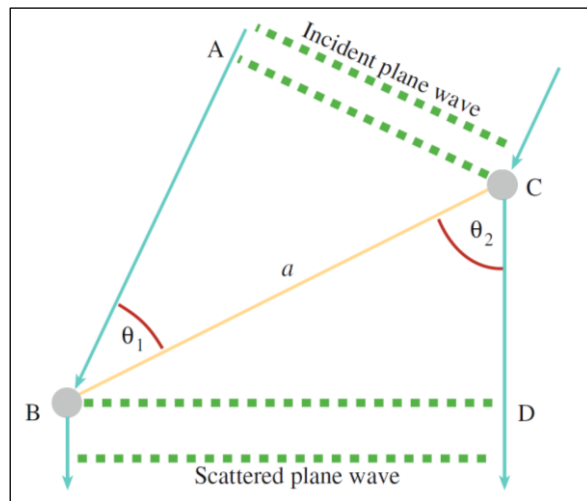


Fig 3.5: Two-dimensional schematic of von Laue approach (reproduce from [72])

Then later, Sir William H. and Mr. W. Lawrence Bragg simplified Von Laue's approach. They regarded the electron waves as behaving as if they are reflected off atomic planes as revealed in Fig 3.6. Bragg's law can be written as equation (3.8):

$$n\lambda = 2d \sin \theta_B \quad (3.8)$$

In the equation, d is the difference between two planes and θ_B is the Bragg angle.

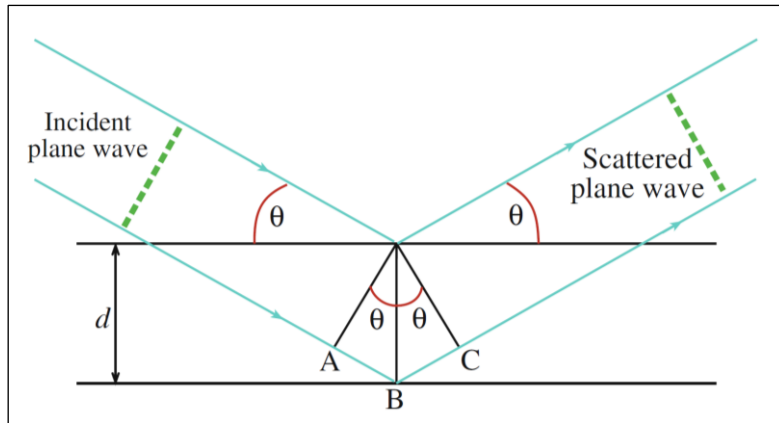


Fig 3.6: Schematic of the Bragg diffraction (reproduce from [72])

3.3.1.2 Inelastic scattering

Inelastic scattering, which based on inelastic collision, may not conserve kinetic energy. On one hand, the inelastic scattering will generate lots of useful signals and we can form spectrum images to analysis the chemistry and electronic structure of the specimen. For instance, Energy dispersive spectrometry is used to analyse emitted X-rays and Electron energy loss spectrometry analyses the energy loss of electron caused by the inelastic scattering. On the other hand, the energy transfer will result in more electron beam damage and heating, compared to elastic interaction.

3.3.2 Components and structure

3.3.2.1 Electron source

There are two kinds of electron source: thermionic and field-emission sources. The filaments of thermionic sources are made of tungsten or lanthanum hexaboride (LaB_6) crystals and field emitters use fine tungsten needles. The electron source used here is a tungsten filament. Fig 3.7 shows a schematic of the thermionic electron source. A voltage is applied between the filament and anode and then focused by a Wehnelt. The electrons come through a crossover and emit with a divergence angle, α_o .

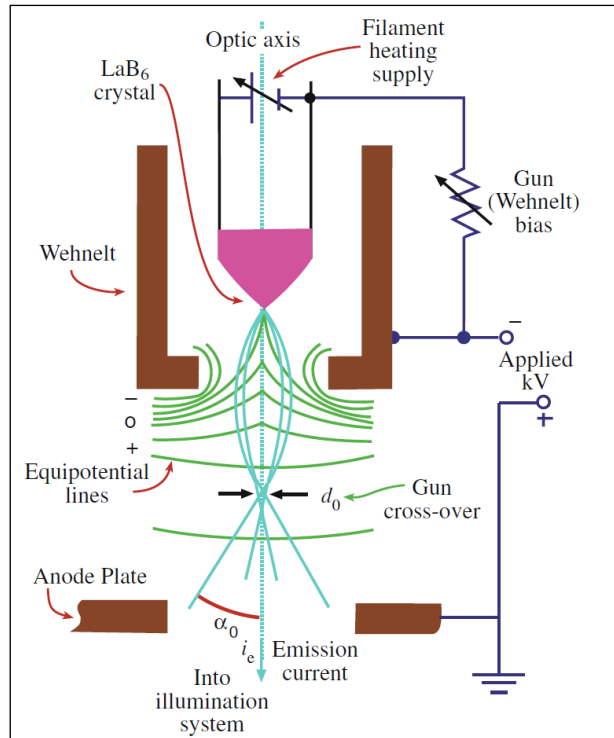


Fig 3.7: Schematic of the thermionic electron source (LaB_6) (reproduce from [72])

3.3.2.2 Lenses

Four electromagnetic lens sets are used in the TEM: the condenser lens, the objective lens, the intermediate lens systems and the projective lens. A modern magnetic electron lens contains soft iron polepieces (upper and lower) with a hole in the middle and a coil of copper wire surrounding each polepiece, seen in Fig 3.8. The gap between two polepieces is an important parameter of an electromagnetic lens. The magnetic field strengthens from the centre of the hole to the edge of the hole.

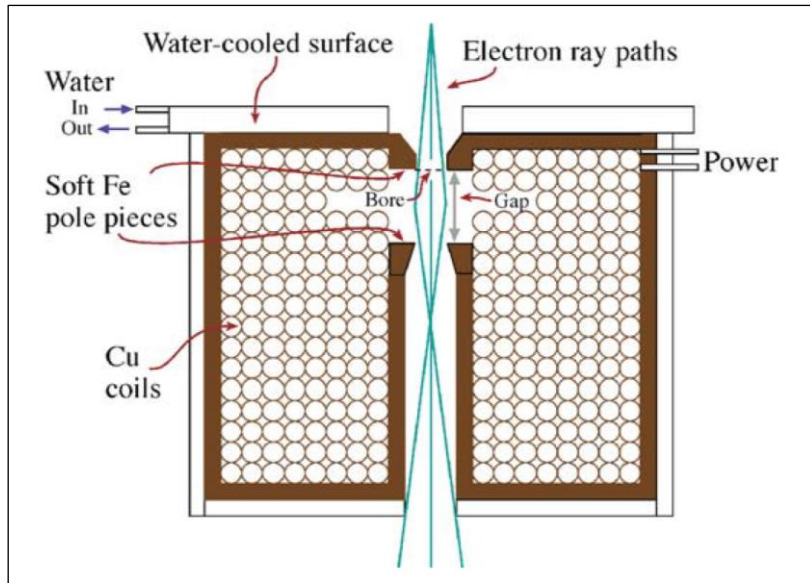


Fig 3.8: Schematic of a magnetic lens (reproduce from [72])

3.3.2.3 Apertures

Apertures are a set of holes with different diameters positioned on the diaphragms. The diameters of the apertures range from a few to μm to several hundred μm . The apertures limit the collection angle of the lens. The objective aperture lens effects a series of the most important parameters of a TEM: the resolution of images, the depth of the field and the depth of focus, the image contrast, the collection angle of the electron energy-loss spectrometer and so on.

3.3.2.4 Image capture

For JEM-2000FX, a fluorescent viewing screen is mounted following the projector lens. It is coated by ZnS grains with sizes of $\sim 50 \mu\text{m}$. The human eye has its peak sensitivity at the 555nm green light emitted by electron excitation in ZnS. The viewing screen is particularly important when finding and centring the electron beam. In modern TEMs, Charge-Coupled Device (CCD) detectors are used as a powerful tool to take images. A computer is used to display, analyse, store and share the data making it much convenient and flexible. Meanwhile, CCD, which possesses the advantages, such as low noise characteristics and rapid image capture, significantly outweighs other semiconductor detectors and scintillator-photomultiplier detectors.

3.3.3 Main operating modes and techniques

TEM is an outstanding tool for materials research. The mechanism and setting of two main modes (diffraction mode and imaging mode) are shown in Fig 3.9. Both will be explained below in this section.

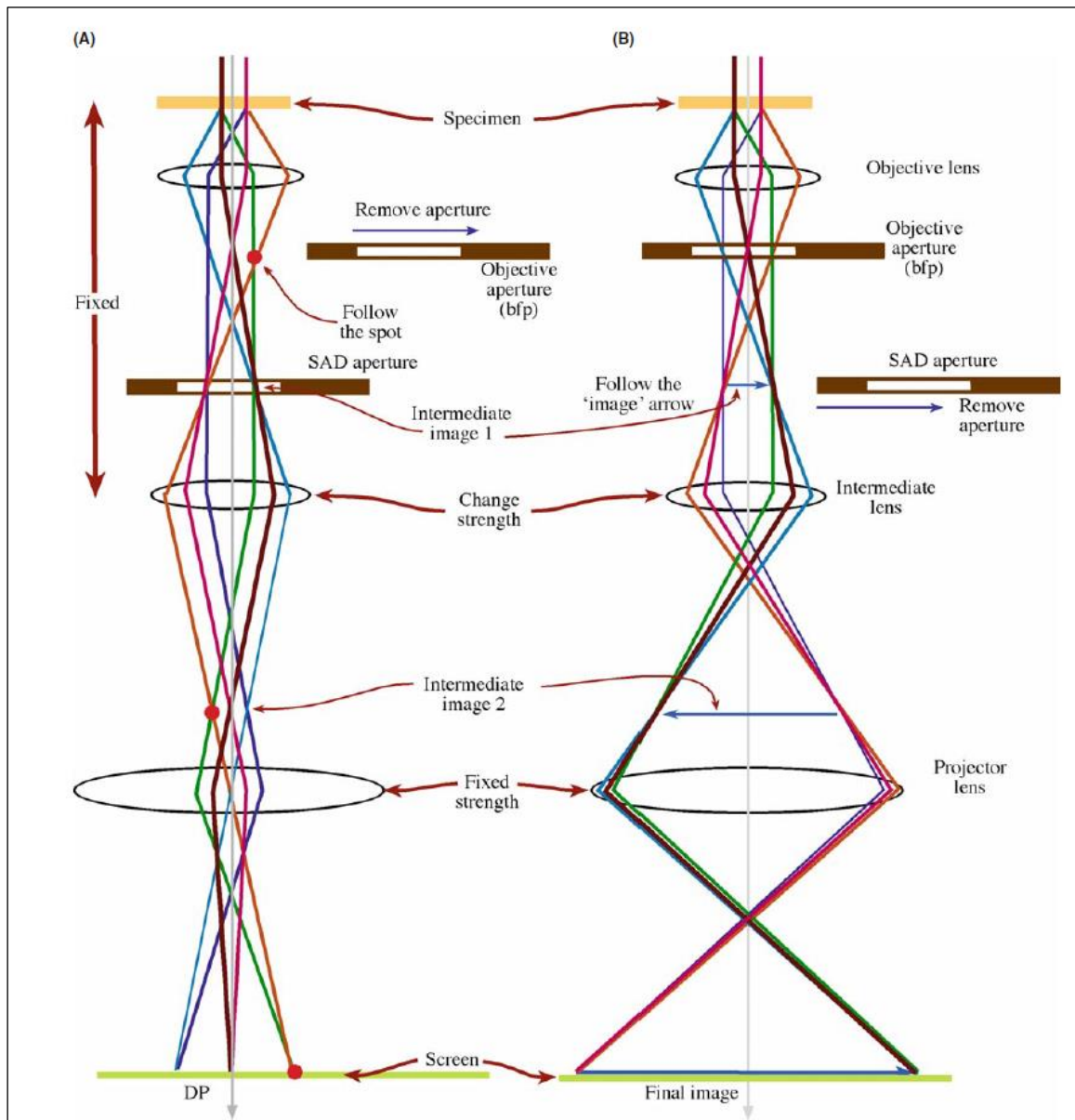


Fig 3.9: The two basic modes of TEM operation. In the diffraction pattern mode (DP), the objective aperture is moved away and selected area aperture is inserted into the image plane of the objective lens to choose a specific area of sample. In the imaging mode objective aperture is inserted into the back focus plane to choose a required area of the specimen while the selected area aperture is moved out. (reproduced from [72])

3.3.3.1 Diffraction

Diffraction Patterns form in the back-focal plane of the objective lens. By changing the focus of the intermediate lens to the back-focal plane of the objective lens, the diffraction pattern is amplified and then displayed on the viewing screen or CCD. Diffraction intensity varies with the changes of intensity of different diffracted electron beams. Diffraction Patterns give the crystallographic information of the samples. The information of a particular area is collected via Selected Area diffraction (SAD).

3.3.3.2 Imaging

Imaging mode is another important operating mode of TEM. The images form on the imaging plane of the objective lens and are magnified by the intermediate lenses. Imaging can be performed in two main modes: bright field imaging and dark field imaging. In the bright field mode, an aperture is positioned in the back focal plane of the objective lens and this allows the direct electron beam to go through. Therefore, the image is contributed by the mass-thickness and diffraction contrast. In the dark field mode, one or several diffracted beams are chosen by the objective aperture whilst the centre direct beam is obstructed. Some important information from the sample can be well presented in dark field images, such as dislocations, planar defects or sizes of precipitated particles.

3.3.3.3 Down-zone imaging

Down-zone imaging means observing the sample under the condition where one crystallographic direction is aligned parallel to the direct electron beam. This can be achieved by tilting a crystallographic sample such that diffraction spots of the low index are distributed on the screen with uniform intensity in diffraction mode. The sample satisfies the Bragg conditions strictly and gives distinct contrast in the images in imaging mode. Images taken slightly off-zone are essential in observing and analysing the orientation of bubble discs (or platelets) in this work because down-zone images are completely dominated by Bragg contrast and the some features may not be clear in the images.

3.3.3.4 Contrast mechanisms

Contrast is generated when the electrons interact with the sample. A TEM image contains different types of contrast. This section discusses the main types of contrast involved in this work.

3.3.3.4.1 Mass-thickness contrast

Mass-thickness contrast appears because of incoherent elastic scattering of electrons and inelastic scattering. It closely related to the atomic number Z , the density, ρ and the thickness, t . The thicker or higher atomic density areas of the samples, the darker you will get on the image. Fig 3.10 shows the mechanism of mass-thickness contrast. Mass-thickness contrast is the main mechanism of non-crystalline materials, such as biological TEM specimens.

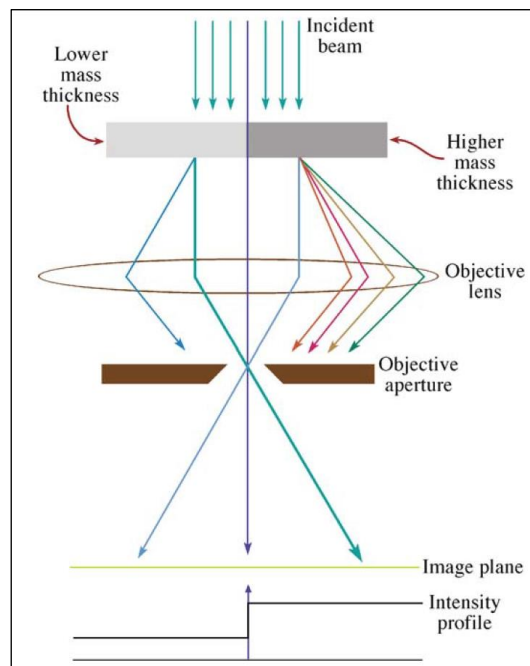


Fig 3.10: The mechanism of mass-thickness contrast in a BF image. In thicker and higher atomic density area, more electron are scattered off the incident axis. Then the area goes darker. In the thinner and low atomic density area, less electron are scattered off the incident axis. The area is lighter. (reproduced from [72])

3.3.3.4.2 Fresnel contrast

Fresnel contrast is a form of phase contrast which is produced by the potential difference between the voids (or cavities), vacuum and edges of samples. Fresnel contrast from voids (or cavities) in the images gives a bright fringe in underfocus of the objective lens and a dark fringe in overfocus condition. Thus bubbles, platelets, and bubble discs can be observed, even without surrounded strain field. The observation of bubbles, platelets, and bubble discs with strain-fields is discussed as below in section 3.3.3.4.3 For the JEOL JEM-2000FX Microscopic bubbles as small as 0.5nm in diameter can be detected with Fresnel contrast. Fresnel contrast is probably hidden by strain contrast in the sample in some conditions.

3.3.3.4.3 Strain-fields

Due to the existence of intrinsic and ion-irradiation induced defects, stain fields are generated around these defects. This results in the bending of some the lattice planes in the samples. The bending planes fit the Bragg condition. Thus, the diffraction conditions change and then contrast in the real-time images change relatively. Strain-fields induced contrast is useful for detecting and characterising the defects in the samples, for instance, dislocations and cavities.

3.4 MIAMI

MIAMI, which is short for Microscope and Ion Accelerator for Materials Investigations, is an in-situ ion irradiation facility. All of the irradiations were conducted on MIAMI. The system induces an accelerated ion beam into JEOL JEM-2000FX TEM. It can generate ion species from H to Xe at an energy range 0~100 keV. Low energy implantation will allow light ions to stop in the target, while high energy heavy ion or self-ion irradiation could produce numerous atomic displacements. Many kinds of samples holders are available for different uses, including double-tilt with heating (RT to 1000 °C), cooling (-173 °C to 100 °C), staining and 360° rotational. This makes the facility flexible to suit various research conditions. Furthermore, in-situ TEM observation allows the facility to explore the dynamic evolution of materials and irradiated ion induced changes and underlying mechanisms. The angle between induced ion beam and the electron beam is 30°. The schematic of beamline from ion source to sample position of the MIAMI facility is shown in Fig 3.11 [122].

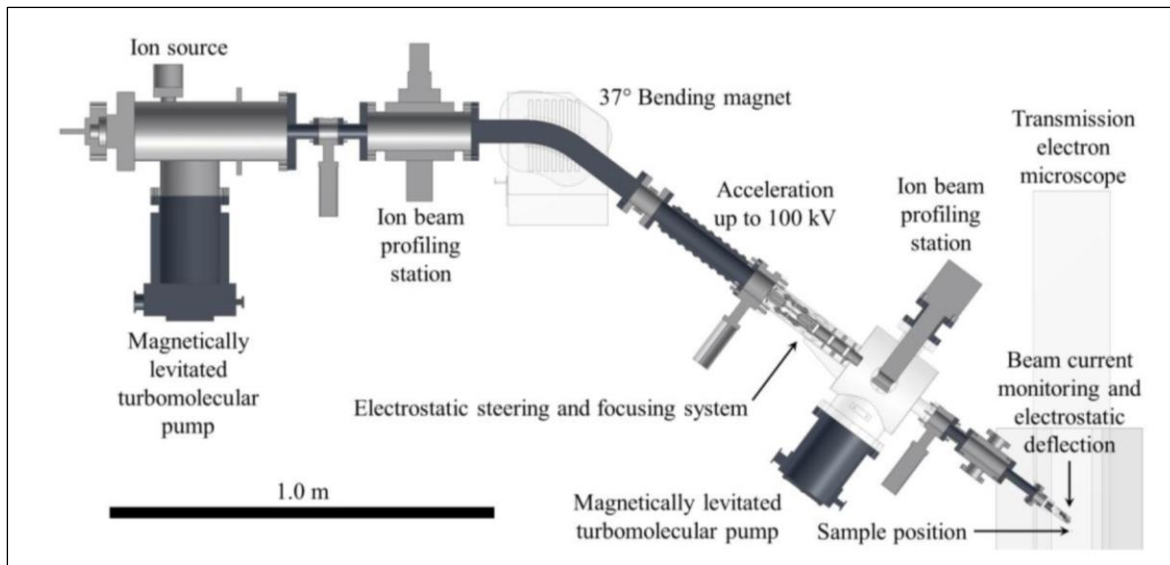


Fig 3.11: Schematic of the ion beamline of MIAMI from the ion source to the final deflection (reproduced from [122])

3.4.1 Ion source

A Colutron ion source generates an ion beam by ionising a gas from a gas cylinder or heated solid. The ionisation happens in a quartz chamber where a tungsten filament is heated by applying 12~15 V to cause thermionic electron emission. The electrons are attracted to the anode (usually 50V~125V with respect to filament) and then the electrons pass through and ionise the gas creating a plasma. An accelerating voltage is applied up to 10 kV between the anode and the extraction element of the Colutron mode. Higher energy ions can be achieved by the acceleration tube mounted after the bending magnet. The ion source needs to be cooled by a cooling loop. An exploded view of ion source is illustrated in Fig 3.12 [123].

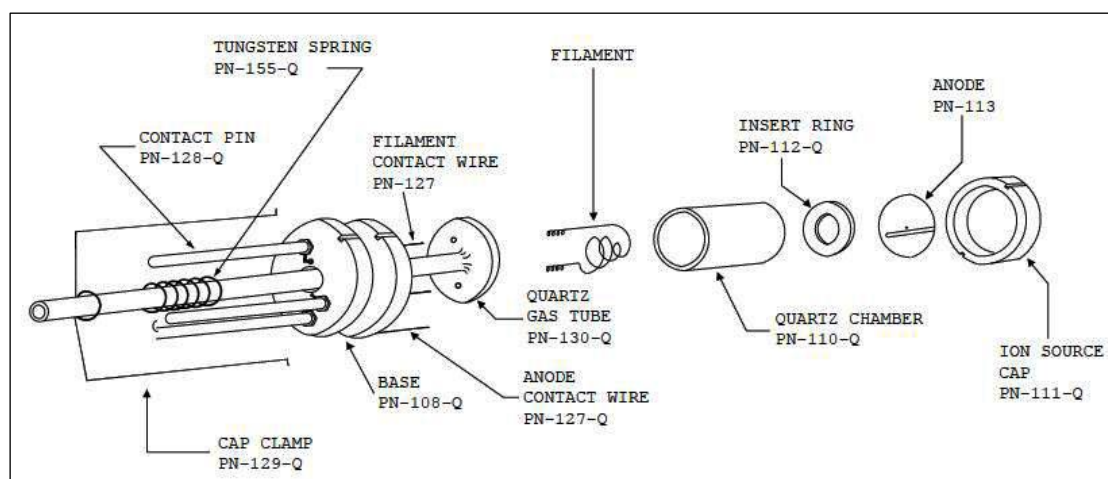


Fig 3.12: An exploded view of Model 101-Q ion source. (reproduced from [123])

3.4.2 Beam profile monitors

Two beam profile monitors provided by National Electrostatics Corporation are positioned on the beamline (see Fig 3.4). Each monitor consists of a helical wire which rotates at 1080 RPM. The helical wire sweeps through the ion beam twice in a single period in two orthogonal directions as the wire rotates. Then, secondary electrons are produced when ions hit the wire and are collected by the surrounding cylinder to measure intensity across the beam, which is displayed as a profile on an oscilloscope.

3.4.3 Beam focus and deflection

3.4.3.1 Einzel lens

There are two Einzel lenses in MIAMI for the purpose of focusing the ion beam. The first one is mounted following the first acceleration of the ion beam in the Colutron G-2 and the second one is installed following the double deflection in the beamline before the TEM.

3.4.3.2 Bending magnet

The bending magnet acts as both ion beam deflection and energy/species selection. The magnetic field is generated in a direction perpendicular to the ion's trajectory. The ions are deflected by the Lorentz force in the magnetic field. The equation for the magnetic field strength is given as follow:

$$B = \frac{mv}{qr} \quad (3.9)$$

Where m , v , q and r mean the mass of the ions, the velocity, the electron charge and the radius of the curved path of the ions, respectively. The velocity, v , is derived from the voltage (V_{acc-1}) acceleration of the ions in the Colutron G-2, shown in equation 3.10 and 3.11. The magnet field strength, B , is adjustable by changing the current passing through the coils of the electromagnet.

$$V_{acc-1} = \frac{mv^2}{2q} \quad (3.10)$$

$$\text{Then, } v = \sqrt{\frac{2V_{acc}-1q}{m}} \quad (3.11)$$

3.4.3.3 Double deflection

Two pairs of parallel plates are set between the acceleration tube and the second Einzel lenses. Each pair of plates applies voltages up to 10 kV. Thus, two normal mounted pairs of plates provide electric field to correct the direction of ion beam. The applied voltage is actual -5 kV to +5 kV. Calculations of the electric force and electric field are given by the equation 3.12 and 3.13.

$$F = qE_d \quad (3.12)$$

$$E_d = \frac{V_{plates}}{d} \quad (3.13)$$

Where F , E_d , d and V_{plates} mean the electric field force, the electric field between the plates, the distance between the plates and the applied voltages between the plates, respectively. One pair of parallel plates is installed horizontally and the other pair is installed vertically, which allows the double deflection to deflect the beam in both directions. A schematic of double deflection is shown in Fig 3.13.

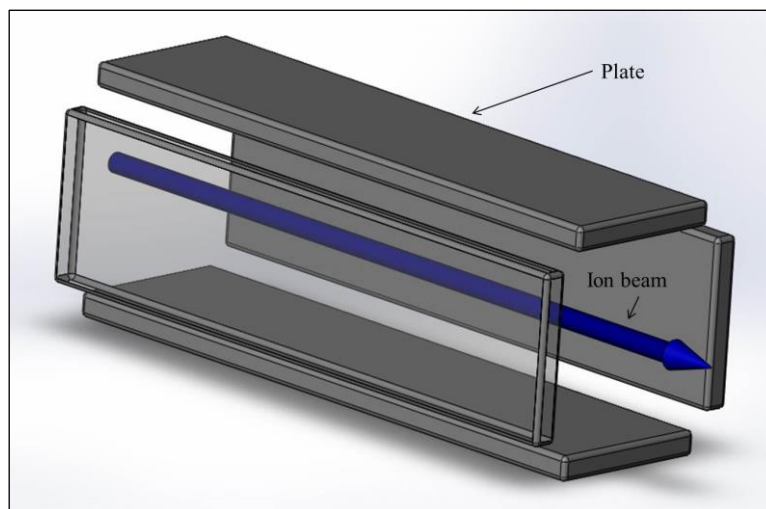


Fig 3.13: Schematic of double deflection

3.4.4 Current metering system

3.4.4.1 Skimmer

The skimmer is used to measure the current and help to align ion beams. It consists of three diaphragms and a 15 mm long stainless steel tube. A tube with a small inner diameter of 3–4 mm is positioned between the first two diaphragms (see Fig 3.14). The well aligned ion beam is collected by the second diaphragm in the middle with an aperture of 1mm. the current of the skimmed ion beam is displayed on a picoammeter, which is connected to the diaphragm. By coming through the first aperture, the ion beam direction is selected. It makes sure that the ion beam travels close to the zero potential line, when it enters the final deflection plates. The skimmer is able to give constant monitoring, whereas the Current Metering Rod (CMR) is taken out during the experiment.

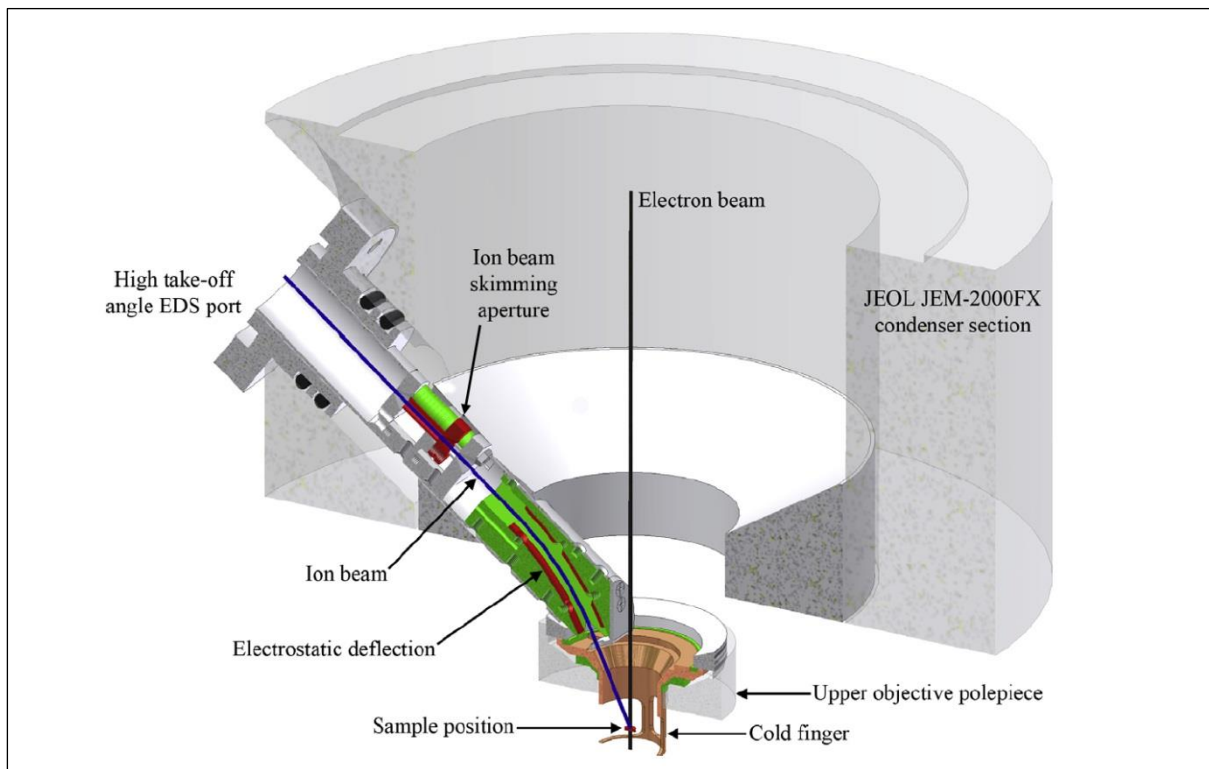


Fig 3.14: Sample position geometry in the MIAMI facility. Ion beam path, final deflection plates and electron beams are shown. The electron beam, ion beam and sample position all intersect towards the bottom of the image. The skimmer is placed before the final deflection. It helps to find the ion beam during the alignment of ion beam and to monitor the ion beam during the irradiation experiment. [80].

3.4.4.2 Current metering rod

The current metering rod fits in TEM like a sample rod. It consists of a holey carbon film covered hole and an ion beam detection plate with secondary electron suppression. The carbon film is used to adjust the height of the rod by finding the exact focus plane of the carbon film. The electron beam is then centred in the detection plate prior to the alignment of ion beam. There are two diaphragms with apertures above the detection plate. The first one is the entrance of ion/electron beam. A voltage of -60 V is applied on the second diaphragm to suppress the secondary electrons. The detection plate gives the accurate current metering at the sample position. As an intrinsic shortcoming, the CMR is not able to measure the dosimetry once the sample holder is installed in the TEM.

3.4.5 Final deflection

The ion beam is deflected again by two pairs of bent parallel plates of final deflection before it hits the sample. An angle of 30° between the electron beam and ion beam is achieved from the final deflection. The voltages applied on the upper plate and the bottom plate are equal and opposite, which keep the centre line of the final deflection assembly as a zero potential zone. The zero potential axes is the centre line of two pairs of bent parallel plates where the ions experience minimum focusing effects due to the applied voltages on the plates. The electric field formed by the applied voltage bends the ion beam and force it to travel along the zero potential zone. The applied voltage on vertical direction is decided by the energy of the ions, shown in equation 3.14, 3.15, 3.16.

$$E = qV_{acc} = \frac{1}{2}mv^2 \quad (3.14)$$

$$F = Eq = \frac{mv^2}{r} = \frac{2qV_{acc}}{r} \quad (3.15)$$

$$V_{plates} = Ed = \frac{2V_{acc}d}{r} \quad (3.16)$$

In the equation, E , V_{acc} , d and r represent the energy of the ion, total acceleration voltage of the ion, the distance between two plates and radius of the curved path of the ions, respectively. The geometry and structure around the sample position inside the microscope is illustrated in Fig 5.3.

3.4.6 Transmission electron microscope

JEOL JEM-2000FX TEM is used to take images and analyse the evolution of materials during the irradiation. Diffraction pattern mode and imaging mode were both used in this work. This allowed images to be captured along with information on the crystallographic orientation. The acceleration voltage used for electron in this experiment was 200 keV. Bright field imaging mode and diffraction mode were used. Samples were installed in the double-tilting heating holder which is able to be heated to 1000 °C.

4. In-situ Analysis of Helium Irradiation

Effect on SiC at High Temperatures

4.1 Introduction

Neutron induced transmutation reactions can release alpha particles which acquire electrons to become helium atoms. Table 4.1 shows the main transmutation reactions in SiC in nuclear reactors [124].

Table 4.1: The most common transmutation reactions in SiC [124].

Product	Transmutation
He	As a by-product of fission reactions
Be	$^{12}\text{C}, (n,\alpha) \rightarrow ^9\text{Be}$
Mg	$^{28}\text{Si}(n,\alpha) \rightarrow ^{25}\text{Mg}, ^{28}\text{Si}(n,\alpha) \rightarrow ^{26}\text{Mg}$
Al	$^{28}\text{Si}(n,2n) \rightarrow ^{27}\text{Si} \rightarrow ^{27}\text{Al}$
P	$^{31}\text{Si}(n,\gamma) \rightarrow ^{31}\text{Si} \rightarrow ^{31}\text{P} + \beta$

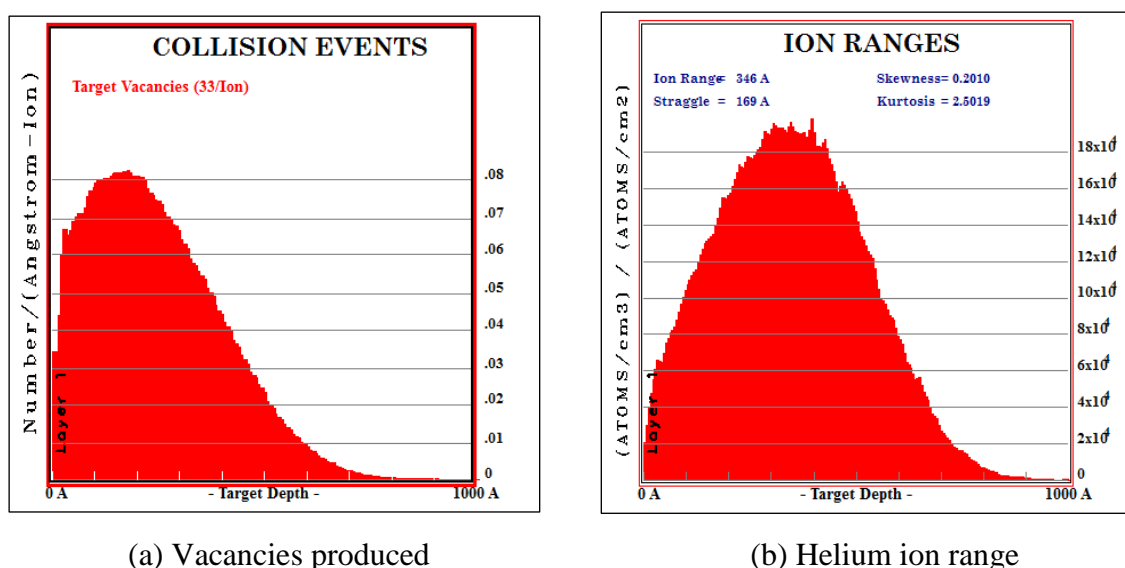
In our experiments, 4H-SiC TEM samples were irradiated by 3.5 keV helium at either 700 °C, 800 °C or 900 °C. The Gen-IV nuclear reactors and future fusion reactors will operate at these temperatures or even above. The MIAMI in-situ irradiations produced useful results applicable to the nuclear applications of SiC-based materials. Under these conditions, helium bubbles nucleated, grew. Bubbles discs were observed in the samples. The evolution observed by TEM helps to understand the mechanisms on the behaviour of SiC under helium irradiation.

4.2 Irradiation conditions

After preparation, the SiC samples were mounted into a Gatan double-tilting heating holder. The samples were irradiated with 3.5 keV helium at either 700 °C, 800 °C or 900 °C. The flux of the helium is 2.5×10^{13} ions.cm⁻².s⁻¹ and the maximum fluence reached more than 6.1×10^{16} ions.cm⁻².

4.2.1 Computer calculation with SRIM

SRIM (software version 2013.00) [125] was run before the experiment to calculate the ion and damage distribution. The choice of helium energy for the irradiation experiments was based on the results of the ion and damage distribution derived from SRIM. The samples were assumed to have a thickness of 100 nm and the displacement energies for Si and C are the default values provided by SRIM. When SRIM was run, helium beams with different energies between 1~6 keV were used and the incident angle of 30° off the normal of the sample surface stay consistent with the incident angle in MIAMI. Then judging from the results of SRIM, it is learnt that energy of 3.5 keV was an appropriate value for helium irradiation in this work. The ion distribution peak of the ion range is about 346 Å. The damage and ion distribution of 3.5 keV helium implantation were shown in Fig 4.1. The conclusion was drawn that all the helium atoms came to rest in a thickness of 100 nm and most of collision happened within this thickness.



(a) Vacancies produced

(b) Helium ion range

Fig 4.1: Graphs output from SRIM [125] showing the predicted irradiation damage (a) and helium ion ranges (b) in SiC.

4.3 Experimental results

4.3.1 Helium bubbles

In the experiments, bubbles were generated under helium irradiation. Isolated bubbles were observed at 700 °C, 800 °C and 900 °C. At 700 °C, areas which contained a high density of isolated bubbles were observed. A typical area with bubbles at 700 °C is shown in Fig 4.2. As discussed in section 3.3.3.4.2, the Fresnel contrast predominated in these images, which were tilted slightly off down. The bubbles featured bright fringes in under-focus condition (see Fig 4.2(a)), while in over-focus condition they exhibited dark fringes (see Fig 4.2(b)). The observation and mechanism of bubbles growth at 700 °C were consistent with those in the thesis of Pawley [49]. In his thesis, he has already detailed the bubble evolution at 700 °C. When the experiment temperatures was repeated at the temperatures of 800 °C and 900 °C, the bubbles formed were bigger than the sizes at 700 °C at the same fluence. It may be explained that higher temperature increases the number of vacancies and helium atoms which have higher energies to overcome the energy barriers. More helium atoms and more vacancies are able to migrate further and less likely to trap. There are more helium atoms and vacancies available nearby when a bubble start to form. More experiments on the sizes of bubbles at different temperatures are proposed for further works.

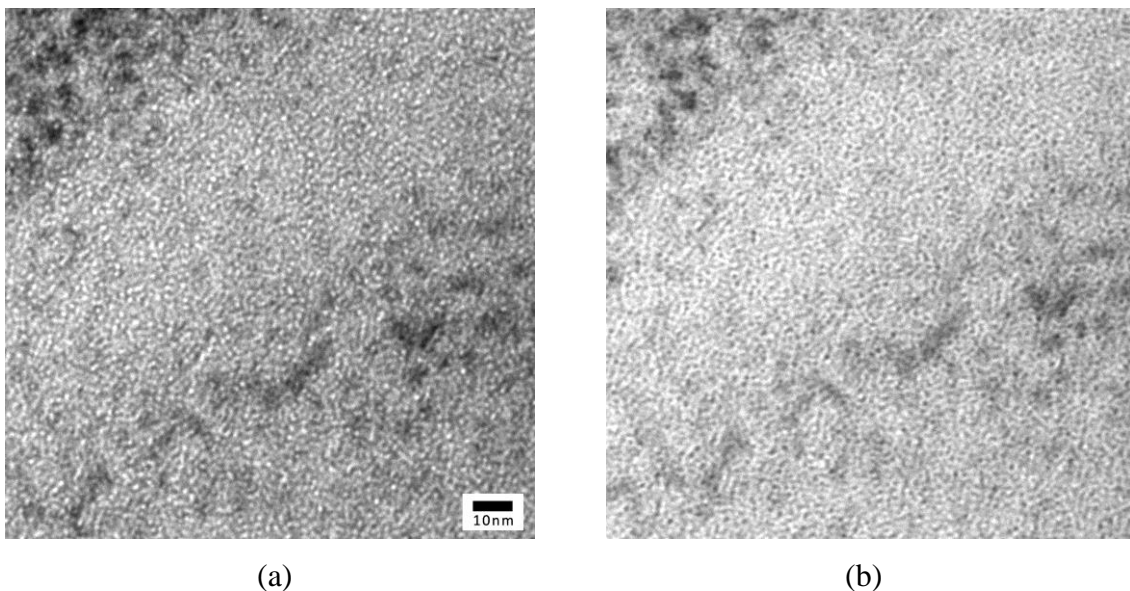


Fig 4.2: TEM images of bubbles at fluence of 6.1×10^{16} ions.cm⁻² at 700 °C; (a) underfocus (-60 nm), (b) overfocus (+60 nm). Scale bar applies to both images.

4.3.2 Bubble discs

Bubble discs were formed in our helium irradiation experiments of 4H-SiC. Fig 4.3 illustrates isolated bubbles and edge-on bubble discs in underfocus and overfocus conditions, which were from an irradiation experiment at a fluence of 6.1×10^{16} ions.cm⁻² at 800 °C. The evolution and characteristics of bubble discs are detailed in this section.

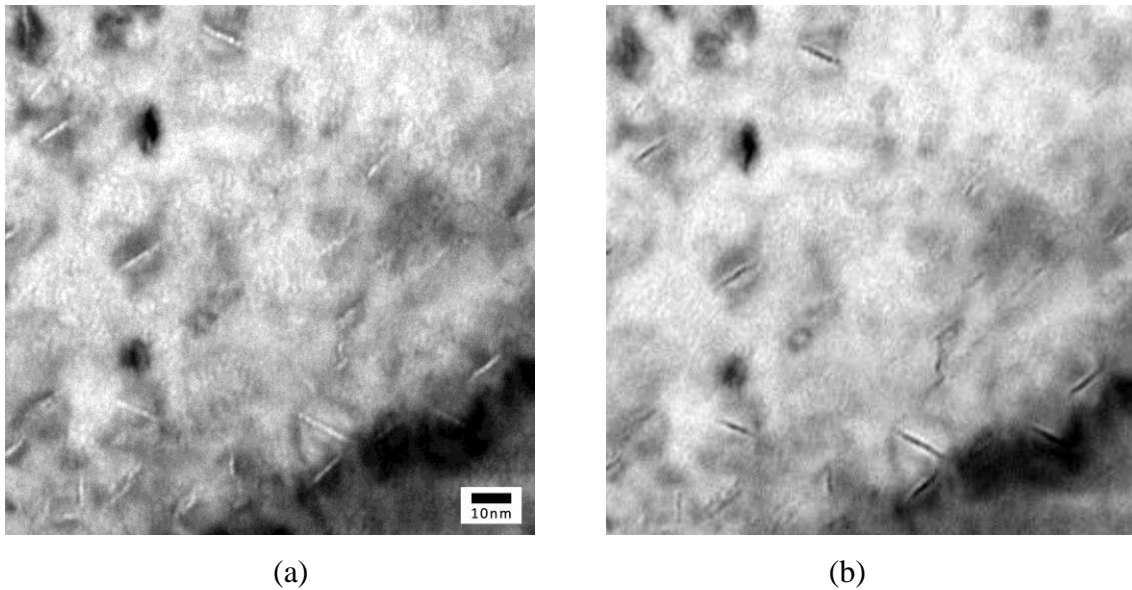


Fig 4.3: TEM images of bubbles and edge-on bubble discs at 6.1×10^{16} ions.cm⁻² at 800 °C viewed close to [001] zone-axis. (a) underfocus (-60 nm), (b) overfocus (+60 nm). Scale bar applies to both images.

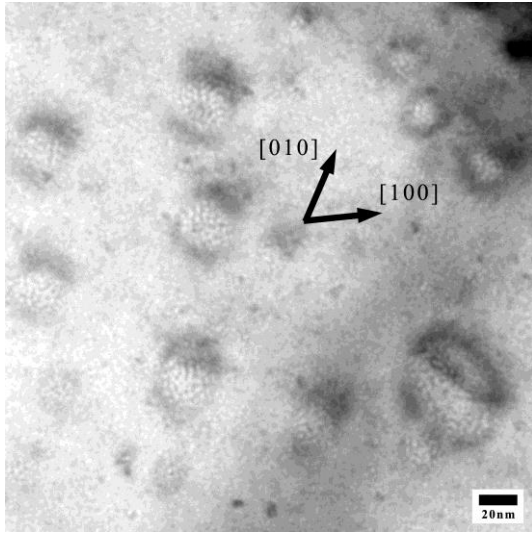
4.3.2.1 Plan-view and edge-on bubble discs

When the samples irradiated at 900 °C with a fluence of 6.1×10^{16} ions.cm⁻² were observed in [001] direction, both plan-view and edge-on bubble discs were formed, shown in Fig 4.4. However, edge-on discs were more easily detected when viewed in various directions due to their significantly stronger contrast.

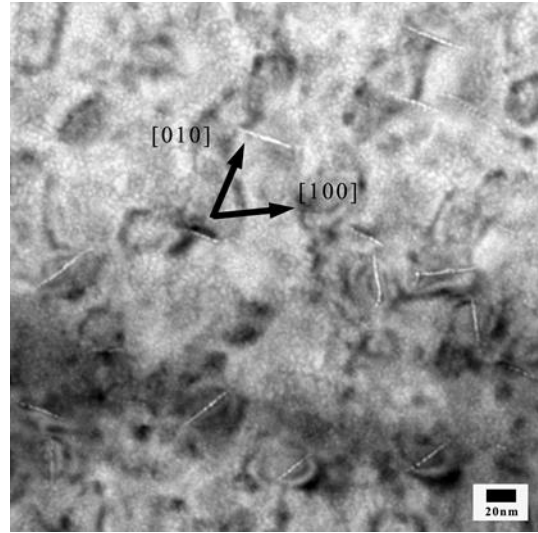
Plan-view bubble discs were easily observed in thin areas where they were not obfuscated by contrast from other features, such as isolated bubbles, different orientated bubble discs and the surrounding strain fields of the bubble and discs.

It is obvious that the plan-view bubble discs lay on {001} planes when observing close to the [001] zone-axis. A quantity of published papers have reported the plan-viewed platelets and discs (lying on {001} planes) [81], [106]–[110], while it was the first time ever that on-edge bubble discs were detected viewed in [001] direction.

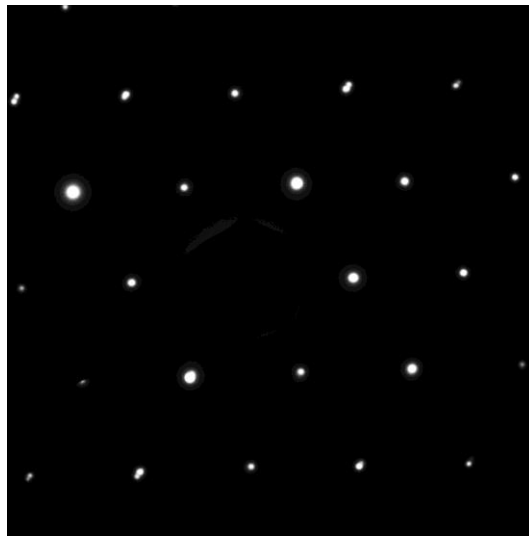
As a new interesting finding and due to the ease of observation, the experiments mainly focused on the edge-on discs. More details of the analysis on the lying-on planes of on-edge bubble discs will be presented in section 5.6.



(a)



(b)

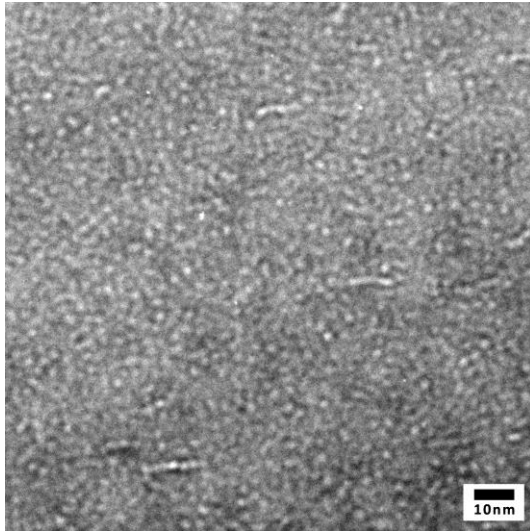


(c)

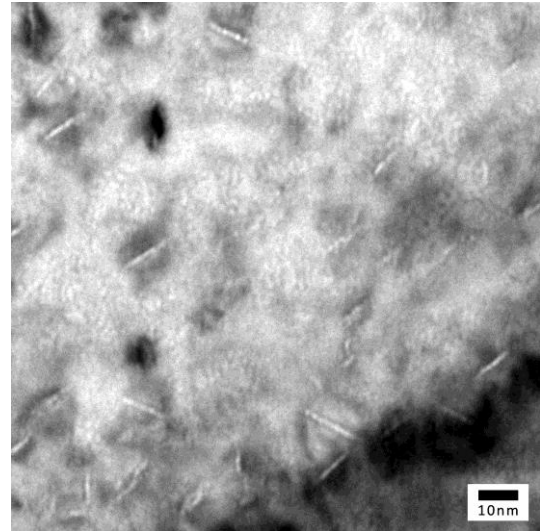
Fig 4.4: Plan-view (a) and edge-on (b) bubble discs at a fluence of 6.1×10^{16} ions.cm⁻² at 900 °C; (c) the corresponding diffraction pattern.

4.3.2.2 Effects of temperature on bubble disc formation

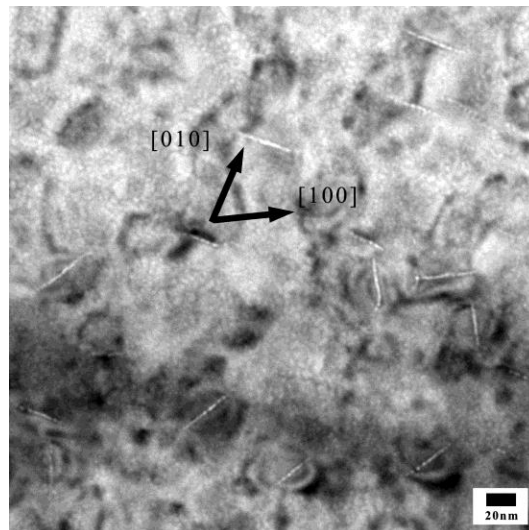
Bubble discs can be formed at 700 °C, 800 °C and 900 °C under the helium irradiation, shown in Fig 4.5. Very few bubble discs are observed at 700 °C at a fluence of 6.1×10^{16} ions.cm⁻², shown in Fig 4.5(a). However, none was detected at the same temperature and fluence in Pawley's work [49]. Pawley's research was more interested in thin areas of the samples. He did the statistics of bubble density at the edge of the hole which is generated by PIPS. In the present work, a very low density of edge-on bubble discs were detected at relatively thick areas (~50nm) at 700 °C. 4H-SiC samples behaved differently when the specimens were heated to 800 °C and 900 °C. A high areal density of bubble discs were detected in the irradiated areas, shown in Fig 4.5(b) and (c). In Zhang's ex-situ experiment, planar clusters of helium bubbles in low density were observed after annealed above 700 °C [108]. Therefore, it is expected there is a temperature threshold (defined as T_t) around 700 °C which changes samples evolution under these conditions. Based on the images captured during the experiment, the mean final sizes of bubble discs at 900 °C at 6.1×10^{16} ions.cm⁻² were larger than those at 800 °C at 6.1×10^{16} ions.cm⁻². However, appropriate post-irradiation analysis to confirm the statistical significance of this observation was not possible due to mechanical failure of the sample at 800 °C. The general trend observed was that larger bubble discs formed at higher irradiation temperatures.



(a)



(b)



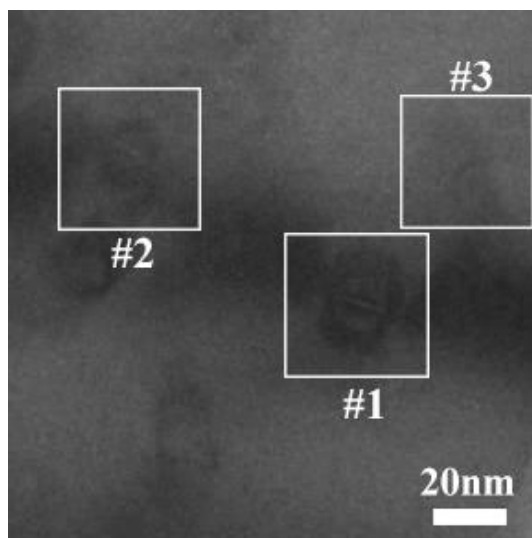
(c)

Fig 4.5: The sizes of the edge-on bubble discs at different temperatures at the same fluence of $\sim 6.1 \times 10^{16}$ ions.cm⁻² viewed close to [001] direction, (a) 700 °C, (b) 800 °C and (c) 900 °C.

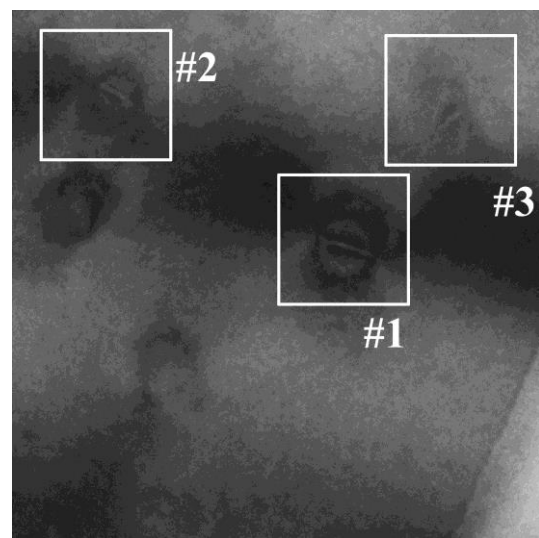
4.3.2.3 The growth of bubble discs with increasing He fluence

Although a number of publications have reported the existence of plan-view helium platelets and discs with ex-situ TEM observation [96], [97], [99]–[104], [122], the in-situ technique used here was able to follow the growth of bubble discs.

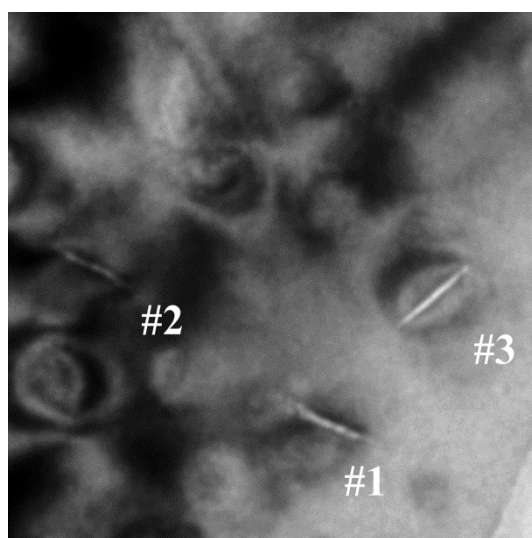
A series of TEM images of the edge-on bubble discs illustrates the significant growth with increasing He at 800 °C, as shown in Fig 4.6. The length of the edge-on bubble discs in projection and the width increases with the rise of fluence. The bubble discs are also accompanied by strain-field induced Bragg contrast.



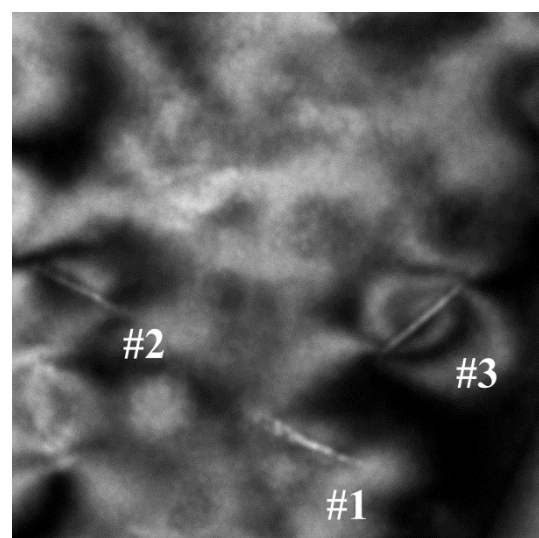
(a) 2.3×10^{16} ions.cm⁻²



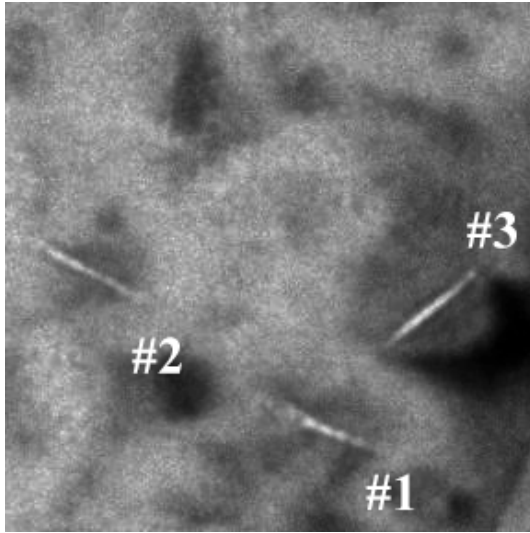
(b) 3.1×10^{16} ions.cm⁻²



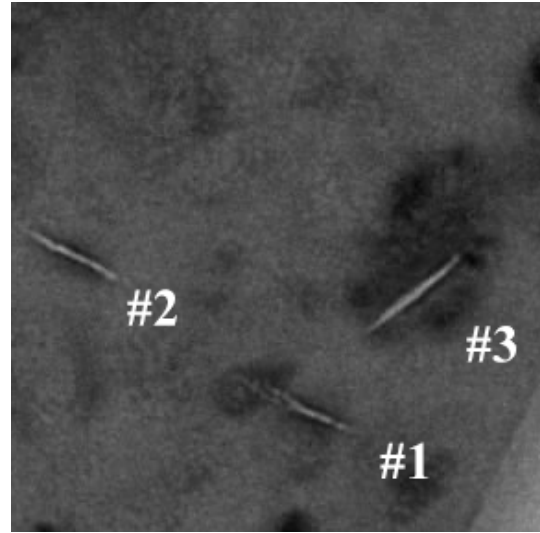
(c) 3.8×10^{16} ions.cm⁻²



(d) 4.6×10^{16} ions.cm⁻²



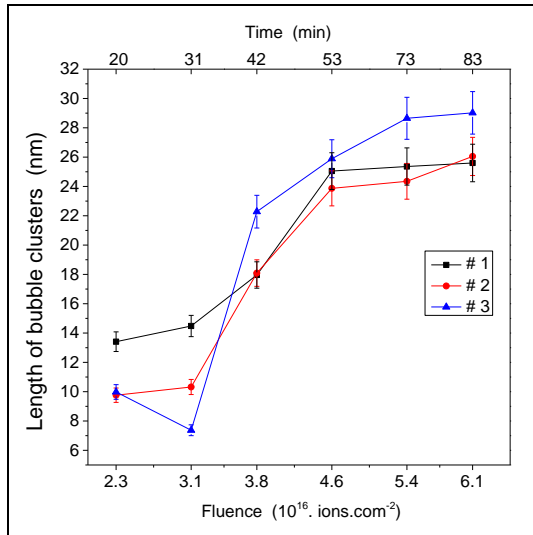
(e) 5.4×10^{16} ions.cm⁻²



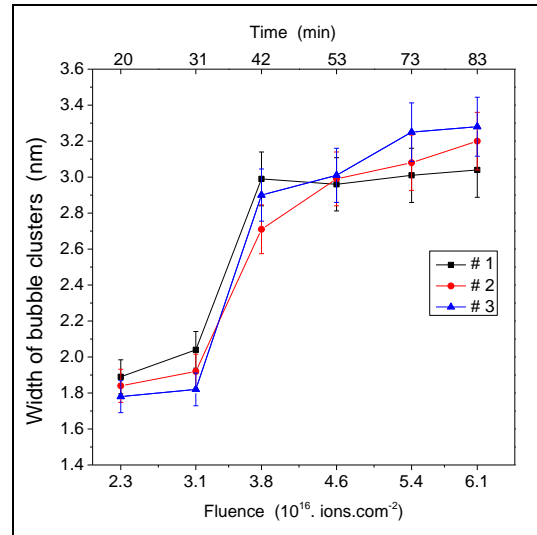
(f) 6.1×10^{16} ions.cm⁻²

Fig 4.6: The growth of edge-on bubble discs at 800 °C with different fluences. Scale bar in the first image applies to all panels.

The length and width of bubble discs in the images were measured in software ImageJ and the resulting measurements are analysed by Origin Pro 9.0. With the increase of fluence from 2.3×10^{16} ions.cm⁻² to 6.1×10^{16} ions.cm⁻², the mean length grew from ~10 nm to ~30 nm. In the Fig 4.7, there was a significant increase of the mean length between the fluence of 3.1×10^{16} ions.cm⁻² and 4.6×10^{16} ions.cm⁻² before the of growth slowed above the fluence of 4.6×10^{16} ions.cm⁻². The bubble discs tended to stop growing after irradiated with a fluence of 5.4×10^{16} ions.cm⁻². The final sizes of discs were ~30 nm. Fig 4.7 shows the increase in bubble discs width at 800 °C. The graph illustrates that the width of bubbles discs rise to maximum values of approximately 3.3 nm. Compared to the length increase, width increase is relatively small. During the irradiation process, the bubble discs kept the shapes as discs (or platelets).



(a)

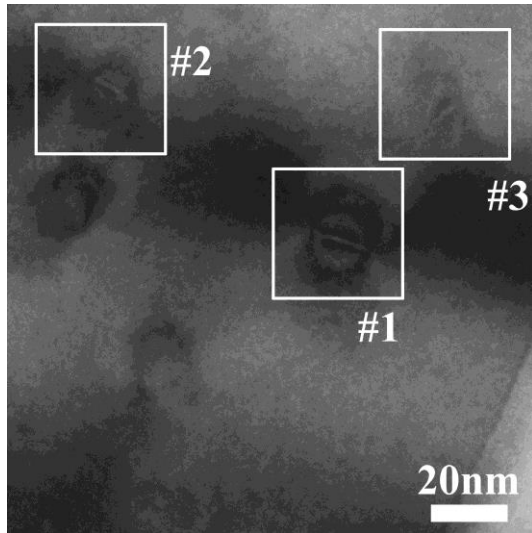


(b)

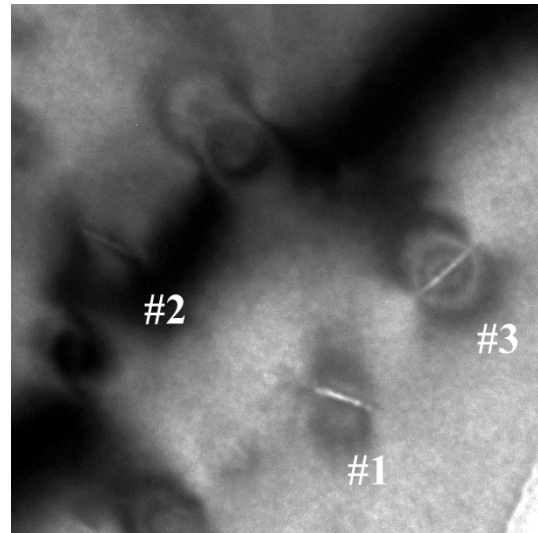
Fig 4.7: The length (a) and width (b) increase of bubble discs at 800 °C with increasing He fluence. Note that the time on the upper axis includes irradiation time and the holding time required for image capture (during which irradiation was not performed but the sample was held at temperature).

4.3.2.4 The growth of bubble discs whilst held at 800 °C

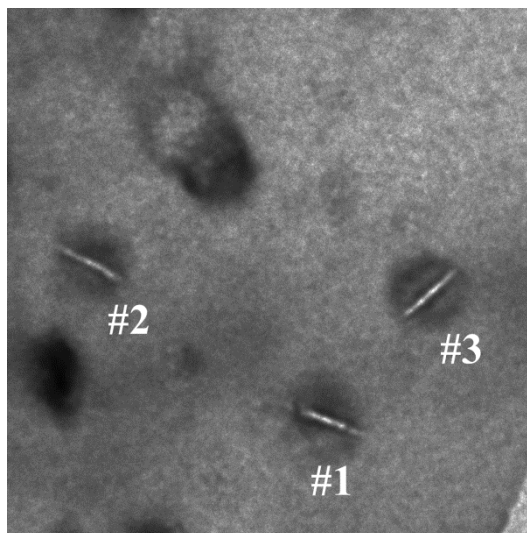
This results discussed here was obtained from the same experiment as above, helium implantation were paused at a fluence of 3.8×10^{16} ions.cm⁻². The sample has been held at the temperature of 800 ° for 6 minutes. The bubble discs exhibited significant growth during this time. Images were taken every two minutes, as shown in Fig 4.8. Note that at both irradiating time and temperature hold periods, the electron beam was left on.



(a) 1min



(b) 3min



(c) 5min

Fig 4.8: The growth of bubble discs with annealing at 800 °C at 3.8×10^{16} ions.cm⁻².

Scale bar in the first image applies to all images.

Fig 4.9 shows the growth charts of the growth of the bubble discs. The length of the #1 edge-on bubble discs grew slowly, while the length of #2 and #3 underwent a dramatic increasing during the sample being held at 800 °C. The length increase rate was extremely high during 1~3 min. The width of those three bubble discs had a uniform growth during this time range. The growth of the bubble discs was probably facilitated by the capture of vacancies and helium from the surrounding material still present from the preceding irradiation. However, the length tended to saturate after a few minutes under these conditions. It will be discussed later in section 5.4.

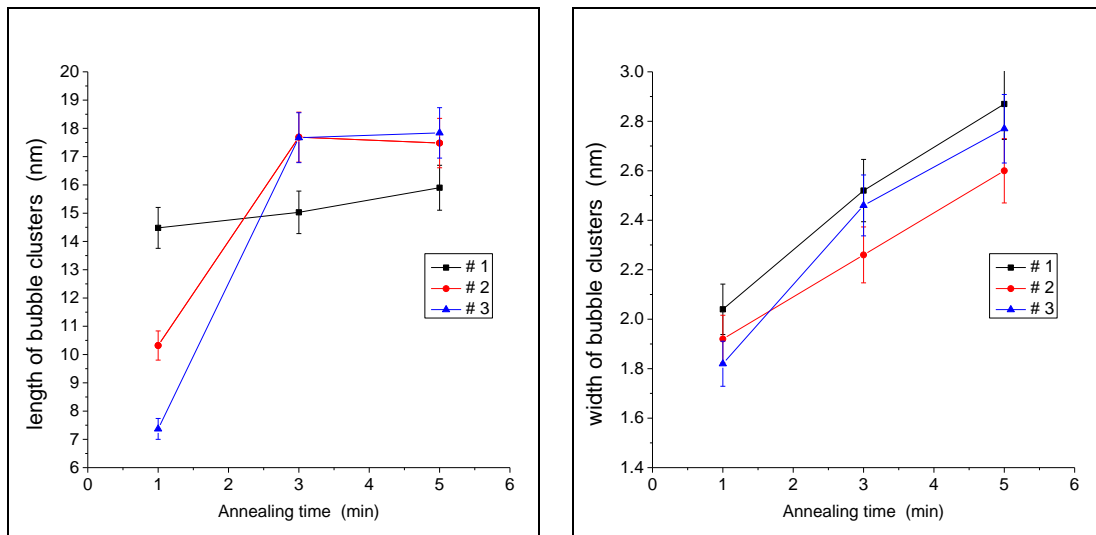


Fig 4.9: The growth curve of bubble discs during the holding time

4.3.2.5 Final size distribution of bubble discs

The statistical analysis of the length of final sizes of edge-on bubble discs (viewed close to [001] down-zone axis) at a fluence of 6.1×10^{16} ions.cm⁻² at 900 °C is shown in Fig 4.10. The length distribution histograms are created by binning length statistics using bins 2 nm wide with a maximum length of 56 nm. The sample size was 104 bubble discs, taken from different images on the (001) plane. Then a Gauss distribution is fitted, which is shown as a black curve in the chart.

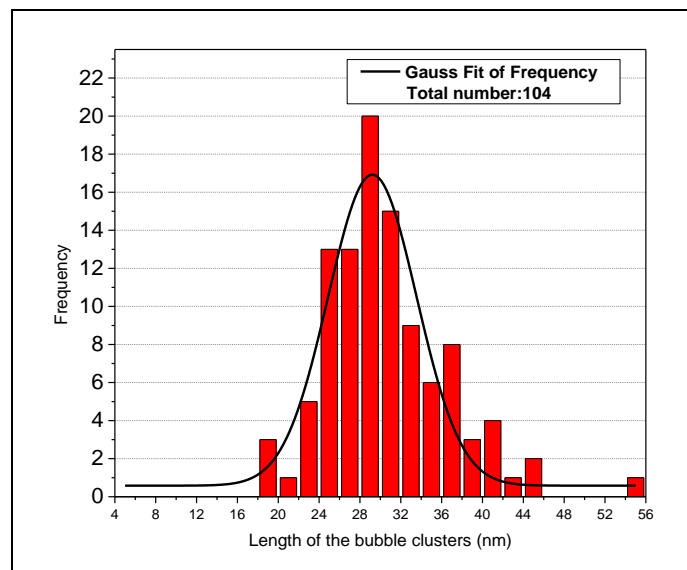


Fig 4.10: Final length distribution of bubble discs at 900 °C at a fluence of 6.1×10^{16} ions.cm⁻²

Some parameters of Gauss fitting are given in Table 4.2. The Adj. R-Squared is short for the adjusted R². R² represents the coefficient of determination in statistics, which provides a measure of how well observed outcomes fit the model. The adjusted R-Squared used in Origin Pro 9 is a modified value of R-Squared, which has been adjusted for the number of predictors in the model. Only when the new term improves the model more than expected, does the adjusted R-squared increase. The adjusted R-squared decreases when a predictor improves the model by less than expected by chance. The Adj. R-Squared=0.90 means that the distribution approximately obey the normal distribution. And the majority of sizes of the bubble discs are around 29.22 nm at 900 °C. The standard error of ± 0.34 is comparatively small.

Table 4.2: The parameters of Gauss fit of the final length distribution in projection at 900 °C
with a fluence of 6.1×10^{16} ions.cm⁻²

Model	Gauss distribution
Adj. R-Squared	0.89797
Peak Value	29.21655
Standard Error	±0.34481

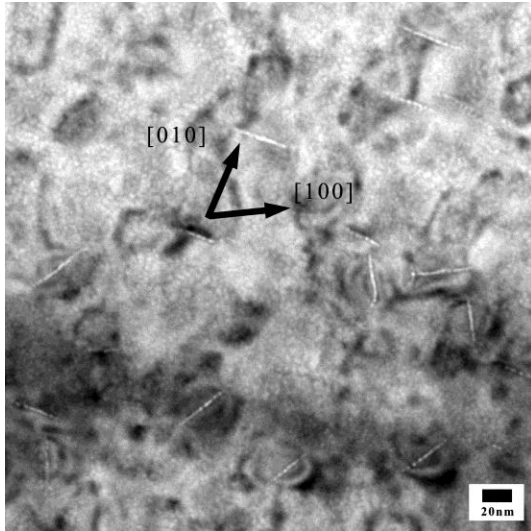
4.3.2.6 The crystallographic orientation of the edge-on bubble discs

4.3.2.6.1 The orientation of the edge-on bubble discs viewed in [001]-zone condition

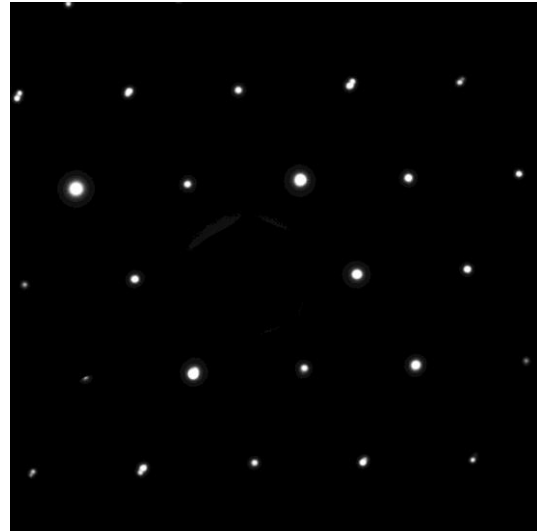
The planes on which the bubble discs lie are investigated in this section. The edge-on bubble discs observed down the [001] zone have different orientations. In the Fig 4.11, habit planes were indexed by comparing the diffraction patterns and images. Fig 4.11(a) shows a TEM image of typical edge-on bubble discs at a fluence of 6.1×10^{16} ions.cm⁻² at 900 °C; Fig 4.11(b) is the diffraction pattern from the same area. Then the indexing of the habit planes was performed with the software JEMs [126], as shown in Fig4.11(c).

The bubble discs were found to be preferential located on some specific habit planes. The orientations of the bubble discs were analysed and the results are shown in Fig 4.12(a). The angles were measured with respect to the positive horizontal direction of the TEM images. Gauss-distribution multi-peak fitting is performed as below. The calculated result and multi-peak fitting curve are shown in Fig 4.12(b) and Table 4.3. The Adj. R-Square=0.989 indicates that the statistics of orientation fits the multi-peak model well. The fitting peaks appeared at angles of 35.00 °, 100.92 ° and 156.85 °, shown in Table 4.3. The angles separation between these peaks is approximately 61 ± 5 °. The habit planes were (100), (010) and ($\bar{1}$ 10), as indicated in Fig 4.12. The reasons why such bubble discs lay on these specific planes are discussed in Section 5.6.

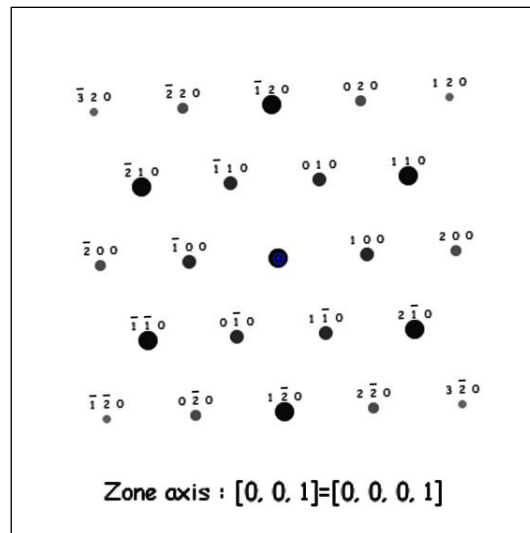
In Fig 4.12, the number of edge-on bubble discs observed around 35 ° was almost the same as the number around 157 °, while the number around 101 ° was relatively smaller. This may be due to the sample size and effects associated with the direction of irradiation and sample geometry.



(a)



(b)



(c)

Figure 4.11: (a) Image of edge-on bubble discs lying on (001) plane at 900 °C at a fluence of 6.1×10^{16} ions.cm⁻²; (b) The diffraction pattern of [001] zone in the corresponding area; (c) The [001] zone indexing generated by JEMs

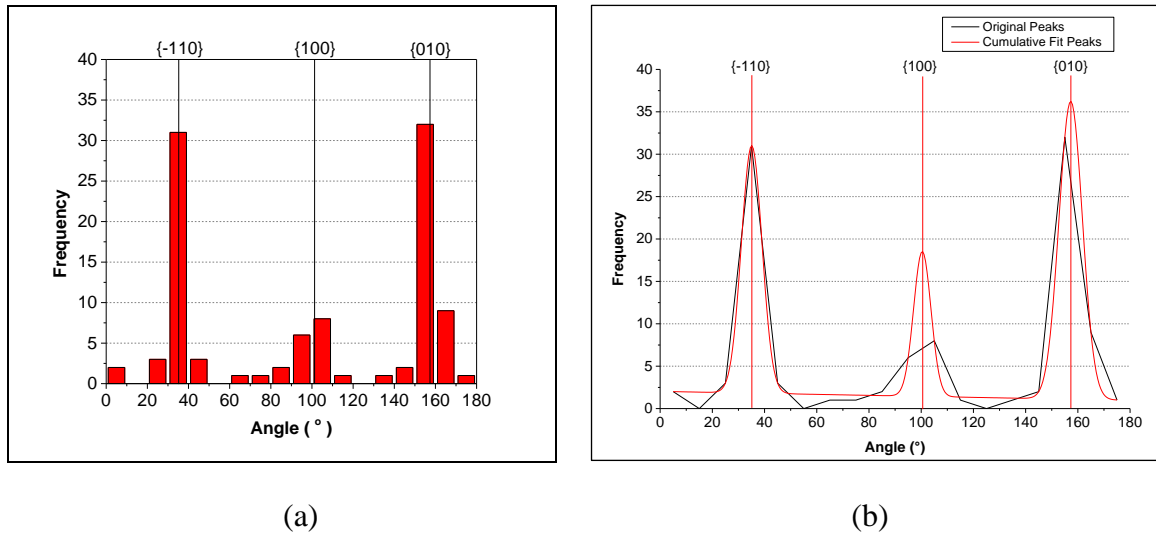


Fig 4.12: Distribution of the angles of the bubble discs and fitting curve at 900 °C at a fluence of 6.1×10^{16} ions.cm⁻²

Table 4.3: Result of Gauss-distribution Multi-peak fitting of angle distribution of the bubble discs at 900 °C at a fluence of 6.1×10^{16} ions.cm⁻²

Feature	Value (°)	Standard Error
Peak1	35.00	±0.52171
Peak2	100.92085	±1.08544
Peak3	156.85429	±0.44503
Adj. R-Square	0.988725829	

4.3.2.6.2 The orientation of the edge-on bubble discs viewed in other down-zone directions

The sample was tilted with the double-tilting heating sample holder. With the help of Kikuchi lines and diffraction indexing using JEMS, theoretical and experimental Zone-Axis Pattern Maps (ZAPMaps) between the [-123], [101] and [001] zones were created as shown in Fig 4.13 and Fig 4.14, respectively.

Edge-on bubble discs were detected when viewed in different down-zone axes, as shown in Fig 4.15. Calculated angles α from the [001]-zone to the various zones shown in Fig 4.13 and Fig 4.14 can be calculated by using Equation 4.1 for hexagonal crystallographic systems:

$$\cos \alpha = \frac{h_1 h_2 + k_1 k_2 + \frac{1}{2}(h_1 k_2 + h_2 k_1) + \frac{3a^2}{4c^2} l_1 l_2}{\sqrt{(h_1^2 + k_1^2 + h_1 k_1 + \frac{3a^2}{4c^2} l_1^2)(h_2^2 + k_2^2 + h_2 k_2 + \frac{3a^2}{4c^2} l_2^2)}} \quad (4.1)$$

Table 4.4 gives the angles between the [001]-zone and other zones. The numbers of edge-on bubble discs detected on different zones are also presented in Table 4.4.

Table 4.4: Calculated angles from the [001]-zone to various zones in its surrounding ZAPMap shown in Fig 4.13 and Fig 4.14.

Zone	[001]	[102]	[101]	[113]	[012]	$[\bar{1}23]$
Angle	0°	10.0°	19.4°	11.5°	10.0°	11.5°
Sample size of edge-on bubble discs	104	71	46	55	52	28

In the Fig 4.16, the statistical analysis of edge-on bubble discs viewed on different zones indicates that the peak of angle distribution appears around ~35°, ~101° and ~157° when viewed on each zone-axis. Therefore, the distributions of angles with respect to the positive horizontal direction didn't change with all these tilt angles from [001] zone. This indicates that the on-edge discs have the same orientations as deduced from the observation made along the [001] zone-axis. The reasons are discussed in the Section 5.6.

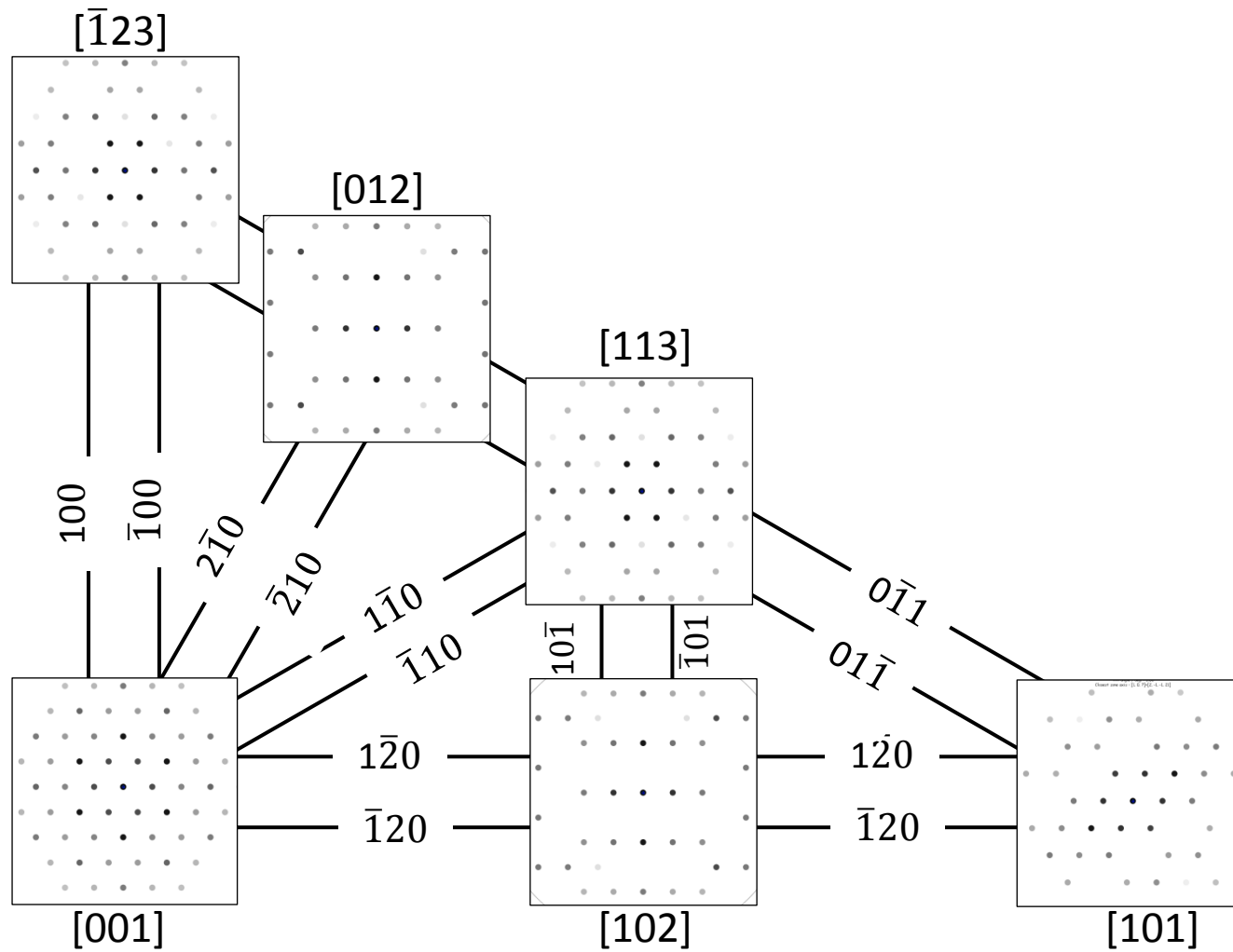


Fig 4.13: Schematic of zone-map showing low-order zones and selected Kikuchi lines derived from JEMs

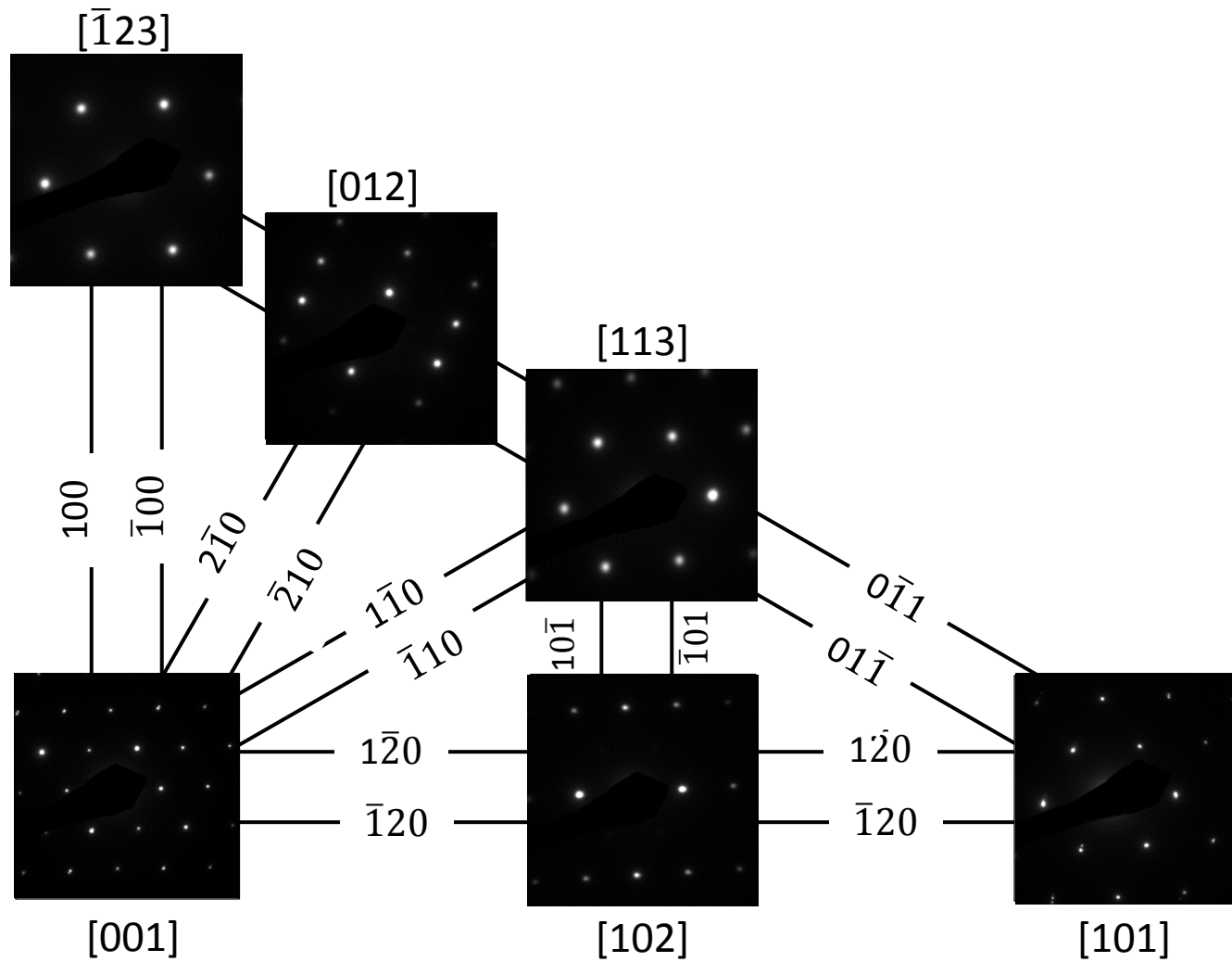


Fig 4.14: Schematic of zone-map with diffraction patterns from the experiment

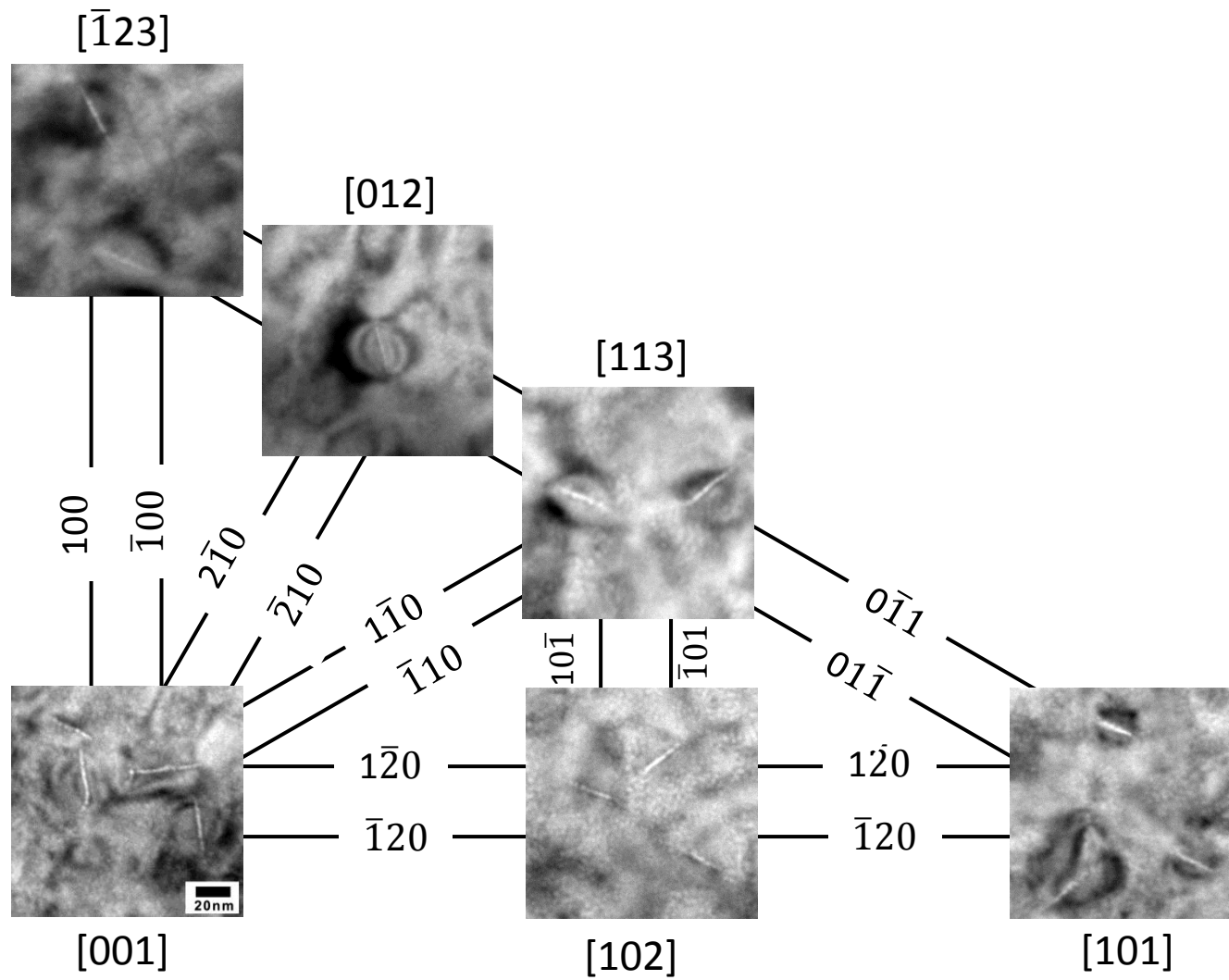


Fig 4.15: Edge-on bubble discs observed in different down-zone directions

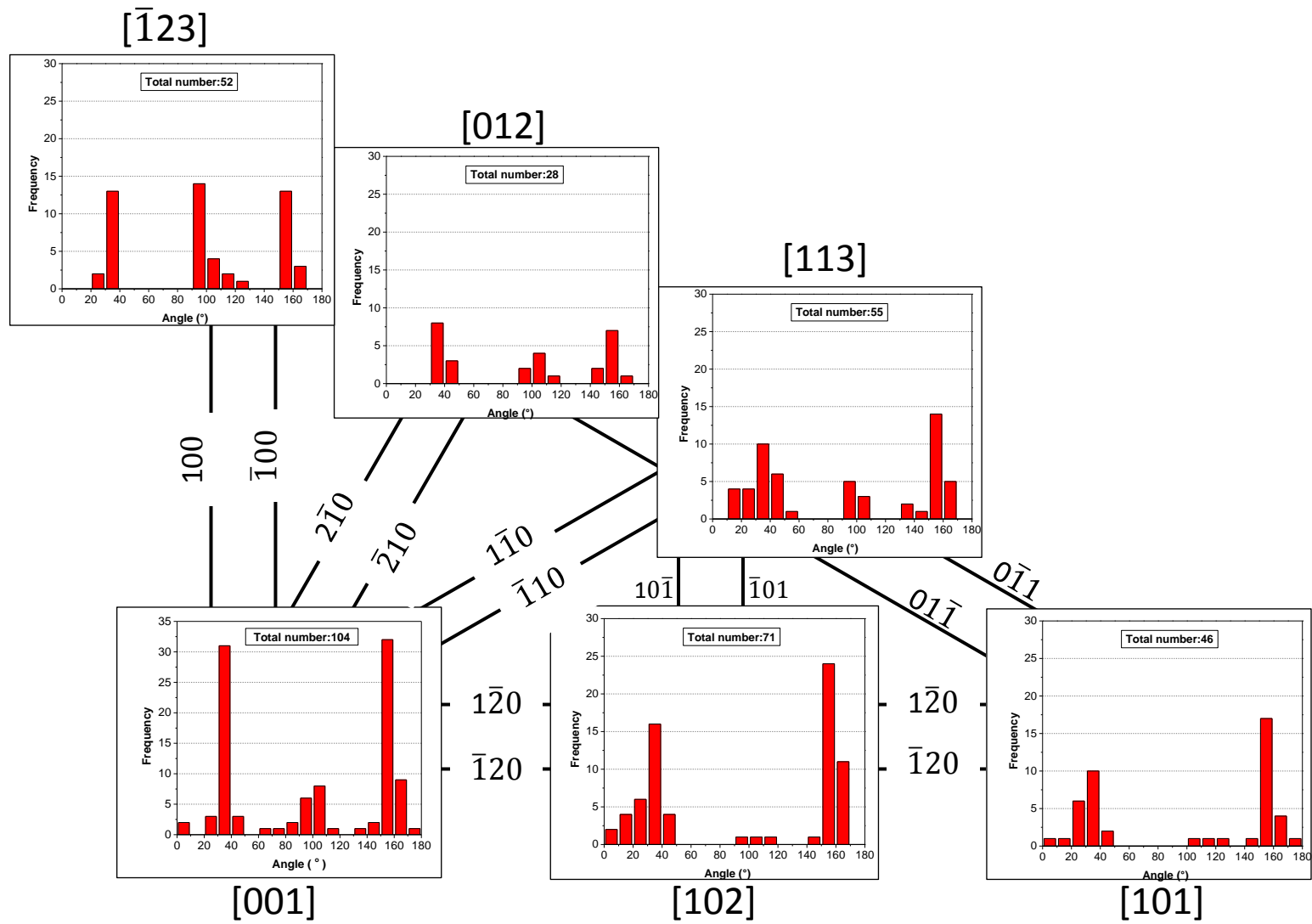


Fig 4.16: Angle distributions of edge-on bubble discs observed in different down-zone conditions

4.4 Summary

This chapter contains experimental results from in-situ 3.5 keV He ion-irradiation and TEM observation of SiC samples at either 700 °C, 800 °C or 900 °C. TEM images were captured regularly throughout the irradiation and videos were recorded. Bubbles and bubble discs were detected in the irradiated areas at all temperature studied. The size of bubble discs was increasing with the increase of helium fluence and bubble discs were observed to grow further whilst being held at 800 °C after a fluence of 3.1×10^{16} ions.cm⁻². Samples were irradiated to a maximum fluence of $\sim 6.1 \times 10^{16}$ ions.cm⁻² at which the bubble appeared to stop growing. The edge-on bubble discs observed close to [001] down-zone axis are formed on {100}, {010} and $\{\bar{1}10\}$ planes.

5. Discussion

5.1 The growth mechanism of the bubble discs

The helium irradiation of SiC has been reported previously and a transformation from helium platelets to bubble discs of small bubbles has been detected [81], [106]–[110]. Isolated bubbles and bubble discs were both formed at a thickness of ~50nm of the samples. In the present work, it is speculated that the helium platelets are formed at the beginning and then they collapsed into discs of small bubbles. Unfortunately, the transformation wasn't detected in the experiments. It may due to: (a) small change in contrast between platelets and bubble discs; (b) sample movement. It is hard to maintain the same area and Bragg conditions during the irradiation. But the nucleation of platelet-shaped cavities at the beginning may be necessary for the formation of bubble discs because isolated bubbles are energetically favoured to be formed rather than bubble discs if no platelet was formed. Meanwhile, the similar evolution has been reported in helium-implanted Mo although detailed mechanism still remained in questions.

The helium platelets and bubble discs have been found in some other materials after helium irradiation, for example, Si [127], B₄C [128], Ti [129] and Mo [130]. But few papers have discuss the evolution of helium platelets (bubble discs). Evans developed a theory to describe the evolution of helium platelets in metal Mo [131]. The bubble discs evolved from helium trapped vacancy clusters are written as He_xV_y, for example, He₂V, He₃V, He₄V₂ (V is short for vacancy) [131]. Then the vacancy clusters gain new space by ejecting the nearby matrix atoms, which is called trap mutation process. These matrix atoms become interstitials and are binding to the helium vacancy clusters. The dislocation loops are formed by the interstitials surrounding the platelets. the platelets nucleate. Then the platelets grow by loop punching. However, the theory can't explain what lead to the different nucleation of isolated bubbles and helium platelets in our experiments. Meanwhile, the loop punching process can't explain the length growth of the bubble discs. The hypothesis from Chen and his co-workers shows a little different nucleation of helium platelets [81]. The schematic of a helium platelet is shown in Fig 5.1. They thought the platelets nucleated from the crack between two lattice layers. It is reasonable that platelets nucleate between the cracks of two lattice layers and grow by loop punching in Chen's experiment, because helium platelets have a uniform thickness of 0.6nm, corresponding to approximately 2.4 lattice layer along [001] direction [81]. While the bubble discs formed in the present work have a thickness of 3.3±0.25 nm,

corresponding to approximately 12 lattice layers along [001] direction and 11 lattice layers along [100] direction. It is unlikely that helium platelets/bubble discs gain so much lattice space without trap mutation process in our case. But both of Evans and Chen agreed that dislocation loops were formed and the bubble discs subsequently grew by loop punching.

There are apparently plenty of vacancies clusters and interstitials in the irradiated areas. During the high temperature implantation periods and the temperature holding periods, Some vacancy-interstitial pairs are recombined and some evolve to become helium bubbles and bubble discs. We speculate that the location of helium trapped vacancy clusters in the lattice and the distance between these vacancy clusters may affect the different nucleation in SiC. Those vacancy clusters which is close to each other and are generated near specific low energy planes coalesce together, when the lattice atoms between them can be easily kicked out by trap mutation to turn into interstitials. The interstitial C and Si have a migration energy of 0.74 eV and 1.53 eV [132], respectively, which is much lower than the migration energy of C vacancies (3.2-3.6 eV) and S vacancies (3.5-5.2eV) [133]. Thus, the interstitial C and Si atoms are able to migrate and are trapped between specific low energy planes to form interstitial dislocation loops, for example, (001) and (100) planes. These vacancy clusters surrounding by interstitial dislocation loops act as nuclei of helium platelets. Then the platelets grow by loop punching. Meanwhile, trap mutation process takes place to transform the lattice atoms at the edge of the platelets into interstitials during the growth. These interstitials are then trapped in the dislocation loops. This process could be the explanation of the length growth of helium platelets. The big growth rate at fluences of 3.1×10^{16} ions/cm² and 3.8×10^{16} ions/cm² indicates that loop punching and trap mutation can easily take place at the beginning so that the platelets are able to gain space and grow fast. The processes are driven by the relaxation of inner pressure of the platelets. The inner helium pressure dropped discontinuously during this process [134]. This may lead to the collapse of helium platelets. The transformation from platelets to bubble discs occurs after the collapse and some of the interstitial atoms return back into the lattice sites. It is believed a cluster of small spherical bubbles have lower energy than a single platelet [135].

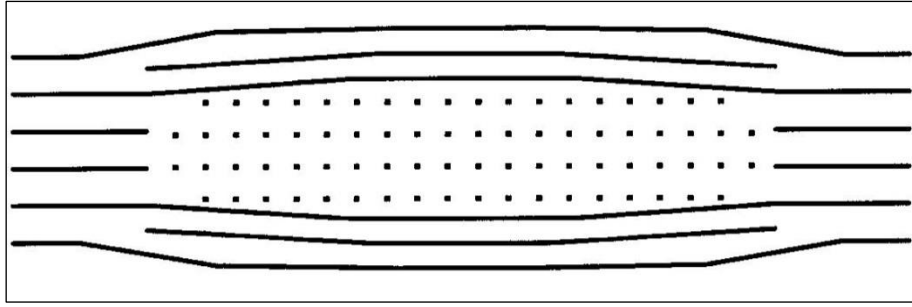


Fig 5.1: schematic of a helium platelet, bound by two dislocation dipoles on both sides. The dots represent helium atoms and the black lines indicate lattice planes. (Reproduced from [81])

5.2 The motion of helium atoms and helium bubbles

5.2.1 Motion of helium atoms

The motion of helium atoms is considered as the helium diffusion process in SiC. The vacancies with trapped helium atoms don't move in this experiment, because it is believed that the mobility of vacancies in SiC is only possible at temperatures higher than 1260 °C [118], [119]. So at this temperature range of 700–900 °C, the dissociative/interstitial mechanism is deduced to explain the diffusion of helium atoms. The helium atoms are detrapped from defects (interstitials, vacancies, or other complexes) and then interstitial helium diffuse, which is shown in equation 5.1 [118]:



As it is reviewed in section 2.5.1, the activation energy for helium is expected to be ~1.1 eV. The electron beam may also affect the helium diffusion process in the TEM.

5.2.2 Motion of helium bubbles

Bubbles which have a size smaller than resolution of FX2000-TEM could not be visible in this work. So mobility of these bubbles were unknown in this work. However, by the time bubbles were large enough to be observed in the TEM, no motion of bubbles was observed. Thermally-activated bubble motion in metals [136], [137] and semi-conductors [138], [139] has been reported before. Whereas, there are rare reports of helium bubble motion in SiC around this temperature range of 700–900 °C in published literatures. Pawley has analysed that the small helium atoms and helium atoms clusters may be able to be diffuse and gather to form bubbles with immobile sizes [49]. Therefore, it is concluded observable helium bubbles formed are pinned in position and unable to move.

The small helium bubbles inside the bubble discs keep spherical shape and are not able to move after the transformation from platelet to bubble discs. Fourier transforms of the images inside the discs should be taken in further work to check whether bubble lattice forms inside the cluster. The formation of bubble lattice are considered as a much stable way of distribution of defects, which may be similar to void lattice [140].

5.3 The growth and growth rate of bubble discs

In the irradiation experiments at the 800 °C and 900 °C, the edge-on bubble discs viewed close to the [001] zone-axis were growing with the increasing helium fluence (see section 4.3.2.3). The mean final length and width of bubble discs at 900 °C reached ~30nm and ~3nm. The grow rate increased before the fluence of 3.8×10^{16} ions.cm⁻² and then the growth slowed down. The growth stopped at with the fluence of 5.4×10^{16} ions.cm⁻². At 700 °C, much fewer bubble discs were observed. There appeared to be a temperature threshold around 700 °C to make the difference. Since no in-situ irradiation experiment of bubbles clusters growth have been done before, the data here shows the first experimental growth process, which is of great value. More data are needed in the further work.

5.4 Analysis of bubble growth during temperature holding period

During the holding period of the experiment at 800 °C after a fluence of 3.8×10^{16} ions.cm⁻², the bubble discs continue to grow rapidly (see section 4.3.2.4). This could be explained as follows. Before the annealing there were helium atoms trapped in vacancies and interstitials because of the very high implanting flux of 2.5×10^{13} ions .cm⁻².s⁻¹. The temperature played the dominating role of the bubble discs growth and the temperature holding periods provided additional time for helium diffusion. At the same time, the energetic electron beam of TEM also might make a contribution. Energy was transferred to helium through the collisions between electrons and helium atoms (or helium-trapped defects). This facilitates helium atoms to overcome the energy barrier and migrate. But this would be the lesser factor because the transferred energy is low.

5.5 The final size distribution of bubble discs

The final sizes of bubble discs are mainly decided by the three main factors: the helium fluences, the irradiation temperatures and the lying-on planes of bubble discs.

As it is described in section 4.3.2.3, bubble discs grow with the helium fluence before they get saturated.

The final sizes are also closely related to temperature. A variety of papers have reported the sizes of bubble discs lying on {001} planes. In the temperature range of 700~900 °C, helium platelets with size of ~9 nm diameter and ~ 0.6 nm thickness were formed in the matrix on {001} planes in Chen's work [81], [110]. Whereas in current work, bubble discs

with sizes of ~30 nm in diameter and ~3 nm in thickness were formed. When the experiment temperature becomes higher than 1050 °C, bubble discs grow bigger [109]. Large platelet-shaped bubble-loop complexes with a diameter of 200 nm have been observed [81].

The mean final size of edge-on bubble discs, which actually lay on {100} planes (see section 5.6 ahead) is ~30 nm in diameter and ~3 nm in thickness. The mean final size of bubble discs lying on {001} planes were not measured in the experiments reported here. It is expected that the final size difference maybe existed between the bubble discs lying on these two planes, due to the little different interplanar spacing. However, the {100} planes with plane spacing of 0.2661nm and the {001} planes with plane spacing of 0.2513nm are two of the closest packing planes in 4H-SiC and have the biggest spacing between the layers. More lattice space is supplied for the helium platelets and bubble discs. The big spacing not only makes the formation of platelets easier to grow in both axial and radial directions, but also makes the dislocation dipoles easier to emit and glide along the close-packing direction. That means, the helium platelets and bubble discs lying on {001} planes may grow bigger than the others before they reach the strain balance between the inside gas pressure and the elastic constraint caused by the lattice atom distortion.

The thickness of samples affects the final sizes of edge-on bubble discs. The overpressure of the platelets and discs releases when they reach the surface of the TEM samples.

In addition, Zhang reported that mono-energetic helium irradiation cause higher ratio of local helium trap than multiple-energy implantation and then lead to bigger sizes of helium platelets [108].

5.6 Preferential habit planes of the bubble discs

5.6.1 The bubble discs viewed in [001] direction

In these experiments, bubble discs were found lying on different planes. For example, as shown in the Fig 4.4, both plan-view bubbles discs lying on {001} planes and edge-on bubble discs are observed when viewed in [001] down-zone direction.

Since 4H-SiC crystalline has a hexagonal structure, it has a property of rotational symmetry on its basal (001) plane. The order of rotational symmetry for an hexagonal structure is 6, which means when it plane rotates by an angle of 60° , the state of the structure will stay the same. The Fig 4.11 above reveals that the angles with respect to horizontal positive direction of the TEM images of the edge-on bubble discs were approximately 35° , 101° and 157° . The angle differences between orientations are approximately 60° and 120° . Therefore, it can be inferred that three preferential planes are equivalent planes.

When observed close to [001] zone, typical orientated on-edge bubble discs are shown in Fig 5.2(a). Fig 5.2(b) presents a plan view of a (001) plane created using Crystalmaker 9.2 software. The equivalent planes: {100}, {010}, {-110}, which is highlighted in Fig 5.2(b) are expected to be the preferential habit planes for the bubble discs. This is because these are the relative close-packing planes compared to other planes perpendicular to (001) plane. As what we analysed in above section 5.5, the relative close-packing planes possess a relative bigger spacing. This character makes them be the preferential choice for bubble discs to lie on. Then the conclusion was drawn that the edge-on bubble discs observed in [001] down-zone direction were lying on {100} planes.

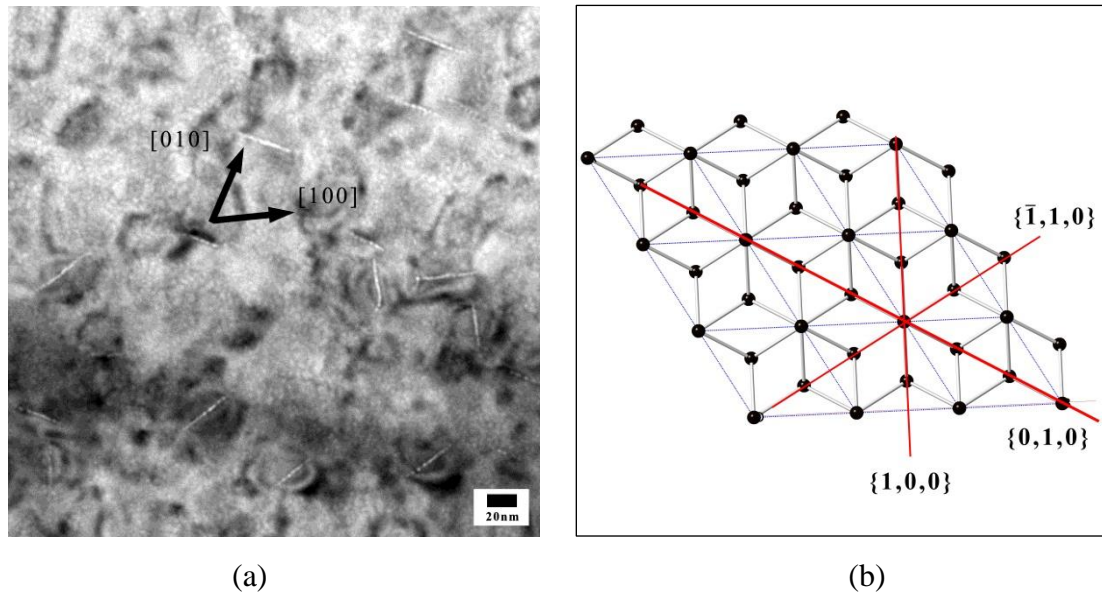


Fig 5.2: (a) TEM image of on-edge bubble discs viewed just off the [001] zone-axis; (b) the structure of (001) plane viewed on [001] zone-axis created using the Crystallmaker software.

However, the closest packed planes in 4H-SiC are the {001} basal planes. The cross section viewed in [100] direction is shown in Fig 5.3. The {001} basal planes are the most preferential planes for the bubble discs to lie on. This conclusion is reached from the many studies in which bubble platelets and clusters are widely detected lying on {001} planes in He-implantation experiments for both α -SiC and β -SiC [106–110].

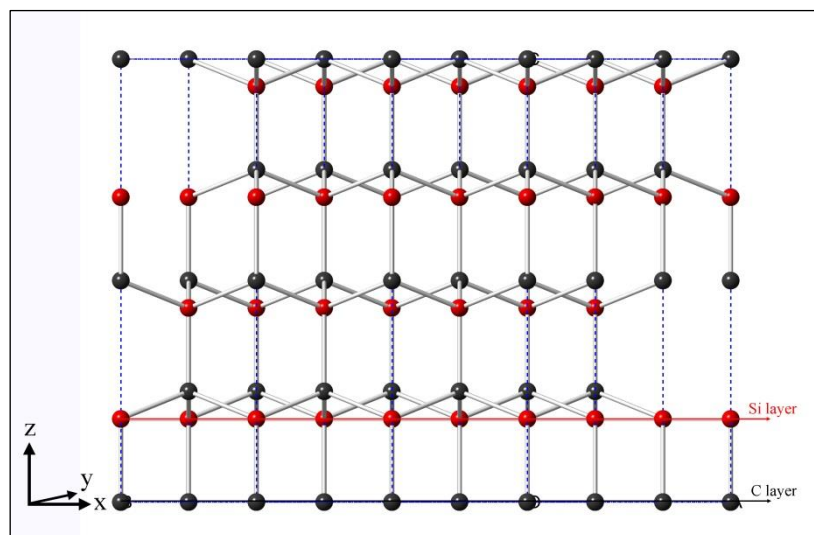


Fig 5.3: the layer structure of 4H-SiC observed in [100] direction

5.6.2 The edge-on bubble discs viewed in other down-zone directions

As it is shown in section 4.3.2.6.2, edge-on bubble discs were detected in down-zone conditions other than the [001] one. When the sample was tilted from [001] down-zone direction to other down-zone directions, it lost the rotation symmetry order of six. But the edge-on bubble discs still distributed around $\sim 35^\circ$, $\sim 101^\circ$ and $\sim 157^\circ$, which have angle difference of 60° . Thus the observations strongly suggest that the edge-on bubble discs observed in other down-zone directions are actually lying on {100} planes, which is exactly the same as the orientation of edge-on bubble discs in [001] down-zone observation.

However, when views of tilted bubble discs were analysed geometrically, the bubble discs lying on (100) planes shouldn't have the same edge-on orientation, shown in Fig 5.4. Such views of tilted view of bubble discs were rarely detected in our work. This could possibly be due to be the thickness of the areas analysed. The thickness of areas in where the bubble discs lying on {100} planes was about 50 nm or even thicker. So the contrast of features in the areas (e.g. bubbles, dislocation, especially other local bubble discs) obfuscated the contrast of tilted edge-on bubble discs.

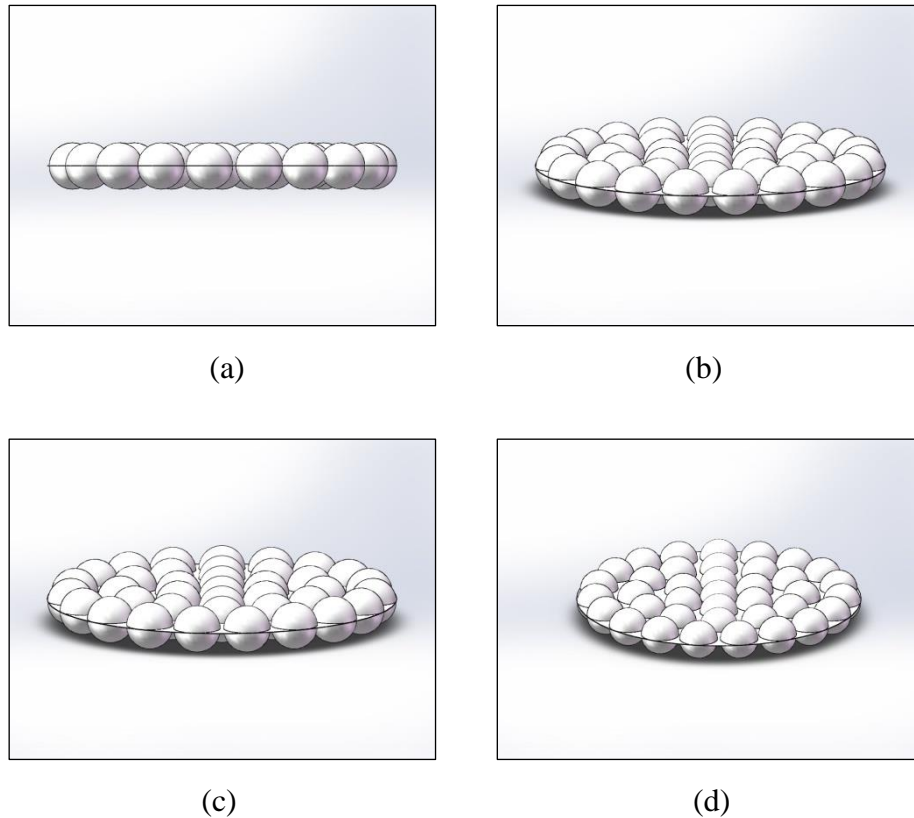


Fig 5.4: The geometrical view of bubble discs lying on (100) planes when observed at different zones: (a). Edge-on bubble discs; (b). Bubble discs viewed at the zone 10.0° off the [001] zone; (c). Bubble discs viewed at the zone 11.5° off the [001] zone; (d). Bubble discs viewed at the zone 19.4° off the [001] zone.

The angle distribution of edge-on bubble discs was the same as those observed in [001] direction when the samples were tilted far from the [001] zone. This has not been fully explained here. A possible reason may be that the areas where edge-on located bubble discs were collected were a little bit far away from the observing zone and were close to the [001] zone because of the bending of samples and the deformation of the lattice.

From what we discussed above, conclusion can be drawn that in helium irradiated SiC areas at $T_t \sim 900^\circ\text{C}$, the helium platelets and discs were formed and lie on two preferential planes in 4H-SiC. They are the {001} basal planes and the {100} planes.

6. Conclusions and Further Work

6.1 Conclusion

Experiments of helium implantation in 4H-SiC at high temperatures were conducted with the in-situ ion irradiation facility MIAMI. With the discussion and analysis above, we can be able to draw the following conclusions:

In the temperature range of 700 °C–900 °C, helium atoms diffuse via the dissociative/interstitial mechanism during the implantation of 4H-SiC. However, no noticeable motion of visible helium bubbles was observed in the TEM.

Lots of bubble discs lying on two different plane clusters were formed in the 4H-SiC matrix at 800 °C and 900 °C with significantly fewer at 700 °C. It is believed there is a temperature threshold T_t around 700 °C. 4H-SiC behaved differently below and above this threshold value.

At the temperature of 800 °C and 900 °C, the formation and growth of bubble discs are similar. The evolution of bubble discs is appeared to proceed as follows. Helium platelets nucleate at the space between two lattice planes. These planes are {001}, {100} habit planes. Then the platelets gain space via loop punching and grow. The emission and gliding away of dislocation loops are driven by the relaxation of pressure inside the helium platelets. Thus the changes of pressure are discontinuous. The platelets collapse into discs of small bubbles when the inside pressure are not able to hold the shape of helium platelet.

In the helium irradiation experiments done at 800 °C, the bubble discs grew up to a fluence of 5.4×10^{16} ions.cm⁻². The growth rate reached the peak value at a fluence of 3.8×10^{16} ions.cm⁻² and then dropped down.

Whilst held at 800 °C at a fluence of 3.8×10^{16} ions.cm⁻², the bubble discs grew rapidly because of the diffusion of helium atoms from the matrix. At the fluence of 3.8×10^{16} ions.cm⁻² at 800 °C, the sizes of bubble discs tend to saturate with a size of ~18 nm in diameter and ~3nm in thickness at the end of this period.

In the helium irradiation experiment conducted at 900 °C at a fluence of 6.1×10^{16} ions.cm⁻², the mean final length and width of edge-on bubbles discs lying on {100} planes reached ~30 nm and ~3 nm. The discs were formed on two preferential plane clusters. These are {001} planes and {100} planes, which were the close-packing planes with bigger interplanar crystal spacing than the other planes.

6.2 Further work

The mean size of isolated helium bubbles likely has a close relationship with the irradiating temperature, which haven't been focused on in this works. Thus the size distribution of isolated bubbles at this temperature range needs further research in the future.

The sizes of bubble discs formed at different temperatures should be compared and a function between temperature and sizes of bubble discs can be conducted. The sizes difference of the bubble discs lying on {001} and {001} should be investigated as well.

The transformation from helium platelets to bubble discs needs more investigation. The energy state inside the helium platelets and discs should be compared. In order to capture this transformation, Pre-He-irradiated cross-section samples, which contain platelets, should be made and be used to do in situ helium irradiation. Furthermore, in most of previous ex-situ experiments, most of platelets/discs observed are lying on the {001} basal planes. Thus, with the help of such kind of samples, it would be possible to find out whether bubble discs lying on {100} planes could be formed in these Pre-He-irradiated cross-section samples during the in-situ irradiation.

The precise temperature threshold proposed T_t around 700 °C which affects the number density of bubble discs in the irradiated areas could be investigated in the further work. Also, the temperature effect on final sizes of isolated bubbles, the bubble discs and bubble inside the bubble discs should be researched as well.

In the experiments, helium was implanted into SiC with an angle of 30° from the normal of surface. Since the implanting angle may affect the planes of bubble discs to lie on, experiments of perpendicular implantation and other incident angles to the SiC surface should be done in the further work.

After helium irradiation the mechanic properties need to be examined. For instance, the blistering and expansion are important for cladding use. Meanwhile, hardness and high temperature tensile strength are crucial factors for the structure component materials.

References

- [1] R. Cheung, *Introduction to Silicon Carbide Microelectromechanical Systems*, UK: Imperi. London, 2006.
- [2] V. A. Izhevskiy, L. A. Genova, J. C. Bressiani, and A. H. A. Bressiani, "Review article: silicon carbide. Structure, properties and processing," *Cerâmica*, vol. 46, no. 297, pp. 4–13, Mar. 2000.
- [3] E. S. Sadow and A. Adarwak, *Advances in silicon carbide processing and applications*. Boston: Artech House, 2004.
- [4] A. H. Cowless and E. H. Cowless, "Preparation of SiC," 319.9451885.
- [5] H. G. Grimmeiss and J. W. Allen, "Light emitting diodes – How it started," *J. Non. Cryst. Solids*, vol. 352, no. 9–20, pp. 871–880, Jun. 2006.
- [6] Y. M. Tairov and V. F. Tsvetkov, "General principles of growing large-size single crystals of various silicon carbide polytypes," *J. Cryst. Growth*, vol. 52, pp. 146–150, Apr. 1981.
- [7] Y. M. Tairov, "Growth of bulk SiC," *Mater. Sci. Eng. B*, vol. 29, no. 1–3, pp. 83–89, Jan. 1995.
- [8] R. P. Devaty and W. J. Choyke, "Optical Characterization of Silicon Carbide Polytypes," *Phys. Status Solidi*, vol. 162, pp. 5–38.
- [9] Y. M. Tairov and V. F. Tsvetkov, "Progress in controlling the growth of polytypic crystals," *Prog. Cryst. Growth Charact.*, vol. 7, no. 1–4, pp. 111–162, Jan. 1983.
- [10] J. R. Glass, D. Henshall, V. Tsvetkov, and C. Carter, "SiC-Seeded Crystal Growth," *Phys. Status Solidi*, vol. 202, pp. 149–162.
- [11] Accuratus, "Silicon Carbide, SiC Ceramic Properties," 2013. [Online]. Available: <http://accuratus.com/silicar.html>.

- [12] M. Bhatnagar and B. J. Baliga, "Comparison of 6H-SiC, 3C-SiC, and Si for power devices," *IEEE Trans. Electron Devices*, vol. 40, no. 3, pp. 645–655, Mar. 1993.
- [13] G. L. DesAutels, P. Powers, C. Brewer, M. Walker, M. Burky, and G. Anderson, "Optical temperature sensor and thermal expansion measurement using a femtosecond micromachined grating in 6H-SiC," *Appl. Opt.*, vol. 47, pp. 3773–7.
- [14] D. N. Talwar and J. C. Sherbondy, "Thermal expansion coefficient of 3C-SiC," *Appl. Phys. Lett.*, vol. 67, no. 22, p. 3301, 1995.
- [15] Accuratus, "Silicon Carbide, SiC Ceramic Properties," 2013. .
- [16] N. P. Bansal, *Handbook of Ceramic Composites*, NASA Glenn. 2005.
- [17] M. Capano and R. Trew, "Silicon carbide electronic materials and devices," *MRS Bull.*, vol. 22, no. 03, pp. 19–24, 1997.
- [18] Y. A. Zeng, M. H. White, and M. K. Das, "Electron transport modeling in the inversion layers of 4H and 6H-SiC MOSFETs on implanted regions," *Solid. State. Electron.*, vol. 49, no. 6, pp. 1017–1028, Jun. 2005.
- [19] A. Pérez-Tomás, P. Godignon, N. Mestres, and J. Millán, "A field-effect electron mobility model for SiC MOSFETs including high density of traps at the interface," *Microelectron. Eng.*, vol. 83, no. 3, pp. 440–445, Mar. 2006.
- [20] M. Riccio, A. Castellazzi, G. De Falco, and A. Irace, "Experimental analysis of electro-thermal instability in SiC Power MOSFETs," *Microelectron. Reliab.*, vol. 53, no. 9–11, pp. 1739–1744, Sep. 2013.
- [21] R. Saidur, M. S. Hossain, M. R. Islam, H. Fayaz, and H. A. Mohammed, "A review on kiln system modeling," *Renew. Sustain. Energy Rev.*, vol. 15, no. 5, pp. 2487–2500, Jun. 2011.
- [22] H. Kaneda, T. Onaka, T. Nakagawa, K. Enya, H. Murakami, R. Yamashiro, T. Ezaki, Y. Numao, and Y. Sugiyama, "Cryogenic optical performance of the ASTRO-F SiC telescope," *Appl. Opt.*, vol. 44, no. 32, pp. 6823–32, Nov. 2005.

- [23] K. Enya, N. Yamada, T. Imai, Y. Tange, H. Kaneda, H. Katayama, M. Kotani, K. Maruyama, M. Naitoh, T. Nakagawa, T. Onaka, M. Sukanuma, T. Ozaki, M. Kume, and M. R. Krödel, “High-precision CTE measurement of hybrid C/SiC composite for cryogenic space telescopes,” *Cryogenics (Guildf)*, vol. 52, no. 1, pp. 86–89, Jan. 2012.
- [24] A. T. Alpas and J. D. Embury, “Sliding and abrasive wear behaviour of an aluminum (2014)-SiC particle reinforced composite,” *Scr. Metall. Mater.*, vol. 24, no. 5, pp. 931–935, May 1990.
- [25] F. M. Hosking, F. F. Portillo, R. Wunderlin, and R. Mehrabian, “Composites of aluminium alloys : fabrication and wear behaviour,” *J. Mater. Sci.*, vol. 17, no. 2, pp. 477–498, 1982.
- [26] A. Banerji, M. K. Surappa, and P. K. Rohatgi, “Cast Aluminum Alloys Containing Dispersions of Zircon Particles,” *Metall. Trans. B*, vol. 14, no. June, pp. 273–283, 1983.
- [27] S. Fan, L. Zhang, L. Cheng, G. Tian, and S. Yang, “Effect of braking pressure and braking speed on the tribological properties of C/SiC aircraft brake materials,” *Compos. Sci. Technol.*, vol. 70, no. 6, pp. 959–965, Jun. 2010.
- [28] S. Fan, L. Zhang, L. Cheng, and S. Yang, “Microstructure and frictional properties of C/SiC brake materials with sandwich structure,” *Ceram. Int.*, vol. 37, no. 7, pp. 2829–2835, Sep. 2011.
- [29] X. Huang, C. Liu, X. Lv, G. Liu, and F. Li, “Aluminum alloy pistons reinforced with SiC fabricated by centrifugal casting,” *J. Mater. Process. Technol.*, vol. 211, no. 9, pp. 1540–1546, Sep. 2011.
- [30] C. Zhang, L. Zhang, Q. Zeng, S. Fan, and L. Cheng, “Simulated three-dimensional transient temperature field during aircraft braking for C/SiC composite brake disc,” *Mater. Des.*, vol. 32, no. 5, pp. 2590–2595, May 2011.
- [31] Saito, Shinzo, Tanaka, Toshiyuki, and Y. Sudo, “Design of High Temperature-engineering Test Reactor (HTTR).”

- [32] L. L. Snead, T. Nozawa, Y. Katoh, T.-S. Byun, S. Kondo, and D. A. Petti, *Handbook of SiC properties for fuel performance modeling*, vol. 371, no. 1–3. 2007.
- [33] C. W. Forsberg, P. F. Peterson, and P. S. Pickard, “Molten-salt-cooled advanced high-temperature reactor for production of hydrogen and electricity,” *Nucl. Technol.*, vol. 144, no. 3, pp. 289–302, 2003.
- [34] K. A. Terrani, L. L. Snead, and J. C. Gehin, “Microencapsulated fuel technology for commercial light water and advanced reactor application,” *J. Nucl. Mater.*, vol. 427, no. 1–3, pp. 209–224, Aug. 2012.
- [35] International Atomic Energy Agency(IAEA), *High Temperature Gas Cooled Reactor Fuels and Materials*. Vienna, 2010.
- [36] P. Hosemann, J. N. Martos, D. Frazer, G. Vasudevamurthy, T. S. Byun, J. D. Hunn, B. C. Jolly, K. Terrani, and M. Okuniewski, “Mechanical characteristics of SiC coating layer in TRISO fuel particles,” *J. Nucl. Mater.*, vol. 442, no. 1–3, pp. 133–142, Nov. 2013.
- [37] Y. Katoh, L. L. Snead, I. Szlufarska, and W. J. Weber, “Radiation effects in SiC for nuclear structural applications,” *Curr. Opin. Solid State Mater. Sci.*, vol. 16, no. 3, pp. 143–152, Jun. 2012.
- [38] D. P. Stinton, W. J. Lackey, and P. Angelini, “Immobilization of Radioactive Cesium in Pyrolytic-Carbon-Coated Zeolite,” *J. Am. Ceram. Soc.*, vol. 66, no. 6, pp. 389–392.
- [39] D. P. Stinton, P. Angeiini, A. J. Caputo, and W. J. Lackey, “Coating of Crystalline Nuclear Waste Forms to Improve Inertness,” 1982.
- [40] T. P. Strachan D, Henager CH, Bryan SA, Levitskaia TG, Matya J and Z. F. Scheele RD, Weber WJ, “Processes for removal and immobilization of ^{14}C , ^{129}Cs , and ^{85}Kr ,” Richland, 2009.
- [41] R. Kurihara, S. Ueda, S. Nishio, and Y. Seki, “Fracture mechanics evaluation of a crack generated in SiC/SiC composite first wall,” *Fusion Eng. Des.*, vol. 54, no. 3–4, pp. 465–471, Apr. 2001.

- [42] M. Shibui, J. Ohmori, Y. Sawada, A. Ozaki, T. Kuroda, O. Kaneko, and Y. Oka, “Thermal shock resistances of aln and sic for first wall applications,” *Fusion Eng. Des.*, vol. 9, pp. 33–38, Jan. 1989.
- [43] M. Nagatsu, N. Takada, and M. Shimada, “Effect of beryllium-coating on power reflectivity of SiC and and C/C first-wall materials,” *J. Nucl. Mater.*, vol. 226, no. 1–2, pp. 256–259, Oct. 1995.
- [44] P. Yvon and F. Carré, “Structural materials challenges for advanced reactor systems,” *J. Nucl. Mater.*, vol. 385, no. 2, pp. 217–222, Mar. 2009.
- [45] B. Riccardi, L. Giancarli, A. Hasegawa, Y. Katoh, A. Kohyama, R. . Jones, and L. . Snead, “Issues and advances in SiCf/SiC composites development for fusion reactors,” *J. Nucl. Mater.*, vol. 329–333, pp. 56–65, Aug. 2004.
- [46] A. I. Ryazanov, A. V. Klaptsov, A. Kohyama, Y. Katoh, and H. Kishimoto, “Effect of Helium on Radiation Swelling of SiC,” *Phys. Scr.*, vol. T111, no. 1, p. 195, 2004.
- [47] W. F. Knippenberg, “Philips Research Reports,” vol. 18, pp. 161–274, 1963.
- [48] S. E. Sadow and A. Agarwal, *Advances in Silicon Carbide Processing and Applications*. 2004.
- [49] C. Pawley, “The use of in-situ ion-irradiation / TEM techniques to study radiation damage in SiC,” University of Salford, 2013.
- [50] D. Fink and L. Chadderton, “Ion-solid interaction: status and perspectives,” *Brazilian J. Phys.*, vol. 35, no. 3, 2005.
- [51] M. T. Robinson, “The binary collision approximation: Background and introduction,” *Radiat. Eff. Defects Solids*, vol. null, no. 1, pp. 3–20, Jul. 1994.
- [52] M. Nastasi, J. W. Mayer, and J. K. Hirvonen, *Ion-solid interactions: Fundamentals and applications*. 1996.
- [53] G. S. Was, *Fundamentals of Radiation Materials Science*. 1921.

- [54] W. Möller, “Fundamentals of Ion-Solid Interaction I: Stopping and Ranges,” 2010.
- [55] M. T. Robinson and O. S. Oen, “The Channeling of Energetic Atoms in Crystal Lattices,” *Appl. Phys. Lett.*, vol. 2, no. 2, p. 30, 1963.
- [56] I. Chakarov and M. Temkin, “Modelling of ion implantation in SiC crystals,” *Nucl. Instruments Methods Phys. Res. Sect. B Beam Interact. with Mater. Atoms*, vol. 242, no. 1–2, pp. 690–692, Jan. 2006.
- [57] C. H. Park, B. Cheong, K. Lee, and K. J. Chang, “Structural and electronic properties of cubic, 2H, 4H, and 6H SiC,” *Phys. Rev. B*, vol. 49, no. 7, pp. 4485–4493, 1994.
- [58] W. Möller, *Fundamentals of Ion-Surface Interaction*. 2004.
- [59] J. A. Brinkman, “Production of atomic displacements by high-energy particles,” *Am. J. Phys.*, vol. 24, p. 246, 1956.
- [60] J. Ayache, L. Beaunier, J. Boumendil, G. Ehret, and Laub D., *Sample Preparation Handbook for Transmission Electron Microscopy*. 2010.
- [61] J. Sarkar, *Sputtering Materials for VLSI and Thin Film Devices*. 2013.
- [62] W. Eckstein, C. García-Rosales, J. Roth, and W. Ottenberger, “Sputtering Data,” 1993.
- [63] J. Roth, J. Bohdansky, W. Poschenrieder, and M. K. Sinha, “Physical and chemical sputtering of graphite and SiC by hydrogen and helium in the energy range of 600 to 7500 eV,” *J. Nucl. Mater.*, vol. 63, pp. 222–229, Dec. 1976.
- [64] L. Bischoff, J. Teichert, and V. Heera, “Focused ion beam sputtering investigations on SiC,” *Appl. Surf. Sci.*, vol. 184, no. 1–4, pp. 372–376, Dec. 2001.
- [65] T. S. Pugacheva, F. G. Jurabekova, Y. Miyagawa, and S. K. Valiev, “Computer simulation of SiC and B₄C sputtering by Ar⁺ and He⁺ ions bombardment,” *Nucl. Instruments Methods Phys. Res. Sect. B Beam Interact. with Mater. Atoms*, vol. 127–128, pp. 260–264, May 1997.

- [66] G. Ecke, R. Kosiba, V. Kharlamov, Y. Trushin, and J. Pezoldt, "The estimation of sputtering yields for SiC and Si," *Nucl. Instruments Methods Phys. Res. Sect. B Beam Interact. with Mater. Atoms*, vol. 196, no. 1–2, pp. 39–50, Nov. 2002.
- [67] W. Eckstein and J. P. Biersack, "Computer simulation of two-component target sputtering," *Appl. Phys. A*, vol. 37, no. 2, pp. 95–108, 1985.
- [68] M. L. Rousha, T. D. Andreadisa, and O. F. Goktepeb, "Evolve, a time-dependent monte carlo code to simulate the effects of ion-beam-induced atomic mixing," *Radiat. Eff.*, vol. 55, no. 1–2, pp. 119–129, 1981.
- [69] Y. Miyagawa, Y. Ato, and S. Miyagawa, "Computer Simulation of Range and Damage Distributions of He ions in SiC," *Jpn. J. Appl. Phys.*, vol. 23, no. 1–11, p. 1482, 1982.
- [70] Gras-Marti, V. Konoplev, and Alberto, "Ion-induced collisional relocation of multicomponent targets," *Phys. Rev. B*, vol. 46, no. 21, pp. 13713–13721, 1992.
- [71] T. S. Pugacheva, "Transition layer formation simulation during film deposition by an ion-molecular beam," *Radiat. Eff.*, vol. 102, no. 1–4, pp. 143–155, Feb. 1987.
- [72] D. B. Williams and C. B. Carter, *Transmission Electron Microscopy*. 1996.
- [73] B. J. Kestel, *Polishing Methods for Metallic and Ceramic Transmission Electron Microscopy Specimens*. 1981.
- [74] J. P. Hytch, M.J., Chevalier, "The effect of amorphous surface layers on HREM images of crystalline material," in *Proc. of ICEM 13*, 1994, pp. 367–368.
- [75] P. Buffat, P.A., Ganiere, J.D., Stadelmann, *Evaluation of Advanced Semiconductor Materials by Electron Microscopy*. NATO ASI Series B, 1988.
- [76] F. Benaissa, M., Humbert P., Ehret, G., Bensmina, "Cleaved Si substrate wedges for thin film sandwich TEM observations," in *Proc. of ICEM 13*, 1994, pp. 1029–1030.
- [77] I.-T. Bae, M. Ishimaru, and Y. Hirotsu, "Structural changes of SiC under electron-beam irradiation: Temperature dependence," *Nucl. Instruments Methods Phys. Res. Sect. B Beam Interact. with Mater. Atoms*, vol. 250, no. 1–2, pp. 315–319, Sep. 2006.

- [78] K. Anantheshwara and M. S. Bobji, "In situ transmission electron microscope study of single asperity sliding contacts," *Tribol. Int.*, vol. 43, no. 5–6, pp. 1099–1103, May 2010.
- [79] J. Reyes-Gasga and R. García-García, "Analysis of the electron-beam radiation damage of TEM samples in the acceleration energy range from 0.1 to 2MeV using the standard theory for fast electrons," *Radiat. Phys. Chem.*, vol. 64, no. 5–6, pp. 359–367, Aug. 2002.
- [80] J. A. Hinks, "A review of transmission electron microscopes with in situ ion irradiation," *Nucl. Instruments Methods Phys. Res. Sect. B Beam Interact. with Mater. Atoms*, vol. 267, no. 23–24, pp. 3652–3662, Dec. 2009.
- [81] J. Chen, P. Jung, and H. Trinkaus, "Evolution of Helium Platelets and Associated Dislocation Loops in a-SiC," *Phys. Rev. Lett.*, vol. 82, pp. 2709–2712, 1999.
- [82] K. Hojou and K. Izui, "Bubbles in SiC crystal formed by helium ion irradiation at high temperature," *J. Nucl. Mater.*, vol. 160, pp. 147–152, 1988.
- [83] K. Hojou., S. Furuno., H. Otsu., K. Izui., and T. Tsukamoto., "In-situ observation system of the dynamic process of structural changes during ion irradiation and its application to SiC and TiC crystals," *J. Nucl. Mater.*, vol. 155–157, pp. 298–302, 1988.
- [84] E. Oliviero, C. Tromas, F. Pailloux, A. Decléry, M. F. Beaufort, C. Blanchard, and J. F. Barbot, "Damage formation and recovery in temperature helium implanted 4H-SiC," *Mater. Sci. Eng. B*, vol. 102, no. 1–3, pp. 289–292, Sep. 2003.
- [85] S. Adachi, S. Fukuda, M. Mohri, and T. Yamashina, "Surface compositional changes of TiC, B₄C and SiC at high temperatures," *J. Nucl. Mater.*, vol. 133–134, pp. 263–267, Aug. 1985.
- [86] P. Miranda, U. Wahl, N. Catarino, K. Lorenz, J. G. Correia, and E. Alves, "Damage formation and recovery in Fe implanted 6H-SiC," *Nucl. Instruments Methods Phys. Res. Sect. B Beam Interact. with Mater. Atoms*, vol. 286, pp. 89–92, Sep. 2012.

- [87] H. J. von Bardeleben and J. L. Cantin, "Electron irradiation induced defects in monocrystalline 4H-SiC and 6H-SiC: the influence of the electron energy and doping," *Appl. Surf. Sci.*, vol. 184, no. 1–4, pp. 237–241, Dec. 2001.
- [88] A. L. Barry, B. Lehmann, D. Fritsch, and D. Braunig, "Energy dependence of electron damage and displacement threshold energy in 6H silicon carbide," *Nucl. Sci. IEEE Trans.*, vol. 38, no. 6, pp. 1111–1115, 1991.
- [89] J. L. Cantin, L. Henry, and M. F. Barthe, "Vacancy defects in p-type 6H-SiC created by low-energy electron irradiation," *Phys. Rev. B*, vol. 62, no. 16, pp. 841–846, 2000.
- [90] K. Danno and T. Kimoto, "Investigation of deep levels in n-type 4H-SiC epilayers irradiated with low-energy electrons," *J. Appl. Phys.*, vol. 100, no. 11, p. 113728, 2006.
- [91] F. Gao, W. J. Weber, M. Posselt, and V. Belko, "Atomic Computer Simulations of Defect Migration in 3C and 4H-SiC," *Mater. Sci. Forum*, vol. 457–460, pp. 457–460, 2004.
- [92] W. J. Choyke, H. Matsunami, and Gerhard Pensl, *Silicon Carbide, Recent Major Advances*. 2001.
- [93] K. Danno and T. Kimoto, "Deep level transient spectroscopy on as-grown and electron-irradiated p-type 4H-SiC epilayers," *J. Appl. Phys.*, vol. 101, no. 10, p. 103704, 2007.
- [94] J. . Steeds, G. . Evans, L. . Danks, S. Furkert, W. Voegeli, M. . Ismail, and F. Carosella, "Transmission electron microscope radiation damage of 4H and 6H SiC studied by photoluminescence spectroscopy," *Diam. Relat. Mater.*, vol. 11, no. 12, pp. 1923–1945, Dec. 2002.
- [95] M. Ishimaru, I.-T. Bae, and Y. Hirotsu, "Electron-beam-induced amorphization in SiC," *Phys. Rev. B*, vol. 68, no. 14, p. 144102, Oct. 2003.
- [96] I.-T. Bae, W. J. Weber, M. Ishimaru, and Y. Hirotsu, "Effect of ionization rates on dynamic recovery processes during electron-beam irradiation of 6H-SiC," *Appl. Phys. Lett.*, vol. 90, no. 12, p. 121910, 2007.

- [97] H. Itoh, N. Hayakawa, I. Nashiyama, and E. Sakuma, "Electron spin resonance in electron-irradiated 3C-SiC," *J. Appl. Phys.*, vol. 66, no. 9, p. 4529, 1989.
- [98] S. Arpiainen, K. Saarinen, P. Hautojärvi, L. Henry, M.-F. Barthe, and C. Corbel, "Optical transitions of the silicon vacancy in 6H-SiC studied by positron annihilation spectroscopy," *Phys. Rev. B*, vol. 66, pp. 1–10, 2002.
- [99] H. Itoh, M. Yoshikawa, I. Nashiyama, H. Okumura, S. Misawa, and S. Yoshida, "Photoluminescence of radiation induced defects in 3C-SiC epitaxially grown on Si," *J. Appl. Phys.*, vol. 77, no. 2, p. 837, 1995.
- [100] X. Chen, C. Yang, M. Gong, W. Ge, S. Fung, C. Beling, J. Wang, M. Lui, and C. Ling, "Low Energy Electron Irradiation Induced Deep Level Defects in 6H-SiC: The Implication for the Microstructure of the Deep Levels E1/E2," *Phys. Rev. Lett.*, vol. 92, pp. 10–13, 2004.
- [101] N. Asaoka, "Formation of Si clusters in electron-irradiated SiC studied by electron energy-loss spectroscopy," *Diam. Relat. Mater.*, vol. 10, pp. 1251–1254, 2001.
- [102] H. Inui, H. Mow, and H. Fujita, "Electron irradiation induced crystalline amorphous transition in ceramics," *Acta Metall.*, vol. 37, pp. 1337–1342, 1989.
- [103] H. Ohyama, K. Takakura, K. Uemura, K. Shigaki, T. Kudou, M. Arai, S. Kuboyama, S. Matsuda, C. Kamezawa, E. Simoen, and C. Claeys, "Radiation-induced defects in SiC-MESFETs after 2-MeV electron irradiation," *Phys. B Condens. Matter*, vol. 376–377, pp. 382–384, 2006.
- [104] T. Sugiyama, Y. Morimoto, K. Iguchi, K. Okuno, M. Miyamoto, H. Iwakiri, and N. Yoshida, "Effects of helium irradiation on chemical behavior of energetic deuterium in SiC," *J. Nucl. Mater.*, vol. 307–311, pp. 1080–1083, 2002.
- [105] H. K., F. S., O. H., I. K., and T. T., "In-situ observation system of the dynamic process of structural changes during ion irradiation and its application to SiC and TiC crystals," *J. Nucl. Mater.*, vol. 155–157, pp. 298–302, Jul. 1988.

- [106] J. F. Barbot, S. Leclerc, M.-L. David, E. Oliviero, R. Montsouka, F. Pailloux, D. Eyidi, M.-F. Denanot, M.-F. Beaufort, A. Declémy, V. Audurier, and C. Tromas, “Helium implantation into 4H-SiC,” *Phys. Status Solidi*, vol. 206, no. 8, pp. 1916–1923, Aug. 2009.
- [107] B. S. Li, C. H. Zhang, H. H. Zhang, T. Shibayama, and Y. T. Yang, “Study of the damage produced in 6H-SiC by He irradiation,” *Vacuum*, vol. 86, no. 4, pp. 452–456, Nov. 2011.
- [108] C. H. Zhang, S. E. Donnelly, V. M. Vishnyakov, J. H. Evans, T. Shibayama, and Y. M. Sun, “A study of the formation of nanometer-scale cavities in helium-implanted 4H-SiC,” *Nucl. Instruments Methods Phys. Res. Sect. B Beam Interact. with Mater. Atoms*, vol. 218, pp. 53–60, Jun. 2004.
- [109] P. Jung, H. Klein, and J. Chen, “A comparison of defects in helium implanted α - and β -SiC,” *J. Nucl. Mater.*, vol. 283–287, pp. 806–810, Dec. 2000.
- [110] J. Chen, P. Jung, and H. Trinkaus, “Microstructural evolution of helium-implanted α -SiC,” *Phys. Rev. B*, vol. 61, no. 19, pp. 923–932, 2000.
- [111] W. Skorupa, V. Heera, Y. Pacaud, and H. Weishart, “Ion beam processing of single crystalline silicon carbide,” *Nucl. Instruments Methods Phys. Res. Sect. B Beam Interact. with Mater. Atoms*, vol. 120, pp. 114–120, 1996.
- [112] I. A. Salama, N. R. Quick, and A. Kar, “Laser doping of silicon carbide substrates,” *J. Electron. Mater.*, vol. 31, pp. 200–208, 2002.
- [113] J. D. Hong and R. F. Davis, “Self-Diffusion of Carbon-14 in High-Purity and N-Doped α -SiC Single Crystals,” *J. Am. Ceram. Soc.*, vol. 63, no. 9, pp. 546–552, 1980.
- [114] J. D. Hong, R. F. Davis, and D. E. Newbury, “Self-diffusion of silicon-30 in α -SiC single crystals,” *J. Mater. Sci.*, vol. 16, pp. 2485–2494, 1981.
- [115] K. Rüschemschmidt, H. Bracht, N. a. Stolwijk, M. Laube, G. Pensl, and G. R. Brandes, “Self-diffusion in isotopically enriched silicon carbide and its correlation with dopant diffusion,” *J. Appl. Phys.*, vol. 96, no. 3, p. 1458, 2004.

- [116] Y. Sun, T. Miyasato, and N. Sonoda, "Outdiffusion of the excess carbon in SiC films into Si substrate during film growth," *J. Appl. Phys.*, vol. 84, no. 11, p. 6451, 1998.
- [117] P. Jung, "Diffusion and retention of helium in graphite and silicon carbide," *J. Nucl. Mater.*, vol. 191–194, pp. 377–381, Sep. 1992.
- [118] Y. Pramono, K. Sasaki, and T. Yano, "Release and Diffusion Rate of Helium in Neutron-Irradiated SiC," *J. Nucl. Sci. Technol.*, vol. 41, no. 7, pp. 751–755, Jul. 2004.
- [119] H. Huang, N. M. Ghoniem, J. K. Wong, and M. I. Baskes, "Molecular dynamics determination of defect energetics in B-SiC using three representative empirical potentials," *Model. Simul. Mater. Sci. Eng.*, vol. 3, pp. 615–217, 1995.
- [120] J. Benedicta, R. Andersona, and S. J. Klepeisa, "Recent Developments in the use of the Tripod Polisher for TEM Specimen Preparation," in *MRS Fall Meeting*, 1991.
- [121] L. A. Giannuzzi and F. A. Stevie, "A review of focused ion beam milling techniques for TEM specimen preparation," *Micron*, vol. 30, no. 3, pp. 197–204, Jun. 1999.
- [122] J. A. Hinks, A. N. Jones, A. Theodosiou, J. A. van den Berg, and S. E. Donnelly, "Transmission Electron Microscopy Study of Graphite under in situ Ion Irradiation," *J. Phys. Conf. Ser.*, vol. 371, p. 012046, Jul. 2012.
- [123] Colutron Research Corporation, "Instructions of ion source assembly," 1997.
- [124] H.L.Heinisch, "Transmutations in SiC irradiated in ARIES-IV first wall," 2001.
- [125] J. F. Ziegler, M. D. Ziegler, and J. P. Biersack, "SRIM – The stopping and range of ions in matter (2010)," *Nucl. Instruments Methods Phys. Res. Sect. B Beam Interact. with Mater. Atoms*, vol. 268, no. 11–12, pp. 1818–1823, Jun. 2010.
- [126] P. Stadelmann, "JEMs:Electron Microscopy Software Java Version 3," *CIME-EPFL,Switzerland*. .
- [127] P. F. P. Fichtner, J. R. Kaschny, R. A. Yankov, A. Mücklich, U. Kreißig, and W. Skorupa, "Overpressurized bubbles versus voids formed in helium implanted and annealed silicon," *Appl. Phys. Lett.*, vol. 70, no. 6, p. 732, 1997.

- [128] A. Jostsons, C. K. H. DuBose, G. . Copeland, and J. O. Stiegler, “Defect structure of neutron irradiated boron carbide,” *J. Nucl. Mater.*, vol. 49, no. 2, pp. 136–150, Dec. 1973.
- [129] Trinkaus, “³He bubble formation in titanium tritides at elevated temperatures A TEM study,” *Philos. Mag. A*, vol. 65, no. 5, pp. 1235–1247, 1992.
- [130] J. H. Evans, A. Van Veen, and L. M. Caspers, “Formation of helium platelets in molybdenum,” *Nature*, vol. 291, p. 310, 1981.
- [131] J. H. Evans, A. Van Veen, and L. M. Caspers, “The application of TEM to the study of helium cluster nucleation and growth in molybdenum at 300 K,” *Radiat. Eff.*, vol. 78, no. 1–4, pp. 105–120, Jan. 1983.
- [132] T. Sawabe, M. Akiyoshi, K. Ichikawa, K. Yoshida, and T. Yano, “Microstructure of heavily neutron-irradiated SiC after annealing up to 1500 °C,” *J. Nucl. Mater.*, vol. 386–388, no. C, pp. 333–337, 2009.
- [133] M. Bockstedte, A. Mattausch, and O. Pankratov, “Ab initio study of the annealing of vacancies and interstitials in cubic SiC: Vacancy-interstitial recombination and aggregation of carbon interstitials,” *Phys. Rev. B - Condens. Matter Mater. Phys.*, vol. 69, no. 23, pp. 1–13, 2004.
- [134] J. H. Evans, A. Van Veen, and L. M. Caspersb, “Precipitation in low energy helium irradiated molybdenum,” *Radiat. Eff.*, vol. 78, no. 1–4, pp. 105–120, 1983.
- [135] M. W. Finnis, A. Van Veen, and L. M. Caspers, “The energy of helium filled platelets and bubbles in molybdenum,” *Radiat. Eff.*, vol. 78, no. 1–4, pp. 121–132, Jan. 1983.
- [136] H. Yamaguchi, I. Hashimoto, H. Mitsuya, K. Nakamura, E. Yagi, and M. Iwaki, “The random motion of bubbles in krypton-implanted aluminum,” *J. Nucl. Mater.*, vol. 161, pp. 164–168, 1989.
- [137] J. Evans and A. van Veen, “An electron microscope study of helium bubble diffusion in gold,” *J. Nucl. Mater.*, vol. 168, pp. 12–18, 1989.

- [138] J. Evans, "Bubble diffusion to grain boundaries in UO₂ and metals during annealing: a new approach," *J. Nucl. Mater.*, vol. 210, pp. 21–29, 1994.
- [139] D. E. Alexander and R. Birtcher, "The effect of ion irradiation on inert gas bubble mobility," *J. Nucl. Mater.*, vol. 191–194, pp. 1289–1294, 1992.
- [140] H. Search, C. Journals, A. Contact, and M. Iopscience, "Theory of regular arrays of defects: The void lattice," *J. Phys. F. Met. Phys.*, vol. 1, no. 1, p. 778, 1971.